Influence of electrode commutation on magnetohydrodynamic flow in a supersonic diffuser

Yu. P. Golovachev and S. Yu. Sushchikh

A. F. Ioffe Physicotechnical Institute, Russian Academy of Sciences, St. Petersburg
(Submitted December 23, 1998)
Pis'ma Zh. Tekh. Fiz. **25**, 1–8 (May 12, 1999)

The slowing of an ionized gas in a supersonic diffuser operating as a magnetohydrodynamic (MHD) generator is investigated by numerical simulation. The calculation results, which reveal a significant dependence of the static pressure level and the Mach number distribution in the exit cross section of the diffuser on the design of the electrode system, are presented. © *1999 American Institute of Physics.* [S1063-7850(99)00105-6]

1. Let us consider a stationary gas flow in a flat channel that simulates the shape of the front part of the air intake of a supersonic aircraft. The operating efficiency of an air intake is known to be determined by the pressure restoration level. One of the promising methods for raising that level and controlling the flow is to preliminarily ionize the gas and employ an external magnetic field. The air intake then operates as a magnetohydrodynamic (MHD) generator.[1,2] This paper examines the dependence of the parameters of the ionized gas in a supersonic air intake on the variant of electrode commutation. The case of a Faraday generator with continuous and sectioned electrodes and the case of a Hall generator are considered.

2. The system considered has the form of a flat channel, whose form is shown in Fig. 1. The upper and lower walls of the channel serve as electrodes. The external magnetic field induction vector $\mathbf{B}(0,0,B_z)$ is perpendicular to the plane of the figure. The stationary flow of a preliminarily ionized gas in the channel is treated under the following basic assumptions:

a) the Reynolds number of the flow $Re=\rho_0 U_0 L/\mu_0 \gg 1$;

b) the extent of ionization of the gas $\alpha \ll 1$;

c) the Reynolds magnetic field $Re_m=U_0 L\sigma\mu \ll 1$;

d) the projection of the gas velocity onto the x axis is greater than the local velocity of sound, $M>1$, at all points in the calculation region.

Here ρ_0, U_0, and μ_0 are the characteristic values of the density, velocity, and viscosity of the gas; L is the linear scale of the flow, σ is the electrical conductivity, μ is the permeability of free space, and M is the Mach number.

Under the assumptions indicated, which correspond to the conditions of flow in the air intakes of supersonic aircraft, we can use the model of an ideal gas described by a system of Euler equations, neglect the influence of ionization on the thermodynamic properties of the gas, and assume that the magnetic induction vector has an assigned magnitude equal to the external magnetic field induction. The influence of an external magnetic field on the flow of an electrically conductive gas is mediated by the ponderomotive force $\mathbf{F}=\mathbf{j}\times\mathbf{B}$ and theJoule heat $Q=\mathbf{j}\cdot\mathbf{E}$. Here $\mathbf{j}$ is the electrical conduction current density, and $\mathbf{E}$ is the intensity of the induced electric field. When the external magnetic field induction $\mathbf{B}$ is known, these quantities are related by a generalized Ohm's law, which, without consideration of the slippage of ions and the electron pressure gradient, can be written in the form

$$\mathbf{j}+\mu_e(\mathbf{j}\times\mathbf{B})=\sigma(\mathbf{E}+\mathbf{V}\times\mathbf{B}), \tag{1}$$

where μ_e is the electron mobility. In the MHD generator regime the closing relation needed to calculate the ponderomotive force and the Joule heat is defined in terms of the external load factor.[3]

When external magnetic field has the orientation indicated, the z component of the ponderomotive force is equal to zero. The formulas for other projections of that force and the Joule heat depend on the variant of electrode commutation.[4]

a) Faraday generator with continuous electrodes. In this case the projection of the electric field intensity vector onto line l, whose direction varies linearly from the direction of the lower electrode to the direction of the upper electrode, is set equal to zero. Then $E_x=-E_y\tan\varphi$, where φ is the angle of inclination of line l to the x axis. Introducing the external load factor $k=E_y/u_xB$, we can obtain the following formulas for the projections of the ponderomotive force vector and the Joule heat:

$$F_x=\frac{\sigma B^2}{1+\beta_e^2}[\beta_e(u_y-ku_x\tan\varphi)-u_x(1-k)],$$

$$F_y=-\frac{\sigma B^2}{1+\beta_e^2}[u_y-ku_x\tan\varphi+u_x\beta_e(1-k)], \tag{2}$$

$$Q=\frac{\sigma B^2}{1+\beta_e^2}ku_x\{\beta_e(u_y-ku_x\tan\varphi)-u_x(1-k) -[(1-k)\beta_e u_x+u_y-ku_x\tan\varphi]\tan\varphi\},$$

where $\beta_e=\mu_e|B|$ is the Hall parameter.

b) Faraday generator with ideally sectioned electrodes. In this case the projection of the current density vector onto

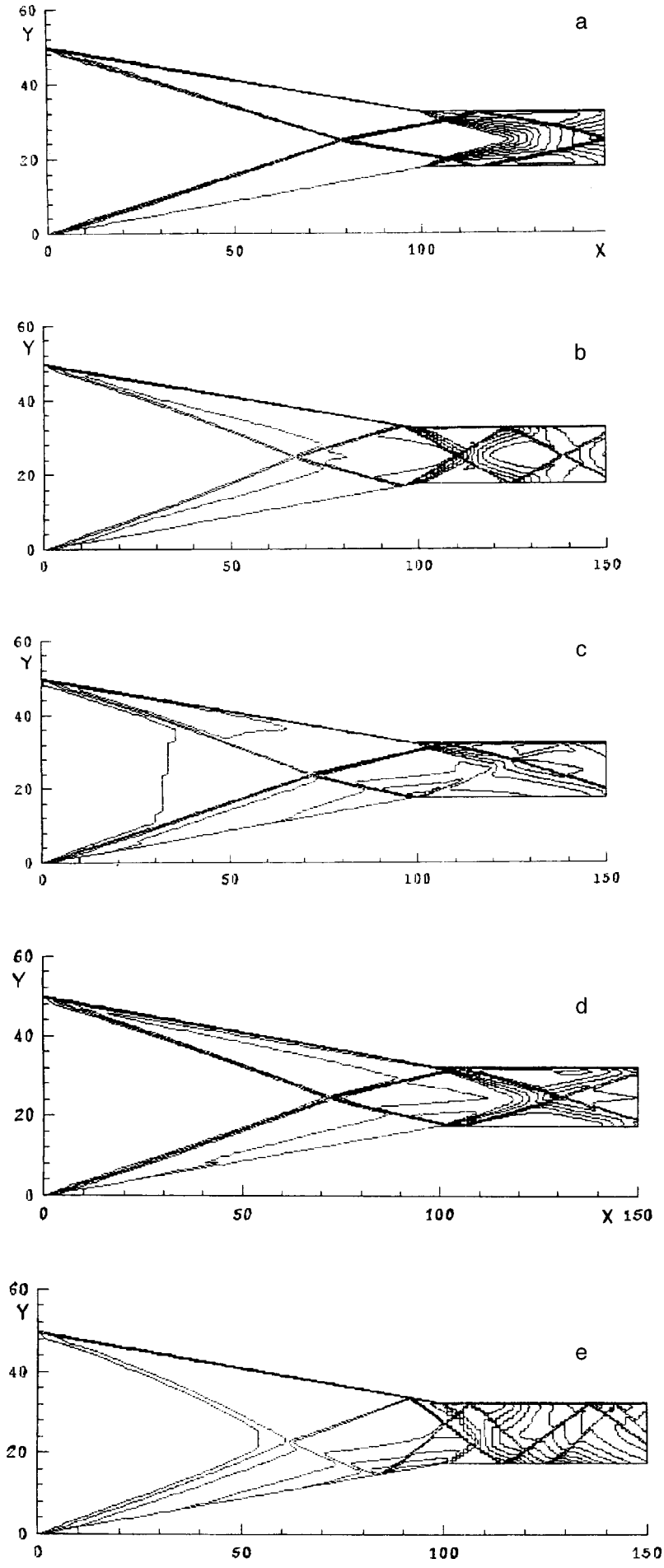

FIG. 1. Density isolines. a — $B=0.0$; b —Faraday generator with continuous electrodes, $\beta_e=0.0$; c —Faraday generator with continuous electrodes, $\beta_e=1.0$; d — Faraday generator with sectioned electrodes, $\beta_e=1.0$; e — Hall generator, $\beta_e=1.0$.

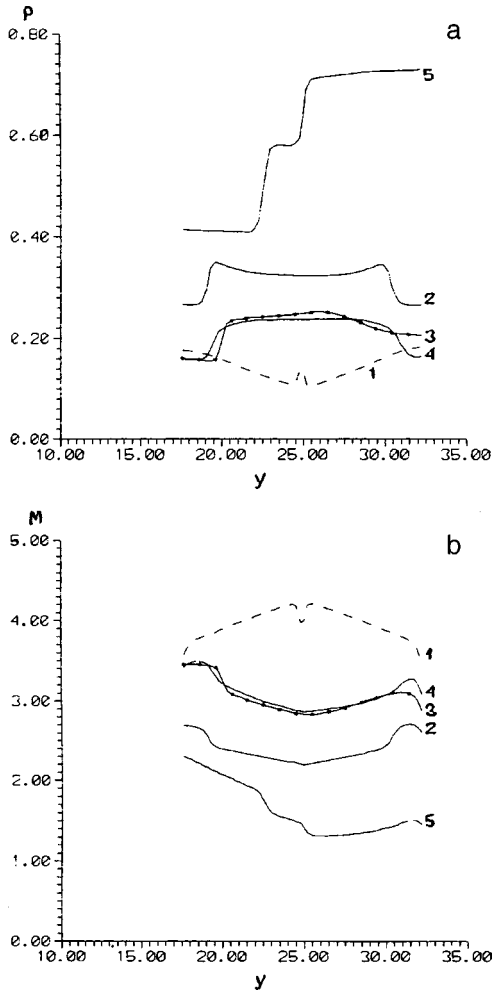

FIG. 2. Distribution profiles of the pressure (a) and the Mach number (b) in the exit cross section of the diffuser. *1* — $B=0.0$; *2* — Faraday generator with continuous electrodes, $\beta_e=0.0$; *3* — Faraday generator with continuous electrodes, $\beta_e=1.0$; *4* — Faraday generator with sectioned electrodes, $\beta_e=1.0$; *5* — Hall generator, $\beta_e=1.0$.

line l, which was defined above, is equal to zero. Then $j_x=-j_y\tan\varphi$, and under the former definition of the load factor we have

$$F_x=-\frac{\sigma B^2}{1+\beta_e\tan\varphi}u_x(1-k),\quad F_y=F_x\tan\varphi, \tag{3}$$

$$Q=-\frac{\sigma B^2}{1+\beta_e\tan\varphi}(1-k)u_x\left[\frac{1+\tan^2\varphi}{1+\beta_e\tan\varphi}ku_x+\left(\frac{\beta_e-\tan\varphi}{1+\beta_e\tan\varphi}u_x+u_y\right)\tan\varphi\right].$$

c) Hall generator. In this case the projection of the electric field intensity vector onto a normal to line l is equal to zero, giving $E_y=E_x\tan\varphi$. The external load factor is defined by the formula $k=E_x/u_yB$. The projections of the ponderomotive force vector and the Joule heat are defined by the formulas

$$F_x=\frac{\sigma B^2}{1+\beta_e^2}[(\beta_e+\tan\varphi)ku_y+\beta_eu_y-u_x)],$$

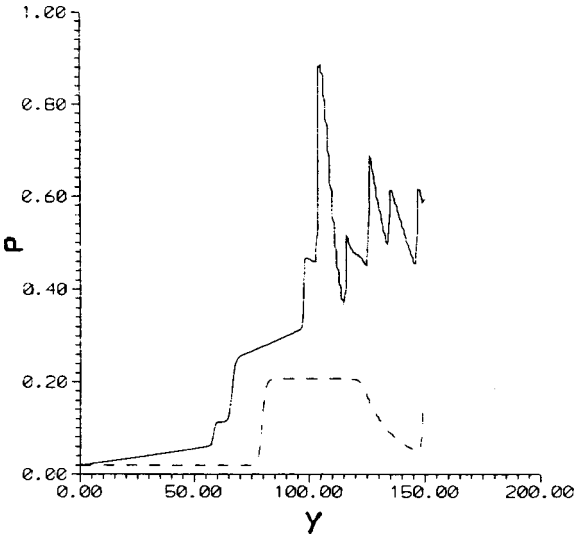

FIG. 3. Variation of the pressure in the symmetry plane of the diffuser: dashed line — $B=0.0$; solid line — Hall generator, $\beta_e=1.0$.

$$F_y=-\frac{\sigma B^2}{1+\beta_e^2}[(1-\beta_e\tan\varphi)ku_y+u_y+u_x\beta_e], \tag{4}$$

$$Q=\frac{\sigma B^2}{1+\beta_e^2}ku_y\{(1+k)u_y+\beta_eu_x+[(k\tan\varphi+\beta_e)u_y-u_x]\tan\varphi\}.$$

Formulas (2), (3), or (4), together with the thermodynamic relations, close the system of equations used to describe the flow under consideration. Under the assumption of a supersonic flow velocity this system is x-hyperbolic. It can be solved with the initial conditions at the entrance to the calculation region ($x=0$), where the values of all the gasdynamic functions are assigned, and by the boundary conditions for the absence of flow onto the diffuser walls.

Numerical solutions were obtained using an explicit Marsh through-calculation scheme of second-order accuracy.[5] The integration step along the Marsh x coordinate is determined from the stability condition. The difference grid contained 60 evenly spaced points in the transverse direction in most cases.

3. Calculations were performed for the simple physical model of a homogeneous ideal gas with a ratio between the specific heats $\gamma=1.4$. The MHD interaction is characterized by two dimensionless parameters: the Stuart number $S=\sigma B^2L/\rho_0U_0$ and the Hall parameter β_e.

Figures 1 and 2 present some calculation results, which correspond to a Mach number at the entrance to the diffuser $M_0=6$, a Stuart number $S=0.003$, and an external load factor $k=0.5$. Figure 1 shows density isolines in a diffuser in the absence of an external magnetic field (*a*), in the case of a Faraday generator with continuous (*b*, *c*), and ideally sectioned (*d*) electrodes, and a Hall generator (*e*). The density was calculated relative to the density for freestream flow, and the isolines were constructed with a spacing $\Delta\rho=0.3$. The figures reveal the significant influence of the MHD interaction on the shock-wave structure and violation of the flow

symmetry in the presence of the Hall effect. The quality of a supersonic air intake is characterized by the pressure restoration level in its exit cross section. Figure 2 shows profiles of the static pressure and the Mach number in that cross section for different variants of electrode commutation and two values of the Hall parameter. The pressure was calculated relative to $\rho_0 U_0^2$. We can, first, discern a significant rise in pressure and a drop in the Mach number due to the MHD interaction. The strongest effect is achieved for electrode commutation according to the scheme for a Hall generator. However, in that case the distribution profiles of the pressure and the Mach number in the exit cross section of the diffuser are most inhomogeneous. It should also be noted that the pressure level varies significantly along the diffuser. This is illustrated by Fig. 3, which presents the distribution of the static pressure along the diffuser axis.

This work was carried out with support from the Russian Fund for Fundamental Research (Grant No. 98-01-01121).

[1] C. Bruno, P. A. Czysz, and S. N. B. Murthy, AIAA Paper 97–3389 (1997).
[2] Yu. P. Golovachev, S. A. Il'in, and S. Yu. Sushchikh, Pis'ma Zh. Tekh. Fiz. **23**(16), 1 (1997) [Tech. Phys. Lett. **23**(8), 615 (1997)].
[3] M. Mitchner and C. H. Kruger, Jr., *Partially Ionized Gases*, Wiley, New York (1973) [Russ. transl., Mir, Moscow (1976)].
[4] V. V. Breev, A. V. Gubarev, and V. P. Panchenko, *Supersonic Magnetohydrodynamic Generators* [in Russian], Énergoatomizdat, Moscow (1988).
[5] A. V. Rodionov, Zh. Vychisl. Mat. Mat. Fiz. **27**, 1853 (1989).

Translated by P. Shelnitz

1/*f* noise in a model of intersecting phase transitions

V. N. Skokov and V. P. Koverda

Institute of Thermal Physics, Russian Academy of Sciences, Ural Branch, Ekaterinburg
(Submitted October 8, 1998)
Pis'ma Zh. Tekh. Fiz. **25**, 9–14 (May 12, 1999)

A mathematical model for the appearance of fluctuations with a spectrum inversely proportional to the frequency (flicker or $1/f$ noise) upon the intersection of phase transitions is proposed. A system with a two-valley potential, whose dynamics are described by two coupled nonlinear Langevin equations that transform Gaussian δ-correlated noise (white noise) into two modes of stochastic fluctuations with spectra having $1/f^{\mu}$ and $1/f^{\nu}$ frequency distributions, where $\mu \approx 1$ and $1.5 \leqslant \nu \leqslant 2$, is considered. © *1999 American Institute of Physics.* [S1063-7850(99)00205-0]

For many years there has been unwaning interest in random processes whose spectral density varies in inverse proportion to the frequency due to the widespread occurrence of this phenomenon and the absence of generally accepted, universal mathematical models. Stochastic processes with a spectrum that is inversely proportional to the frequency (flicker or $1/f$ noise) are observed in systems of very diverse nature, from current fluctuations in radiophysical devices to cellular automata, which simulate self-organized criticality. Numerous studies (see, for example, Refs. 1–4) have established the main properties of $1/f$ noise. However, the mechanism leading to the appearance of a $1/f$ spectrum and the location of its sources are often unclear. Most of the publications devoted to this phenomenon refer to spatially distributed systems. The model of an exponentially broad relaxation-time distribution,[1–3] in which $1/f$ noise is interpreted as the result of the superposition of random relaxation processes, has been used most often. A thermal model, in which heat conduction mechanisms are responsible for the $1/f$ behavior of the spectrum, is also widely known. However, the classical ''thermal-conductance'' model runs into some difficulties in accounting for experimental results.[1,2] In Ref. 5 $1/f$ noise was attributed to the presence of nonlinear heat sources in the system, and in Ref. 6 it was attributed to the interaction between diffusion and heat-conduction modes. In Ref. 4 flicker noise was treated as a result of Brownian motion in a bounded system.

In Refs. 7–10 we presented the results of the experimental discovery of thermal fluctuations with a $1/f$ spectrum accompanying the Joule heating of a superconductor in a boiling coolant. The distinguishing feature of these experiments is the presence of only one source of stochastic signals with a $1/f$ spectrum in the system, which can be considered zero-dimensional. Extended models of $1/f$ noise in spatially distributed systems cannot be used to explain the results. The origin of intense thermal fluctuations with a spectral density inversely proportional to the frequency can be associated with the interaction of nonequilibrium phase transitions occurring in the nonlinear subsystems, i.e., the current-carrying superconductor and the boiling coolant. A mathematical model of intersecting nonequilibrium phase transitions in the form of a system of two coupled Langevin equations that transforms white noise into two modes of fluctuations with spectral densities proportional to $1/f$ and $1/f^2$ was proposed in Refs. 9 and 10. The distinguishing feature of this model is the fact that the dynamic system is not a potential one. This paper proposes a potential system which yields results similar to those in Refs. 9 and 10.

Let us consider a point system in which two phase transitions with interacting order parameters X and Y take place. In the vicinity of the point of intersection of the lines of the phase transitions the potential of the system can be written in the form of the expansion[11]

$$\Phi = \Phi_0 - \alpha_1 X^2 - \alpha_2 Y^2 - \alpha_{12} XY + \beta_1 X^4 + \beta_2 Y^4 + \beta_{12} X^2 Y^2. \quad (1)$$

Taking into account that $\partial X/\partial t = -\partial\Phi/\partial X$ and $\partial Y/\partial t = -\partial\Phi/\partial Y$ and introducing fluctuating forces in the form of the additive terms $\Gamma_1(t)$ and $\Gamma_2(t)$,where $\Gamma_1(t)$ and $\Gamma_2(t)$ are Gaussian δ-correlatednoises, we can go over to a system of coupled Langevin equations:

$$dX/dt = -2\beta_{12} XY^2 - 4\beta_1 X^3 + 2\alpha_1 X + \alpha_{12} Y + \Gamma_1(t),$$
$$dY/dt = -2\beta_{12} YX^2 - 4\beta_2 Y^3 + 2\alpha_2 Y + \alpha_{12} X + \Gamma_2(t). \quad (2)$$

The system (2) was solved numerically by Euler's method with various parameters. The spectral density of the fluctuations was determined from the numerical solutions obtained for $X(t)$ and $Y(t)$ by fast Fourier transformation. In the simplest case, in which the solutions have diverging spectral characteristics, the parameters of the system are $\beta_{12} = 1/2$, $\beta_1 = \alpha_{12} = 1$, and $\alpha_1 = \alpha_2 = \beta_2 = 0$, and the system (2) takes on the form

$$dX/dt = -XY^2 - 4X^3 + Y + \Gamma_1(t),$$
$$dY/dt = -YX^2 + X + \Gamma_2(t). \quad (3)$$

In the absence of external noise the solution has the following asymptotes at $t \to \infty$: $X(t) \to t^{-1/2}$ and $Y(t) \to t^{1/2}$. The results of numerical calculations for an integration step dt

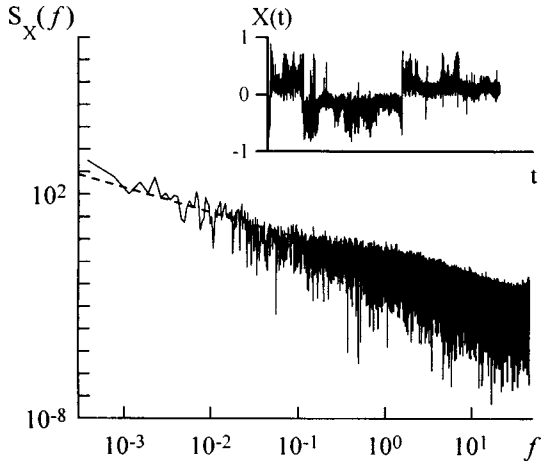

FIG. 1. Spectral density $S_X(f)$ of fluctuations of the order parameter X and a realization of $X(t)$. Dashed line — plot of $S_X(f) \propto 1/f^{1.05}$.

$=0.01$, a realization length $N=262143$ points, and the employment of a Gaussian sequence of random numbers with a zero mean and a standard deviation $\sigma=5$ as external noise (the results do not change fundamentally, if it is assumed that $\Gamma_1=\Gamma_2$) are presented in Fig. 1. It can be seen from Fig. 1 that the frequency dependence of the spectral density $S_X(f)$ of the fluctuations of $X(t)$ has the form $1/f^{\mu}$, where $\mu \approx 1$. In other words, the system (3) generates $1/f$ noise. The spectral density of the fluctuations of the order parameter $Y(t)$ depends on frequency according to an $S_Y(f) \propto 1/f^{\nu}$ law, where $1.5 \leqslant \nu \leqslant 2$. As the number of points is increased for an assigned integration step and dispersion of the external noise, the branches of the spectra become horizontal. Thus, for assigned dt and σ, divergent spectra are observed only in a bounded frequency range. However, this range can be extended in the low-frequency direction and the divergent low-frequency asymptote can be traced, if the integration step is decreased by a factor of n with a simultaneous increase in the standard deviation σ by a factor of $n^{1/2}$ as the number of intervals is increased by a factor of n. Thus, if we would have true ''white'' noise as a sequence of δ functions with an infinitesimal spacing, it is possible that $1/f$ behavior would also be observed when $f \to 0$.

The potential in whose field the system undergoes random walks described by the system (3) has the form

$$\Phi = \Phi_0 - XY + X^4 + \frac{1}{2}X^2Y^2. \tag{4}$$

The form of the potential surface (4) and the potential relief are shown in Fig. 2. The potential surface has two valleys, which are located in the first and third quadrants and separated by potential barriers. In the absence of external noise the phase trajectory is located entirely in one of the valleys, depending on the initial conditions. The motion is then infinite with respect to Y, and the process is nonstationary. When the amplitude of the external noise is small, the system undergoes random walks within a valley. As the noise intensity is increased, jumps from one valley to the other begin, and $1/f$ noise is observed in the system. The process becomes stationary, because the external noise does not let the system go too far along a valley. When the intensity of the external noise is excessively high, the system ceases to undergo Brownian motion along the valleys, the dynamics are specified completely by jumps between valleys, and the spectral densities have a typical Lorentzian form.

Thus, random walks in a two-valley potential lead to the appearance of fluctuations with a $1/f$ spectrum. The mechanism of the appearance of flicker noise is associated, as in the model with an exponentially broad distribution of relaxation times,[1–3] with overcoming different potential barriers. In the model proposed here a distribution of barriers is not postulated, but it is specified by the form of the potential (4), in whose field the random walks take place. It is then not necessary to assume that the system is spatially distributed.

The intersection and interaction of two phase transitions comprise a fairly widespread phenomenon. For this reason the proposed model can be fairly universal and can serve as a basis for explaining $1/f$ noise in a broad class of processes with phase transitions.

We thank V. P. Skritsov for discussing the results.

This work was carried out with support from the Russian Fund for Fundamental Research (Project Code 96-02-16077a).

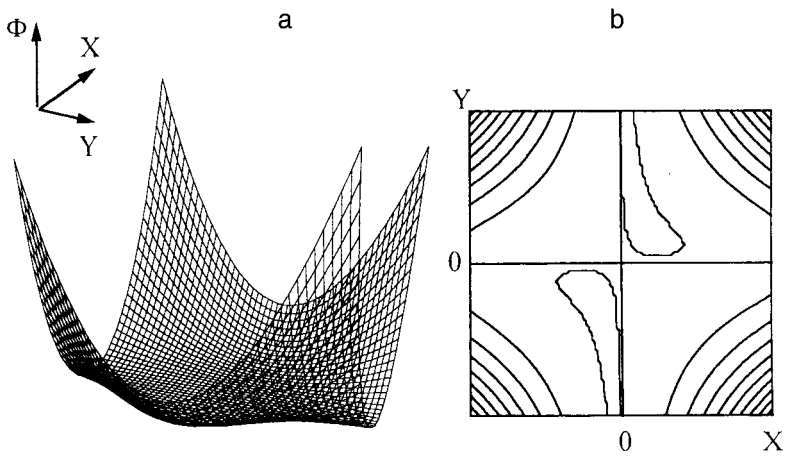

FIG. 2. Form of the potential surface $\Phi(X,Y)$ (a) and potential relief of $\Phi(X,Y)$ (b).

[1] Sh. M. Kogan, Usp. Fiz. Nauk **145**, 285 (1985) [Sov. Phys. Usp. **28**, 170 (1985)].
[2] M. B. Weissman, Rev. Mod. Phys. **60**, 537 (1988).
[3] G. P. Zhigal'skiĭ, Usp. Fiz. Nauk **167**, 624 (1997) [Phys. Usp. **40**, 599 (1997)].
[4] Yu. L. Klimontovich, *Statistical Theory of Open Systems, Vol. 1: A Unified Approach to Kinetic Description of Processes in Active Systems*, Kluwer Academic Publishers, Dordrecht–Boston (1995) [Russ. original, Yanus, Moscow (1995), 623 pp.].
[5] Yu. S. Levitan, N. N. Panchenko, and O. A. Sinkevich, Dokl. Akad Nauk SSSR **302**, 1359 (1988) [Sov. Phys. Dokl. **33**, 750 (1988)].
[6] R. O. Zaĭtsev, JETP Lett. **58**, 915 (1993).
[7] V. P. Koverda, V. N. Skokov, and V. P. Skripov, JETP Lett. **63**, 775 (1996).
[8] V. N. Skokov, V. P. Koverda, and V. P. Skripov, Cryogenics **37**, 263 (1997).
[9] V. P. Koverda, V. N. Skokov, and V. P. Skripov, Dokl. Akad Nauk **356**, 614 (1997) [Phys. Dokl. **42**, 532 (1997)].
[10] V. P. Koverda, V. N. Skokov, and V. P. Skripov, Zh. Éksp. Teor. Fiz. **113**, 1748 (1998) [JETP **86**, 953 (1998)].
[11] I. F. Lyuksyutov, V. L. Pokrovskiĭ, and D. E. Khmel'nitskiĭ, Zh. Éksp. Teor. Fiz. **69**, 1817 (1975) [Sov. Phys. JETP **42**, 923 (1975)].

Translated by P. Shelnitz

Near-threshold mode synchronization and *Q* switching in diode lasers with a fast saturated absorber

A. E. Gubenko, G. B. Venus, I. M. Gadzhiev, and E. L. Portnoĭ

A. F. Ioffe Physicotechnical Institute, Russian Academy of Sciences, St. Petersburg
(Submitted January 12, 1999)
Pis'ma Zh. Tekh. Fiz. **25**, 15–22 (May 12, 1999)

The near-threshold lasing regimes of AlGaAs lasers with an implanted saturated absorber under short pulsed pumping are investigated experimentally. A near-threshold mode-synchronization regime is obtained. © *1999 American Institute of Physics.*
[S1063-7850(99)00305-5]

1. INTRODUCTION

Both passive *Q*-switching and mode-synchronization regimes can be obtained in multisection diode lasers, in which one of the sections functions as a saturated absorber. A mode-synchronization regime is generally observed only at a considerable distance above the threshold,[1–3] where the self-pulsations associated with *Q* switching are suppressed. However, in the case of a fairly fast saturated absorber with a relaxation time τ_a comparable to the cavity transit period $\tau_{ct}=2Ln_g/c$ (L is the cavity length, n_g is the group refractive index, and c is the speed of light), the rate of the mode-synchronization process rises significantly with resultant alteration of the emission dynamics near the threshold.

As was shown in Refs. 5 and 6, a saturated absorber with a very short relaxation time $\sim 10^{-12}$ s can be created by ion implantation. This paper presents the results of an investigation of the near-threshold features of the output of diode lasers with an implanted saturated absorber under the conditions of short pulsed pumping and offers a qualitative explanation for mode synchronization near the threshold.

2. EXPERIMENTAL RESULTS

Stripe SiO_2/AlGaAs double heterostructure lasers with a thickness of the active region equal to 0.2 μm, a stripe width of 10 μm, and a cavity length of about 250 μm were used in the experiments. A saturated absorber region was created by implanting 16–18-MeV N^{4+} ions on both sides of the cavity mirror. The penetration depth of ions with such an energy in AlGaAs is 6–8 μm. The dose was varied in the range $5\times10^{10}-1.2\times10^{12}$ cm^{-2}. The lasers were pumped by current pulses with a duration of about 3 ns and a repetition rate of 1 MHz. Smooth regulation of the pump current permitted adjustment of the pulse amplitude so that the lasers would produce single pulses at a minimal distance above the threshold.

Typical spectra of lasers with a saturated absorber near the threshold are shown in Fig. 1. The transition from a superluminescence regime (a) to a lasing regime (b–d) was accompanied by a decrease in the duration of the emission pulse. The second-order autocorrelation function was measured to determine the dynamic parameters of the radiation. Figure 2 shows the autocorrelation curve characteristic of lasers irradiated by doses smaller than 5×10^{11} cm^{-2}. The presence of spikes on the curve indicates that the light pulse has a substructure, i.e., is not Fourier-confined. The duration of the spikes is determined by the emission spectrum, while the width of the entire curve corresponds to the duration of the light pulse. The rapid oscillations in the central spike are caused by interference, whose averaging leads to a contrast ratio equal to 2:1. This value corresponds to multimode lasing with random mode phases. The cross-correlation spikes separated from one another by the double cavity transit time have the same width and contrast ratio. This corresponds to repetition of the emission substructure after the cavity transit time. However, interference is generally not observed in the cross-correlation spikes because of the spontaneous emission of other sources of noise. The situation just described corresponds to a pure *Q*-switching regime.

When the dose of implanted ions is greater than 10^{12} cm^{-2}, the form of the autocorrelation function changes (Fig. 3). At the lasing threshold the contrast of the spikes equals 4.5:1. This means that longitudinal modes are synchronized already at the threshold in the nonstationary regime. We note that the emission time amounts to about 100 ps, which is significantly shorter than the characteristic times for the establishment of a mode-synchronization regime reported in Refs. 3 and 4. As the current is increased, the degree of synchronization decreases somewhat, as is manifested by a decrease in the contrast to 3:1. Nevertheless, a complete loss of synchronization does not occur at least until the onset of multipeak lasing.

We also observed an intermediate case of partial mode synchronization, which collapsed completely as the pump current was increased (Fig. 4). Here synchronization occurs only in a very narrow current range and vanishes when the energy of the light pulse is increased by about 10%, which corresponds to less than a 1% change in pump amplitude.

3. DISCUSSION OF RESULTS

We assume that the occurrence of mode synchronization near the threshold when the dose of implanted ions is sufficiently high and the dependence of the degree of synchronization on pump current can be qualitatively explained in the following manner.

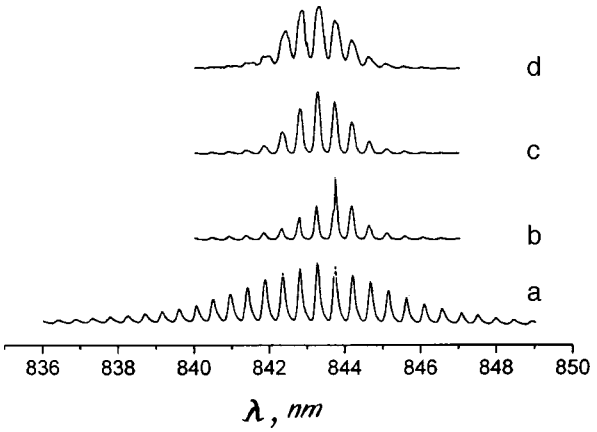

FIG. 1. Spectra of lasers with a saturated absorber near the threshold. The dose of implanted ions is 1.2×10^{12} cm^{-2}. Light-pulse energy: 1 pJ (a), 2 pJ (b), 3 pJ (c), and 6 pJ (d).

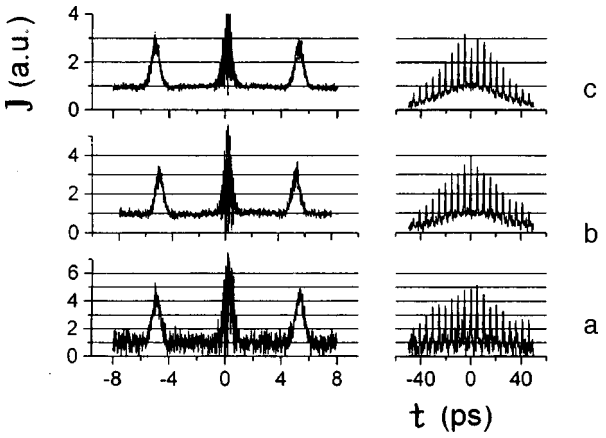

FIG. 3. Autocorrelation function of a laser in a mode-synchronization regime for various light-pulse energies: 5 pJ (a), 10 pJ (b), and 15 pJ (c). The dose of implanted ions is 1.2×10^{12} cm^{-2}.

The lasing regime depends on the recovery rate of the saturated absorber, which is determined by the lifetime of the nonequilibrium carriers τ_a. A saturated absorber obtained by heavy-ion implantation has separate lasing and carrier-recombination regions.[5] The recombination process takes place in the amorphized material along ion tracks. It can then be assumed in a first approximation that τ_a is determined by the transit time of electrons to the amorphized regions, i.e., an increase in the dose of implanted ions should lead to an increase in the speed of the absorber.

Let us consider two extreme cases of the possible behavior of a laser with a saturated absorber near the threshold under the conditions of a short pump pulse.

Let the dose be such that $\tau_a \gg \tau_{ct}$. During the passage of the current pulse the carrier concentration in the active region increases and surpasses the threshold value, at which the total gain and the total losses (including the losses in the unbleached absorber) are equal. The number of photons within the cavity begins to rise. When the intensity of the light in the cavity reaches E_a^s/τ_a (E_a^s is the saturation energy of the absorber), the absorber is bleached, and the losses decrease significantly as a result (Q switching occurs). The radiation intensity increases rapidly and grows until the population inversion in the active region is eliminated. In this case the absorber weakly senses the inhomogeneity of the intensity along the cavity, since it does not manage to recover. Therefore, the rate of the mode-synchronization process is not sufficient for establishing an appreciable correlation between the initial phases of the longitudinal modes during the period of emission. The beating of a large number of longitudinal modes with random phases produces random variation of the intensity during the time τ_{ct} with a nearly exponential distribution of the probability $P(I)$ (Ref. 7):

$$P(I)=\frac{1}{\langle I\rangle}\exp\left(-\frac{I}{\langle I\rangle}\right) \tag{1}$$

The contrast of the spikes on the mean autocorrelation function corresponding to this distribution is 2:1.

In the opposite case of a fairly high dose of implanted ions ($\tau_a \ll \tau_{ct}$), the radiated power needed to bleach the absorber E_a^s/τ_a increases significantly. However, the saturated absorber becomes sensitive to the inhomogeneity of the radiation during the time τ_{ct} and is bleached by local intensity maxima, which can significantly exceed the mean radiant flux density in the cavity. Redistribution of the intensity oc-

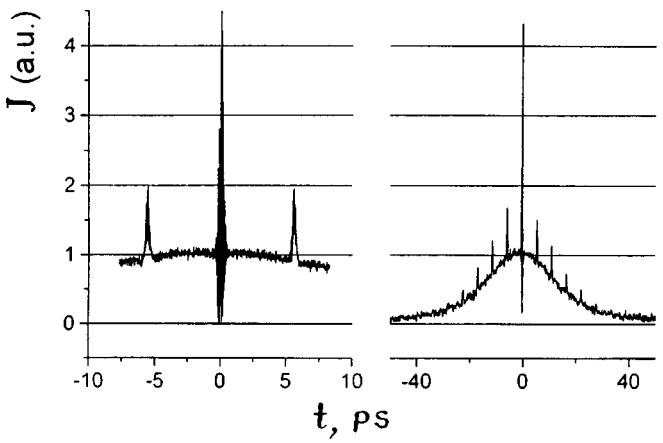

FIG. 2. Autocorrelation function for a laser with a saturated absorber in a passive Q-switching regime. The dose of implanted ions is 4×10^{11} cm^{-2}.

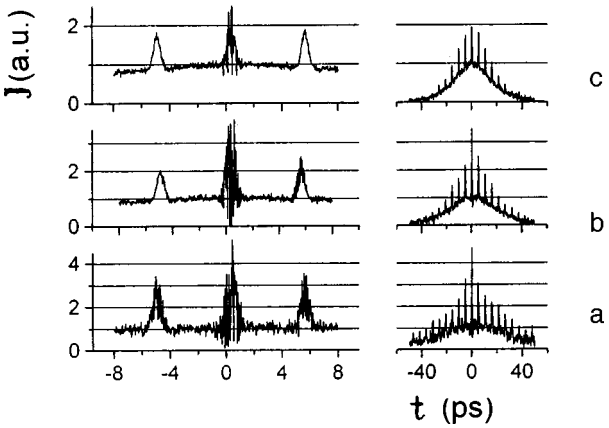

FIG. 4. Transition of a laser from partial mode synchronization to pulsed passive Q switching as the light-pulse energy is increased: 3.6 pJ (a), 3.9 pJ (b), and 4.5 pJ (c). The dose of implanted ions is 4×10^{11} cm^{-2}.

curs within the cavity as a result of the mode-synchronization process, which is considerably faster in the present case than under ordinary conditions, since the absorber supports the effective interaction of τ_{ct}/τ_a modes (and not just neighboring modes). In addition, passive mode synchronization is known to be a self-starting process and develops from the fluctuation which created the original inhomogeneity of the radiation in the cavity. The greater is the amplitude of the fluctuation, the faster is the initial rate of the synchronization process. In our case, if the number of modes N is not excessively large ($N \leqslant \tau_{ct}/\tau_a$), the saturated absorber ''senses'' inhomogeneities caused by intermodal beats, and, as can be seen from Ref. 1, these inhomogeneities are initially large: $\Delta I \sim \langle I \rangle$. The mode-synchronization process may also be ''accelerated'' by the deep modulation of the carrier concentration in the absorber $\Delta n_a \sim n_a$ when $\langle I \rangle \sim E_a^s/\tau_a$ (incontrast to the ordinary case, where $\langle I \rangle \gg E_a^s/\tau_a$ and the absorber is supersaturated). Thus, the saturated absorber is bleached by a short pulse produced by mode synchronization, and a sequence of pulses is emitted with a repetition period τ_{ct}. The autocorrelation function exhibits spikes of high contrast in this case.

Let us move on to the intermediate case ($\tau_a \sim \tau_{ct}$), which is a combination of the two extreme cases. In this case the emission process can be mentally divided into two stages. In the first stage ($\langle I \rangle \leqslant E_a^s/\tau_a$) mode synchronization takes place, and the saturated absorber is bleached. In the second stage ($\langle I \rangle \gg E_a^s/\tau_a$)the absorber is transparent, and rapid amplification of the radiation occurs until the population inversion in the active region is eliminated. The phase relations between the modes are established in the first stage, while the bulk of the energy is emitted in the second stage. As the pump current is increased, the residence time in the first stage shortens. If the time needed for synchronization is comparable to this period, the degree of synchronization should decrease with increasing pump current. Just such a dependence is observed experimentally in the intermediate case of partial mode synchronization.

4. CONCLUSION

Thus, mode synchronization, Q switching, and an intermediate lasing regime have been observed experimentally near the threshold under the conditions of a short pump pulse in AlGaAs lasers with a fast saturated absorber obtained by heavy-ion implantation. It has been established that the lasing regime depends on ion dose, which determines the speed of the saturated absorber, and on pump amplitude. The dependence on the latter is strongest in the intermediate case of partial mode synchronization, an increase in the pump current leading to a decrease in the degree of synchronization. A qualitative explanation has been proposed for the dependence of the lasing regime on the amplitude of the pump pulses and the dose of implanted ions.

This work was partially financed within contract No. IC15-CT96-0748 ''NIR-Diode Laser Systems for Infrared Spectroscopy.''

[1] E. L. Portnoi and A. V. Chelnokov, in *Digest of the 12th IEEE International Semiconductor Laser Conference*, Davos, Switzerland (1990), p. 140.
[2] E. L. Portnoi, E. A. Avrutin, and A. V. Chelnokov, *Joint Soviet–American Workshop on the Physics of Semiconductor Lasers*, Leningrad, USSR, May–June 1991, p. 58.
[3] W. Yang and A. Gopinath, Appl. Phys. Lett. **63**, 2717 (1993).
[4] O. Solgaard, M.-H. Kiang, and K. Y. Lau, Appl. Phys. Lett. **63**, 2021 (1993).
[5] E. A. Avrutin and M. E. Portnoĭ, Fiz. Tekh. Poluprovodn. **22**, 1524 (1988) [Sov. Phys. Semicond. **22**, 968 (1988)].
[6] A. B. Zhuravlev, V. A. Marushchak, E. L. Portnoĭ, N. M. Stel'makh, and A. N. Titkov, Fiz. Tekh. Poluprovodn. **22**, 352 (1988) [Sov. Phys. Semicond. **22**, 217 (1988)].
[7] *Ultrashort Light Pulses*, S. L. Shapiro (Ed.), Springer-Verlag, Berlin–New York (1977) [Russ. transl., Mir, Moscow (1981), pp. 119–123].

Translated by P. Shelnitz

Electric fields with annular features in corpuscular optics

Yu. K. Golikov, D. V. Grigor'ev, and T. A. Shorina

St. Petersburg State Technical University
(Submitted December 7, 1998)
Pis'ma Zh. Tekh. Fiz. **25**, 23–27 (May 12, 1999)

A new class of axisymmetric Laplace potentials with an annular feature that can be described by elementary functions is introduced. The possibilities of employing these potentials in the synthesis of energy-analyzing systems and lenses are discussed. Equipotential portraits of electric fields with annular features are presented. © *1999 American Institute of Physics.*
[S1063-7850(99)00405-X]

1. ORIGIN OF THE NEW CLASS OF POTENTIALS

We write an axisymmetric Laplace equation in the variables x and y, where x plays the role of the radial coordinate and y plays the role of the axial coordinate:

$$\frac{\partial^2\omega}{\partial x^2}+\frac{\partial^2\omega}{\partial y^2}+\frac{1}{x}\frac{\partial\omega}{\partial x}=0. \tag{1}$$

A standard separation of variables yields fundamental solutions in the form of a product of exponential and Bessel functions:[1]

$$\omega(x,y)=(A_1J_0(x)+A_2Y_0(x))(B_1e^{y}+B_2e^{-y}).$$

The separation of variables can be enriched significantly, if Eq. (1) is brought into a complex form using the complex-conjugate variables $z=x+iy$ and $\bar{z}=x-iy$ and new solutions are sought in the form of a product of functions of z and $\bar{z}$ taken individually.

Using Kolosov's operators[2]

$$\frac{\partial}{\partial z}=\frac{1}{2}\left(\frac{\partial}{\partial x}-i\frac{\partial}{\partial y}\right),\quad \frac{\partial}{\partial\bar{z}}=\frac{1}{2}\left(\frac{\partial}{\partial x}+i\frac{\partial}{\partial y}\right), \tag{2}$$

we write (1) in the following form:

$$\frac{\partial}{\partial\bar{z}}\left(2z\frac{\partial\omega}{\partial z}+\omega\right)+\frac{\partial}{\partial z}\left(2\bar{z}\frac{\partial\omega}{\partial\bar{z}}+\omega\right)=0. \tag{3}$$

The search for solutions of the form $\omega=P(z)Q(\bar{z})$, where $P(z)$ and $Q(\bar{z})$ are unknown analytic functions, leads directly to a separation of variables in Eq. (3):

$$\frac{2zdP/dz+P}{dP/dz}=-\frac{2\bar{z}dQ/d\bar{z}+Q}{dQ/d\bar{z}}=2C, \tag{4}$$

where $C=a+ib$ is the complex separation constant. Both equalities in (4) can be integrated quickly and give the following expressions for P and Q:

$$P(z)=\frac{A_1}{\sqrt{z-C}},\quad Q(\bar{z})=\frac{A_2}{\sqrt{\bar{z}+C}},$$

where A_1 and A_2 are arbitrary complex numbers. The principal part of the solution sought can be written in the form

$$\omega(z,\bar{z})=\varphi+i\psi=\frac{1}{\sqrt{(z-C)(\bar{z}+C)}}$$

$$=\frac{1}{\sqrt{x^2+(y-b+ia)^2}}. \tag{5}$$

It can be seen from (5) that both real Laplace potentials, φ and ψ, have an annular feature with a radius $x=a$ lying in the $y=b$ plane. The specific value of b clearly has no influence on the form of the equipotentials, and we, therefore, set $b=0$. Then,

$$\varphi=\frac{1}{M}\sqrt{\frac{M+x^2+y^2-a^2}{2}},\quad \psi=\frac{1}{M}\sqrt{\frac{M-x^2-y^2+a^2}{2}},$$

$$M(x,y)=\sqrt{(x^2+y^2-a^2)^2+4a^2y^2}. \tag{6}$$

2. PHYSICAL INTERPRETATION OF SOLUTIONS

Figures 1 and 2 present equipotential portraits of φ and ψ. The potential φ describes the field of a grounded conducting disk of radius a, near whose edge there is an infinitely thin ring of charge. In the limit where $a\to 0$ the potential φ degenerates into the potential of a point charge; therefore, at small values of a it is logical to regard the ''disk-ring'' case as a very important variant of the generalization of the field of a point charge. The potential ψ is the spheroidal inverse of φ, and its portrait corresponds to the field of a grounded infinite circular diaphragm of radius a, near whose edge there is an annular filament of charge. Because of mutual induction, the features in both cases have a dipole character.

3. ANNULAR MULTIPOLES

The differentiation of (6) with respect to the axial coordinate y gives two series of potentials with an annular feature of radius a, which should be regarded as a generalization of the point multipoles obtained by the same procedure from the ordinary potential of a Coulomb center. The general formula for these multipoles in complex form is:

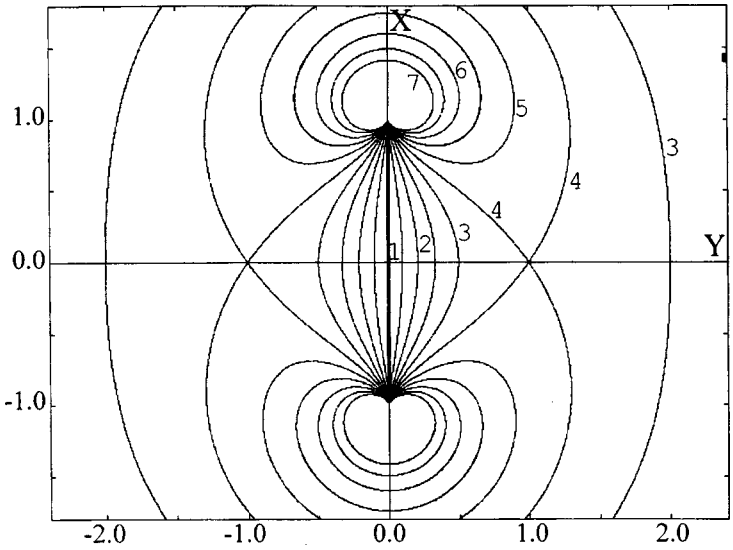

FIG. 1. Equipotential portrait of the harmonic potential φ (disk–charged-ring system). The numbers in the figure correspond to the following potentials: *1* — $\varphi=0.0$, *2* — $\varphi=0.2$, *3* — $\varphi=0.4$, *4* — $\varphi=0.5$, *5* —$\varphi=0.6$, *6* — $\varphi=0.8$, *7* — $\varphi=1.0$.

$$\omega_n=\varphi_n+i\psi_n=\frac{\partial^n}{\partial y^n}\left(\frac{1}{\sqrt{x^2+(y+ia)^2}}\right). \tag{7}$$

For example, a complex annular quadrupole is described by the expression

$$\omega_2=\frac{y+ia}{[x^2+(y+ia)^2]^{3/2}}.$$

As $a\to 0$, the generalized complex multipoles transform into classical multipoles of the same order.

4. APPLICATIONS

It was shown in Ref. 3 that the motion of charged particles in a field with a potential in the form of a linear superposition with arbitrary coefficients

$$V(x,y)=\alpha\varphi+\beta\psi \tag{8}$$

reduces to an additive separation of variables in the Hamilton–Jacobi equation in spheroidal coordinates. A separation of variables also occurs in the Schrödinger equation with the potential function (8). This fact can be productively utilized to devise new quantum-mechanical models in solid-state physics. In addition, the generalized Coulomb center φ can be employed in the synthesis of an energy analyzer of the deflector type, which generalizes the classical spherical deflector. The potential ψ corresponds physically to a variant of a single lens consisting of a grounded diaphragm, whose opening is adjacent to a torus with an almost circular cross section charged to a certain potential. This lens is remarkable because the course of trajectories in it can be described exactly in elliptic functions not only in the paraxial region,[4] but also in all space,[3] and such a situation usually facilitates the synthesis of systems for transporting hollow conical beams in energy analysis. The basis set of annular multipoles with an elementary representation together with the known classical field structures, viz., the fields of coaxial cylinders, concentric spheres, hyperboloids of revolution, etc., permits the

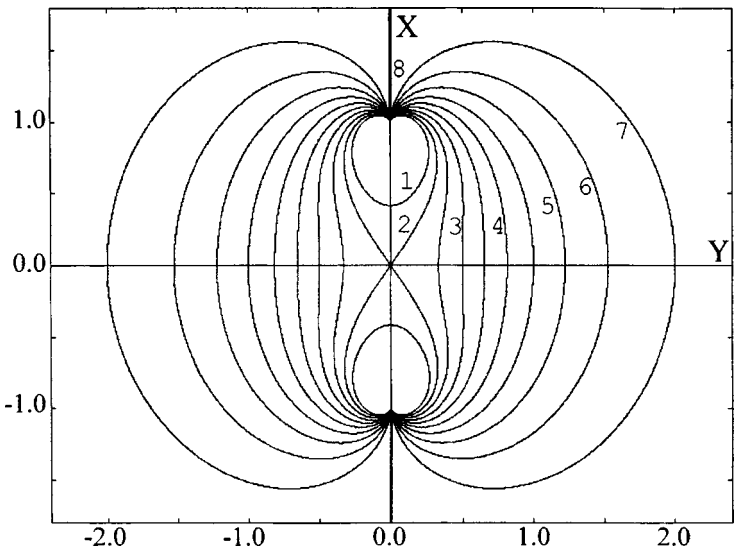

FIG. 2. Equipotential portrait of the harmonic potential ψ (diaphragm–charged-ring system). The numbers in the figure correspond to the following potentials: *1* — $\psi=-1.1$, *2* — $\psi=-1.0$, *3* — $\psi=-0.8$, *4* — $\psi=-0.6$, *5* — $\psi=-0.4$, *6* — $\psi=-0.3$, *7* — $\psi=-0.2$, *8* — $\psi=0.0$.

synthesis of electron-optical systems for various purposes, primarily electrostatic energy analyzers and lens systems for transporting hollow and solid beams. Under the proposed approach there is no need to solve complicated boundary-value problems; therefore, trajectories can be calculated with high speed and accuracy.

[1] I. N. Vekua, *Generalized Analytic Functions*, Addison–Wesley, Reading, MA (1962) [Russ. original, Fizmatgiz, Moscow (1959)].

[2] A. N. Tikhonov and A. A. Samarskii, *Equations of Mathematical Physics*, Pergamon Press, Oxford (1964) [Russ. original, 4th ed., Nauka, Moscow (1953)].

[3] Yu. K. Golikov, ''Determination of electric fields from assigned characteristics of the motion of charged and dipole particles,'' Doctoral dissertation, Leningrad (1984).

[4] W. Glaser, *Grundlagen der Elektronenoptik*, Springer, Vienna (1952) [Russ. transl., Gostekhizdat, Moscow (1957)].

Translated by P. Shelnitz

Predetonation luminescence spectrum of thallium azide

B. P. Aduev, É. D. Aluker, A. G. Krechetov, A. Yu. Mitrofanov, A. B. Gordienko, and A. S. Poplavnoĭ

Kemerovo State University

(Submitted August 29, 1998)
Pis'ma Zh. Tekh. Fiz. **25**, 28–30 (May 12, 1999)

The time-resolved predetonation luminescence spectrum of thallium azide is measured by the ''spectrum-during-a-pulse'' method. Good agreement between the spectrum obtained and the results of a theoretical calculation of the valence-band density of states of TlN_3 is noted.
 [S1063-7850(99)00505-4]

In Refs. 1 and 2 we measured the predetonation luminescence spectra of the azides of silver and lead. Both of these materials are characterized by the presence of two peaks: the first peak is at 2.25 eV for AgN_3 and at 2.1 eV for PbN_6, and the second peak is at 1.45 and 1.5 eV, respectively. The present study, which is a continuation of the work in Refs. 1–3, is devoted to measuring the predetonation luminescence spectrum of TlN_3.

The measurements were performed on the setup in Ref. 3, which was modified to record time-resolved luminescence spectra from a single sample in the wavelength range 500–1000 nm.

Thallium azide in the form of pellets of thickness 300 -400 μm and diameter 10 mm, which were obtained by compacting powered TlN_3 under a pressure of 4×10^4 Pa following its synthesis by two-jet crystallization, served as the samples for study.

Unlike the spectra of AgN_3 and PbN_6, the predetonation luminescence spectrum of thallium azide contains four peaks at 2.35, 1.9, 1.65, and 1.4 eV.

In Ref. 4, we proposed a model of the predetonation luminescence of heavy-metal azides, according to which such luminescence is caused by optical transitions of valence-band electrons to a quasilocal level formed deep in the valence band as the explosive decomposition chain reaction proceeds. The experimental results concerning the predetonation luminescence spectrum $N_2(E)$ of thallium azide, which can be interpreted on the basis of this model, are compared in Fig. 1 with new calculations of the valence-band density of states $N_1(E)$.

The calculations were performed self-consistently in the local density-functional formalism using first-principles norm-conserving separable pseudopotentials. To construct an LCAO representation of the single-particle functions of the

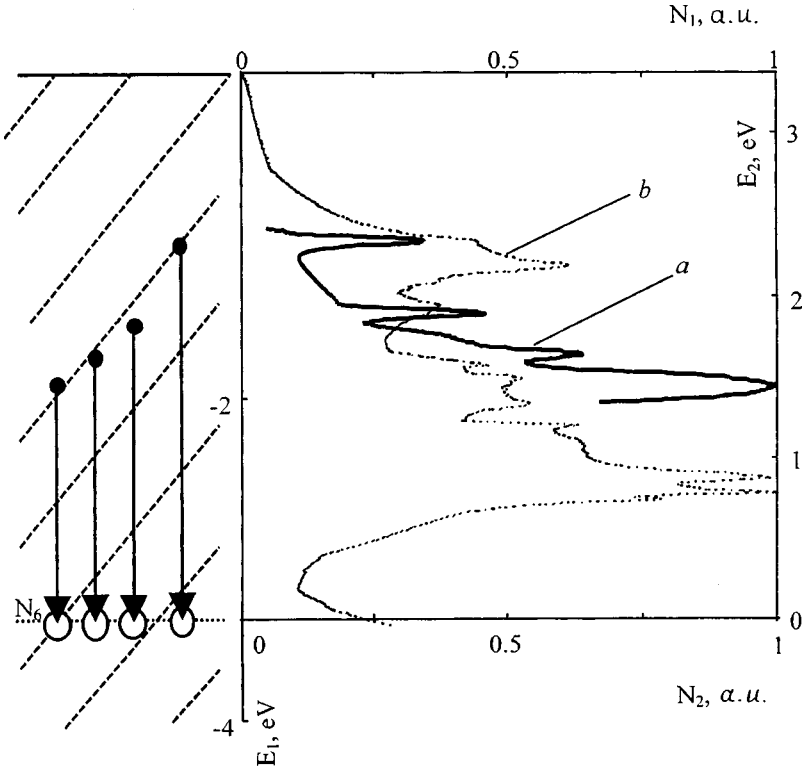

FIG. 1. Comparison of the predetonation luminescence spectrum (a) with the calculated valence-band density of states (b): N_1, E_1 — scales for the density of states ($E_1=0$ — top of the valence band); N_2, E_2 — scales for the luminescence spectrum; N_6 — position of the level of the quasilocal state providing the best correlation between the predetonation luminescence spectrum and the density of states. Vertical arrows — optical transitions of valence-band electrons to the quasilocal state.

crystal for all the types of atoms (Tl and N), we used a basis set consisting of their pseudoatomic eigenfunctions of the *s*, *p*, and *d* types, whose radial parts were determined by solving the corresponding ''pseudoatomic'' equations and then finding analytical representations for them.[5,6] According to the calculation procedure,[7] plane waves with energies up to 33.6 Ry and a total number up to 2800 were taken into account in forming the secular equations. To calculate $N_1(E)$ with good resolution (~ 0.01 eV), the energy spectrum $E_n(\mathbf{k})$ was calculated on a fairly dense $\mathbf{k}$ grid covering the Brillouin zone ($\sim 10^4$ points).

A comparison of the experimental and calculated data reveals that the best agreement between the predetonation luminescence spectra and the valence-band density of states is obtained if the short-wavelength maximum in the predetonation luminescence spectrum $N_2(E)$ is located on the ''shoulder'' of $N_1(E)$ at ~ 2.2 eV from the top of the valence band, which corresponds to a depth of the quasilocal level within the band equal to ~ 3.4 eV.

In our opinion, the results presented in this paper, together with the results previously published in Refs. 1 and 2, can be regarded as weighty evidence of the faithfulness of the model of the predetonation luminescence of heavy-metal azides proposed in Ref. 4.

This work was carried out with the support of the Russian Fund for Fundamental Research (Grant No. 98-03-32001) and a Grant from Ministry of General and Professional Education of the Russian Federation.

[1] B. P. Aduev, É. D. Aluker, and A. G. Krechetov, Pis'ma Zh. Tekh. Fiz. **22**(6), 24 (1996) [Tech. Phys. Lett. **22**(3), 236 (1996)].
[2] B. P. Aduev, É. D. Aluker, Yu. A. Zakharov, A. G. Krechetov, and I. V. Chubukin, JETP Lett. **66**, 111 (1997).
[3] B. P. Aduev, É. D. Aluker, A. G. Krechetov, and Yu. P. Sakharchuk, Pis'ma Zh. Tekh. Fiz. **24**(16), 31 (1998) [Tech. Phys. Lett. **24**(8), 636 (1998)].
[4] B. P. Aduev, É. D. Aluker, G. M. Belokurov, and A. G. Krechetov, Khim. Fiz. **16**(8), 130 (1997).
[5] A. B. Gordienko and A. S. Poplavnoĭ, Izv. Vyssh. Uchebn. Zaved. Fiz. No. 1, 54 (1995).
[6] A. B. Gordienko and A. S. Poplavnoĭ, Phys. Status Solidi B **202**, 941 (1997).
[7] S. Louie, K.-M. Ho, and M. L. Cohen, Phys. Rev. B **8**, 5747 (1973).

Translated by P. Shelnitz

Criterion for fatigue failure in steels

L. B. Zuev, V. V. Murav'ev, and Yu. S. Danilova

Institute of the Physics of Strength and Materials Science, Russian Academy of Sciences, Siberian Branch, Tomsk;
Siberian State University of Ways of Communication, Novosibirsk
(Submitted November 27, 1998)
Pis'ma Zh. Tekh. Fiz. **25**, 31–34 (May 12, 1999)

A formal criterion for fatigue failure in steels, which permits reliable detection of the transition to the final stage of the process on the basis of the form of the dependence of the propagation velocity of ultrasonic waves in them on the number of loading cycles and the derivatives of this function with respect to the number of cycles, is established. The nature of the phenomena associated with the variation of the ultrasound velocity during the accumulation of fatigue damage is analyzed. © *1999 American Institute of Physics.* [S1063-7850(99)00605-9]

Fatigue failure usually occurs unexpectedly, and the prediction of service life[1,2] using fatigue curves is based on statistical models, i.e., it permits only a probabilistic, rather than a deterministic, estimation of the service life of a specific part. Estimation of the residual life of a part is especially difficult when there is fatigue, and thus the most complicated problem associated with fatigue failure is predicting its approach for an individual object. Such a problem is usually solved with the use of various complicated techniques for the early detection of fatigue microcracks.[3]

This paper proposes a formal criterion for fatigue failure, which is suitable for individual objects, on the basis of previously performed[4–6] investigations of the ultrasound propagation velocity in fatigue-loaded samples. It was established in Refs. 4–6 that the ultrasonic wave propagation velocity drops continuously during cyclic loading as the number of loading cycles N rises, as is shown in Fig. 1a. The total decrease in velocity up to the moment of failure is no greater than $3\times10^{-2}-3.5\times10^{-2}$, whichplaces fairly high requirements on the procedures and techniques for measuring this quantity.[7] The relative velocity change $V^*=V/V_0$ (V_0 is the velocity before the beginning of fatigue testing, and V is the velocity after N loading cycles) is a function of N, and, for example, has a three-stage form for a whole series of steels. The transition from one stage to another is determined both by the type of material and the loading conditions.

The relationship between this dependence and the state of the material is fairly clear. Microscopic examinations[5] showed that while there are no appreciable structural changes in the first stages, microcracks measuring up to 0.1 mm are observed in the last stage. The onset of the third stage of the $V^*(N)$ curve clearly signals the approach of failure. In fact, direct experiments performed on 40, 40Kh, 30KhGSA, rail, and other steels showed that one sample reaching such a state has undergone only $\sim$250 loading cycles, while the duration of the first two stages at the same loading amplitude can be as long as 10^4 cycles.

The use of plots of the type shown in Fig. 1a to predict fatigue failure is possible, but it does not provide the accuracy needed, since the ultrasound propagation velocity decreases continuously over the course of the entire loading process, differing only with respect to the rate of decrease in the different stages of the process, so that it is difficult to fix

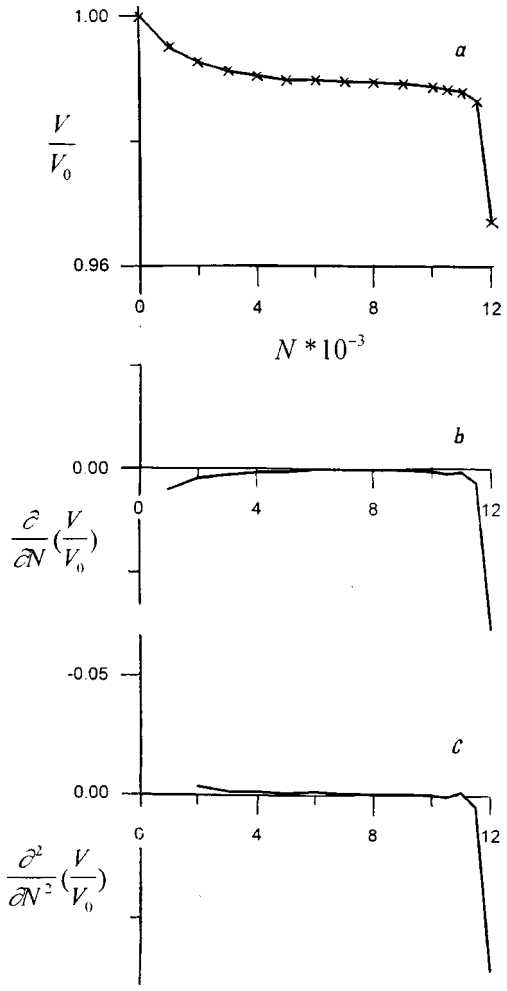

FIG. 1. a — Dependences of the velocity of sound in samples of steel 45 on the number of loading cycles $V^*(N)$ (asymmetric cycle, amplitude equal to 200 MPa, and a loading frequency equal to 1 Hz). b — The first derivative $\partial V^*/\partial N=\xi_1(N)$. c — The second derivative $\partial^2 V^*/\partial N^2=\xi_2(N)$.

the time of passage from the second stage to the third. It can be shown that the behavior of the first and second derivatives of V^* with respect to N, i.e., $\xi_1 = \partial V^*/\partial N$ and $\xi_2 = \partial^2 V^*/\partial N^2$, respectively, as a function of the number of loading cycles N is more informative, as can be seen in Figs. 1b and 1c.

The form of the plot of $\xi_1(N)$ mimics the U-shaped failure rate curve known in engineering reliability theory,[8] but adapts it to the case of an individual part.[4] Thus, it can be assumed that the initial drop in the value of the ultrasound velocity corresponds to the processes responsible for preworking failures, that processes leading to random failure are responsible for the drop in the rate in the second stage, and that, finally, the decrease in the ultrasound velocity in the third stage has the same causes as wear failures.[4] The last stage is most dangerous, since, as microscopic examinations have shown,[5] incipient microcracks, which serve as foci for brittle failure, appear at its onset.

The behavior of the second derivative $\xi_2(N)$ is especially informative, since it clearly changes sign upon transition to the final stage of the process (see Fig. 1c). This distinctly discernible moment fixes the onset of the most dangerous stage of fatigue failure, so that the following qualitative criterion for the transition to the critical stage of fatigue loading can be formulated: the service life of a part is essentially exhausted when

$$\xi_2 = \partial^2 V^*/\partial N^2 = \partial^2 (V/V_0)/\partial N^2 > 0, \quad (1)$$

while the condition $\xi_2 \leqslant 0$ corresponds to a fairly large reserve of fatigue life for the part or sample.

It is noteworthy that while the duration of the fatigue failure process for different samples of the same material can differ by almost two fold, the transition to the critical stage occurs essentially always when $V^* \approx 0.98$. Thus, the condition $V^* \leqslant 0.98$ can also be regarded as a criterion for the approach of fatigue failure.

The practical employment of the proposed criterion (1), which is based on measurements of the ultrasound propagation velocity, is possible at the time of repairs or technical servicing and does not require a preliminary measurement of the ultrasound velocity in the unloaded part. The critical stage of the process can be detected by observing a change in the sign of the derivative $\xi_2(N)$ during a small number of additional loading cycles.

[1] V. S. Ivanova, *Fatigue Failure of Metals* [in Russian], Metallurgizdat, Moscow (1963).
[2] A. J. Kennedy, *Processes of Creep and Fatigue in Metals*, Oliver and Boyd, Edinburgh (1962) [Russ. transl., Metallurgiya, Moscow (1965)].
[3] R. A. Collacott, *Mechanical Fault Diagnosis and Condition Monitoring*, Chapman and Hall, London; Wiley, New York (1977) [Russ. transl., Mir, Moscow (1989)].
[4] L. B. Zuev, V. Ya. Tsellermaer, V. E. Gromov *et al.*, Zh. Tekh. Fiz. **67**(9), 123 (1997) [Tech. Phys. **42**, 1094 (1997)].
[5] L. B. Zuev, D. Z. Chirakadze, O. V. Sosnin *et al.*, Mekh. Nizk. Temp. **19**(8), 80 (1997).
[6] L. B. Zuev, O. V. Sosnin, D. Z. Chirakadze *et al.*, Prikl. Mekh. Tekh. Fiz. **39**(4), 180 (1998).
[7] V. V. Murav'ev, L. B. Zuev, and K. L. Komarov, *Velocity of Sound and the Structure of Steels and Alloys* [in Russian], Nauka, Novosibirsk (1996).
[8] B. S. Dhillon and C. Singh, *Engineering Reliability: New Techniques and Applications*, Wiley, New York (1981) [Russ. transl., Mir, Moscow (1984)].

Translated by P. Shelnitz

Acoustic field created by radial oscillations of a portion of a cylindrical channel in the medium within the channel

I. A. Kolmakov

(Submitted April 17, 1998)
Pis'ma Zh. Tekh. Fiz. **25**, 35–41 (May 12, 1999)

An explanation for the formation of plane waves traveling in opposite directions from a region with cylindrical waves in the medium within a channel is presented. The problem of the form of the region generating the plane waves and the problem of the field formed near that region are solved. The results obtained can be useful for technical applications. © *1999 American Institute of Physics.* [S1063-7850(99)00705-3]

Radial oscillations of the walls of a cylindrical channel of infinite length (i.e., oscillations along the radius) produce waves which propagate only in the radial direction in the medium filling the channel.[1] When the walls of a finite segment of a channel oscillate, the region with cylindrical waves created by the segment generates longitudinal waves, which travel in opposite directions from its end surfaces. The experiments in Ref. 2 revealed that such waves are not normal waves, since the characteristic distributions of the acoustic parameters, i.e., pressures, densities, etc., for normal waves, which are proportional to Bessel functions of the form $J_i(\kappa r)$, were not observed. In particular, measurements of the amplitude of the acoustic pressure showed that the waves formed at a certain distance from the radial end plane bounding the region with cylindrical waves closely resemble plane waves. There is presently no explanation for their formation or any hypothesis regarding the mechanism for the generation of such waves; nevertheless, the investigation of these questions is very important for applied problems.

This paper gives probably the only possible explanation for the essence of the generation of traveling plane waves by a region with cylindrical waves. A mechanism for conversion of the energy of cylindrical waves converging toward the longitudinal axis into direct longitudinal motion of the medium, which creates a field of plane waves, is systemically developed and investigated. For greater simplicity, the dissipation of energy is not taken into account.

It is already clear from the foregoing that the formation of longitudinal plane waves from cylindrical waves is caused by the presence of a sharp boundary between two regions with different acoustic energy densities: the region with cylindrical waves and the region without such waves adjoining it on each of its end surfaces. Because the pressure in a wave is greater than the undisturbed pressure, i.e., $P>P_0$, motion of the medium from the region with the cylindrical waves through an end surface should appear. However, as calculations show, the energy lost as a result has a value significantly smaller than the values obtained experimentally, i.e., the latter cannot appear as a result of the transmission of acoustic energy through the wave end surfaces alone. Appreciable conversion of the energy of cylindrical waves into the energy of plane waves is apparently possible only when the cylindrical waves have a nonzero axial (longitudinal) wave-vector component K_z. The formation of a z component is possible when the front of a cylindrical wave is bent. The bending of the wave front should, in fact, take place already because of the previously mentioned pressure drop at the wave end surface, which creates a longitudinal pressure in the region without cylindrical waves. It can be shown that such energy ''movement'' slows the motion of the wave (the slowing is proportional to the energy transfer rate). This also accounts for the retardation and, thereby, the bending first of the end portion of a cylindrical wave and then of the parts more distant from its end surfaces.

Figure 1 (left-hand part) shows wave profiles formed by a plane intersecting cylindrical waves at various moments in time. Profile *1* corresponds to the initial moment, when the wall of the emitting segment of the channel (W) has just formed a cylindrical wave and the ''bending'' angle θ of the front is still close to zero. When the bulk of the wave front reaches the OZ axis (focusing), the angle θ reaches its maximum value, since the intensity of the cylindrical wave increases with decreasing radius, and a region bounded by the conic surface of the cylindrical wave, i.e., the $Od'd$ ''cone,'' forms in the bent end portion of the front bounded by the radial OR_0 and Z_0Z' planes. Profile *2* corresponds to this moment. Then the character of the motion of the front changes: the points of the profile in the Z_0Z' plane continue their motion toward the OZ axis, while the points in the OR_0 plane reverse their direction of motion. As a result, at a certain time the profile of the diverging cylindrical wave *2′* is the ''mirror image'' of profile *2* of the wave converging toward the axis. In the case under consideration the wave vector **k** of the cylindrical wave is perpendicular to the surface of the front at all points. Therefore, bending of the front (which is negligibly small) appears, in principle, already at the time of formation of the cylindrical wave. However, the longitudinal component is effectively realized only within the cone.

Let us examine the motion of the medium in the cone during compression of the ''conical piston'' after first making several simplifying assumptions. We assume that the medium in the cone is incompressible, that the angle θ at the apex of the cone does not vary during compression, that the

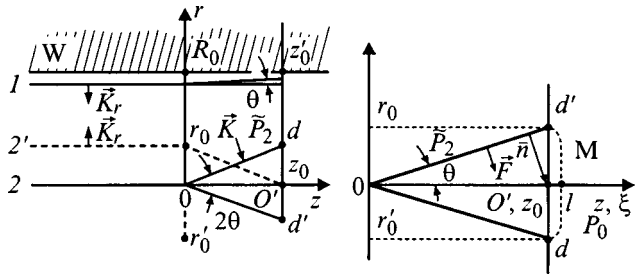

FIG. 1.

rate of propagation (motion) of the cone surface is constant and equal to the velocity of sound c, that the cone generatrices Od' and Od (see Fig. 1), therefore, move to the right along the normal **n** with the constant velocity c, that the points r_0 and r_0' move along the radii r_0O and $r_0'O$, the apex O moves along the OZ axis, and they have the velocities $v_z=c(\sin\theta)^{-1}$ and $v_r=c(\cos\theta)^{-1}$ andconverge at the point O' simultaneously, and that the pressure exerted by the front on the medium in the cone $\tilde{P}_2=P_{20}-P_0=\text{const}$ (P_0 is the undisturbed pressure, and P_{20} is the acoustic pressure) over the course of the entire time of ''compression'' of the cone into a point, i.e., τ_0. The basis for these assumptions is as follows. The compressibility in the near-axial region is small even for gases; therefore, taking it into account would lead to corrections of the order of $v_z^{-1}\cdot c\ll 1$; the constancy of P_2 and c during the time τ_0 can be estimated by a correction of the same order of magnitude. We note that the ''displacement'' of part of the medium from the cone will continue until the force exerted by the end surface of the cone becomes equal to the sum of two forces, viz., the drag of the region M formed by the medium displaced from the cone and the pressure P_0 (see Fig. 1, right-hand part). Let us next consider the effect of the forces in the cone. The vector of the force **F** exerted by the conical surface on the medium is directed along a normal to it. Because of the axial symmetry, the radial components of **F** compensate one another, and the longitudinal components create motion along the OZ axis. Thus, the force exerted on the medium by the cone surface $\mathbf{F}=P_2S_{\text{l.s.}}\cdot\mathbf{n}$, where $S_{\text{l.s.}}$ is the area of the lateral surface of the cone and **n** is a normal to it, induces motion of the medium through the end surface r_0r_0' at a distance z_0 from the origin of coordinates with the velocity

$$v_z(z_0)=\frac{3\tilde{P}_2t}{(\rho_0\cos\theta)\cdot\mathbf{r}}. \tag{1}$$

The dynamics of the region $z_0r_0lr_0'\equiv M$ (see Fig. 1, right-hand part) formed by the medium displaced from the cone can be described using the hydrodynamic equations of an incompressible fluid in cylindrical coordinates

$$\frac{\partial v_z}{\partial t}+v_r\frac{\partial v_z}{\partial r}+\frac{1}{2}\frac{\partial v_z^2}{\partial z}+\frac{1}{\rho_0}\frac{\partial P}{\partial z}=0, \tag{2}$$

$$\frac{\partial v_r}{\partial t}+v_z\frac{\partial v_r}{\partial z}+\frac{1}{2}\frac{\partial v_r^2}{\partial r}+\frac{1}{\rho_0}\frac{\partial P}{\partial r}=0, \tag{3}$$

$$\frac{\partial v_r}{\partial r}+\frac{v_r}{r}+\frac{\partial v_z}{\partial z}=0 \tag{4}$$

(ρ_0 is the density of the incompressible medium) and the boundary condition (1). The main points in the solution are as follows. From (4) we obtain expressions for the radial (v_r) and longitudinal (v_z) flow velocities of the medium (outside the cone) in terms of an arbitrary function of time $f(t)$:

$$v_r=\frac{r}{2}\cdot f(t), \tag{5}$$

$$v_z=-z\cdot f(t). \tag{6}$$

Integrating (2) and (3) first over r in the range from $R(t)$ to R_0 and then over z from $Z(t)$ to ∞, where $R(t)$ and $Z(t)$ are points on the surface of region M, and taking into account (5) and (6), for the rate of motion of the boundary (points on the surface) of region M we obtain

$$\frac{\partial V_z^2}{\partial Z}+\frac{V_z^2}{Z}\left\{1+\frac{3R_0^4+4R(R_0^3-R^3)}{2R(R_0^3-R^3)}\right\}=-\frac{12R_0^3}{Z(R_0^3-R^3)}\cdot\frac{P_0-P(R,Z)}{\rho_0}, \tag{7}$$

$$\frac{\partial V_r^2}{\partial R}+6\frac{V_r^2}{R}=-\frac{2}{R\cdot\ln RR_0^{-1}}\cdot\frac{P_0-P(R,Z)}{\rho_0}, \tag{8}$$

where $V_z=dZ(t)/dt$, $V_r=dR(t)/dt$, and $P(R,Z)$ is the pressure on the boundary of M. Solving Eqs. (7) and (8) under the boundary condition (1) gives

$$V_z=v_z(z_0)\left(\frac{Z}{Z_0}\right)^{\frac{3}{2}}\cdot\left(\frac{m_1z_0^2+m_2}{m_1z^2+m_2}\right)^{\frac{3}{8}N}, \tag{9}$$

$$V_r=v_z(z_0)\frac{R}{2}\cdot\left(\frac{Z}{Z_0^3}\right)^{\frac{1}{2}}\cdot\left(\frac{m_1z_0^2+m_2}{m_1z^2+m_2}\right)^{\frac{3}{8}N}, \tag{10}$$

where $m_1=R_0^3-R^3$, $m_2=3R_0^3R^2\ln RR_0^{-1}$, and $N=R_0^4[R(R_0^3-R^3)]^{-1}$. From formulas (9) and (10) we can determine the expressions for $Z(t)$ and $R(t)$:

$$Z(t)=z_0+\frac{1}{2}v_z(z_0)t\left(\frac{c_0}{R^2z_0}\right)^{\frac{3}{2}}\left(\frac{m_1z_0^2+m_2}{m_1c_0^2R^{-4}+m_2}\right)^{\frac{3}{8}N}, \tag{11}$$

$$R(t)=r_0+\frac{1}{4}v_z(z_0)t\left(\frac{c_0}{Z}\right)^{\frac{1}{2}}\left\{\left[R_0^3-\left(\frac{c_0}{Z}\right)^{\frac{3}{2}}\right]+3\frac{R_0^2c_0}{Z}\ln\left[R_0^{-1}\left(\frac{c_0}{Z}\right)^{\frac{1}{2}}\right]\right\}^{\frac{3}{8}N}, \tag{12}$$

where $c_0=r_0^2z_0-c^3t^3(\sin\theta\cdot\cos^2\theta)^{-1}$.

Assigning the external impulse $\tilde{P}_2(t)$, we can use (11) and (12) to reconstruct the form of the surface of the region

M in the arbitrary moments in time t_i, and taking into account (9) and (10), we can determine the values of the velocities of $V(t_i)$ points on the surface of M.

The second part of the problem is to find the field created by the axial ''source'' (the region M) outside its boundaries, i.e., when the condition on the boundary (the surface of M) is assigned by (9) and (10) and the surface itself is specified by (11) and (12). It is difficult to obtain an approximate analytical solution of the problem in such a formulation, and numerical solutions would probably be more expedient in this case. An analytical solution is still possible, but for disturbances of an acoustic scale, i.e., for the case where the volume of the region M is small compared with the volume of the cone $Z(t)\cdot z_0^{-1}$ and $R(t)\cdot r_0 \ll 1$. The mean velocity of the region M and the medium in it during the lifetime τ_0 of the region for a not very small amplitude of the external signal is supersonic, i.e., $V_z > c$. The radial velocities are small and shall henceforth not be taken into account. It can be shown with consideration of the assumptions made that the motion of the region M is approximated ''well'' by the motion of a disk of radius r_0 with a constant velocity V_z during the time τ_0 and a distribution of the form $\exp(-r^2 r_0^{-2})$. The energy losses accompanying the motion of the disk are proportional to its drag and determine the level of the disturbances generated. Under such motion a weak discontinuity surface, which resembles an ellipsoid of revolution and ends on the internal surface of the channel, forms in front of the disk.

In a cylindrical coordinate system moving with a velocity $V_z > c$ along the OZ axis the problem of the field created by a flat disk reduces to the solution of the wave equation

$$\frac{\partial^2 \rho'}{\partial r^2} + \frac{1}{r}\frac{\partial \rho'}{\partial r} + \gamma^2 \frac{\partial^2 \rho'}{\partial \xi^2} = \frac{1}{c^2}\,\mathrm{div}\,\mathbf{f}, \tag{13}$$

where $\xi = z - V_z t$, $\gamma^2 = 1 - V_z^2 c^{-2}$, $\mathbf{f} = \mathbf{e}_z \alpha_0 S \rho V_z^2 \times \exp(-r^2 r_0^{-2})\delta(\xi)$, S is the area of the disk, $\delta(\xi)$ is a Dirac delta function, $\mathbf{e}_z$ is the unit vector along OZ, and α_0 is the drag coefficient.

The solution of Eq. (13) obtained using integral transformations of the Fourier-Hankel type and the properties of cylindrical functions[3,4] with consideration of the conditions at infinity has the form

$$\rho' = N \frac{\xi}{(\xi^2 - \gamma^2 \tilde{r}^2)^{3/2}} \cdot \left[1 - \frac{3}{4} r_0^2 \gamma^2 \cdot \frac{(2\xi^2 + 3\gamma^2 \tilde{r}^2)}{(\xi^2 - \gamma^2 \tilde{r}^2)^2} \right], \tag{14}$$

where $\tilde{r} = r - r_0$ and $N = (\pi + 2)(2\pi)^{-1} \rho V_z^2 c^{-2} \cdot S$.

Equation (14) also specifies the field created by the end portion of a converging cylindrical wave. The expression for the shape of the weak discontinuity surface can be obtained from (14), for example, using the condition for an extremum $(\partial\rho/\partial\xi) = 0$; however, a sixth-order equation must then be solved. The points of intersection of the surface with the coordinate axes 0ξ and $0r$ are determined at once. In particular, the points of intersection of the surface with the 0ξ coordinate axis are always located in front of the disk ($V_z > c$) at distances $\xi > r_0$, which increase with increasing V_z.

Thus, an explanation for the appearance of longitudinal plane waves has been given, and a detailed substantiated description of the mechanism for their formation has been presented. Formulas have been derived, which can be used, if the external signal is assigned in the required form, not only to predict and reproduce the expected experimental picture of the wave field formed in a channel, but also to solve the problem of optimizing various systems, for example, an emitter–communication-channel–receiver system, and other problems. The results in the present communication can be useful for technical applications.

[1] L. D. Landau and E. M. Lifshitz, *Fluid Mechanics*, 2nd ed., Pergamon Press, Oxford (1987) [Russ. original, Nauka, Moscow (1986), 733 pp.].
[2] I. A. Kolmakov, Akust. Zh. **42**, 721 (1996) [Acoust. Phys. **42**, 635 (1996)].
[3] N. S. Koshlyakov, É. B. Gliner, and M. M. Smirnov, *Differential Equations of Mathematical Physics*, North-Holland, Amsterdam (1964) [Russ. original, Fizmatgiz, Moscow (1962), 767 pp.].
[4] H. Jeffreys and B. Swirles, *Methods of Mathematical Physics*, 3rd ed., Cambridge University Press, Cambridge (1966) [Russ. transl., Mir, Moscow (1970), Vol. 3, 344 pp.].

Translated by P. Shelnitz

One-component cesium magnetometer for measuring the residual magnetic induction in ferromagnetic shields

N. A. Dovator

A. F. Ioffe Physicotechnical Institute, Russian Academy of Sciences, St. Petersburg
(Submitted April 30, 1998; resubmitted January 11, 1999)
Pis'ma Zh. Tekh. Fiz. **25**, 42–46 (May 12, 1999)

A simple design for a miniature cesium magnetometer intended for measuring the residual magnetic induction ($B_0 \leqslant 1000$ nT) in ferromagnetic shields of cylindrical shape with an internal diameter $\varnothing \geqslant 15$ mm is described. © *1999 American Institute of Physics.*
[S1063-7850(99)00805-8]

Unlike quantum magnetometers of the S_z and S_x types, which are based on double radio-optical resonance (DROR),[1] a one-component cesium magnetometer has been created using a nonresonant principle for forming a signal that is proportional to the longitudinal (along the optical axis of the magnetometer) component of the magnetic induction.[2] This principle for constructing magnetometers was chosen because it is difficult to measure weak magnetic fields in the range from -1000 to $+1000$ nT with only one type of quantum magnetometer based, for example, on the use of either a DROR signal ($100-1000$ nT) or a parametric resonance signal in an ensemble of optically oriented atoms ($0-10$ nT).[3,4]

The operation of the cesium magnetometer described here is based on utilization of the dependence of the polarization of atoms subjected to the action of circularly polarized optical pump radiation on the angle between the direction of the magnetic field and the pump radiation beam. Under stationary conditions the expression for the magnetization of an atomic ensemble (along the pump beam) has the form:[3]

$$M = M_0 \frac{1+\gamma^2 B_0^2 \tau_2^2}{1+\gamma^2 B_0^2 \tau_2^2 + \gamma^2 B_1^2 \tau_1 \tau_2}, \tag{1}$$

where M_0 is the magnetization created by the pump radiation in the absence of a magnetic field, B_0 and B_1 are the values of the longitudinal and transverse (relative to the pump beam) components of the magnetic induction, γ is the gyromagnetic ratio, and $\tau_{1,2}$ are the longitudinal and transverse relaxation times of the atomic magnetization (with allowance for optical relaxation). It follows from (1) that a plot of $M(B_0)$ has the form of a symmetric curve with a minimum at $B_0 = 0$. Therefore, by modulating B_0 using an additional magnetic field with the induction $B_M \cos \Omega_M t$ ($\Omega_M \ll \tau_{2,1}^{-1}$) directed along the optical axis of the magnetometer, we obtain the variable component of the magnetization M^{Ω_M}. Its amplitude and phase depend on the magnitude of the magnetic induction B_0 and its direction (parallel or antiparallel to the pump beam). Since the absorption of the pumping radiation by an ensemble with optically oriented atoms is $\delta S \sim (M_0 - M)$,[1] a magnetic field sensor including a pump lamp, a cell with cesium, a modulation coil, and a photodetector (Fig. 1) can serve as a null indicator for the longitudinal component of the magnetic induction (Fig. 2). An autocompensation system for a quantum magnetometer (Fig. 1) was also assembled on the basis of such a null indicator. For this purpose an error signal in the form of the alternating component of the photocurrent (with a frequency $\Omega_M/2\pi = 80$ Hz) was amplified and fed after synchronous detection (in the form of a dc signal) into the modulation coil in the phase in which the longitudinal component of the magnetic induction was zeroed within the cell with oriented atoms. Thus the compensating current (J) was proportional to the value of the induction B_0. The self-adjustment factor (with respect to the magnetic field) attained in this magnetometer was ~ 750. The calibration needed for such a quantum magnetometer ($B_0 = \alpha J$, where J is the indicator current and α is the calibration factor), as well as its testing were performed using an experimental system with stabilization of the magnetic field in the ferromagnetic shield[5] and an alkali-metal–

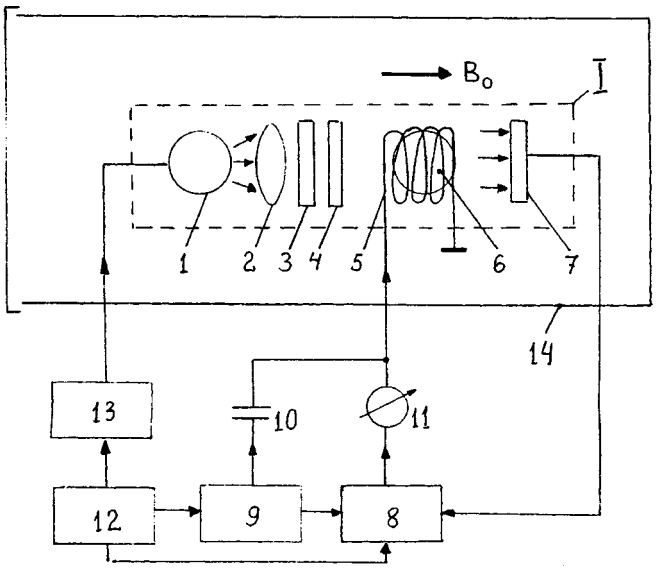

FIG. 1. Block diagram of the cesium magnetometer: *1* — cesium spectral lamp; *2* — lens; *3* — interference filter,which transmits the cesium D_1 line; *4* — circular polarizer; *5* — modulation coil, which also serves as the feedback coil in the self-adjustment system; *6* — working cell; *7* — photodetector; *8* — selective amplifier with a synchronous detector; *9* — low-frequency generator; *10* — separating capacitor; *11* — indicator; *12* — power supply; *13* — high-frequencygenerator for the discharge in the cesium lamp; *14* — ferromagnetic shield.

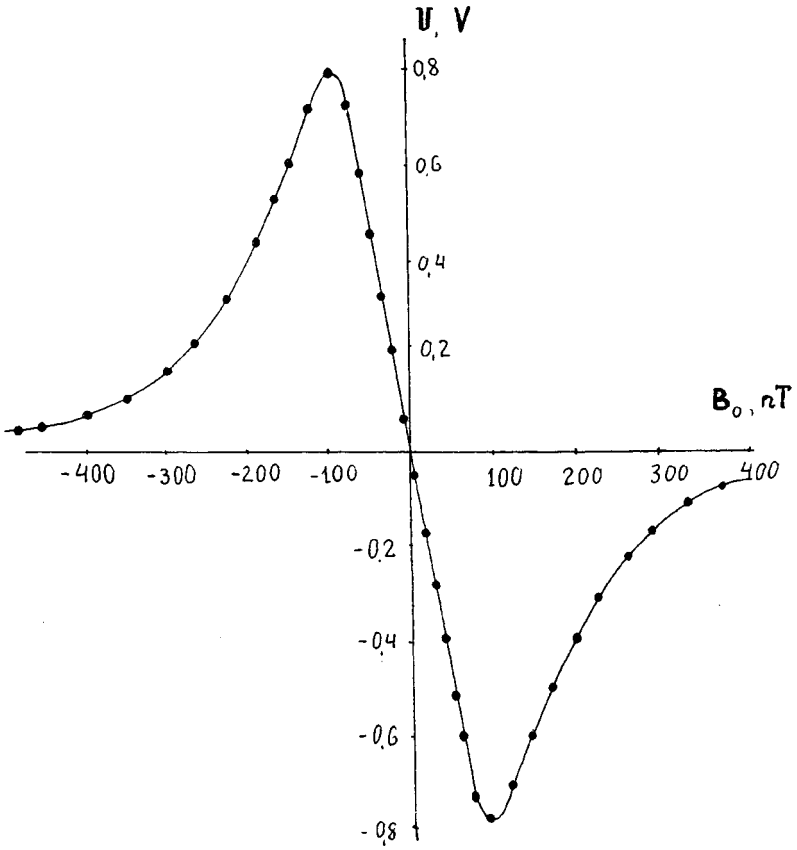

FIG. 2. Output voltage of the synchronous detector with an open feedback loop and $B_1 = 40$ nT.

helium magnetometer,[6] which was certified by the D. I. Mendeleev All-Union Scientific-Research Institute of Metrology.

Several features of the design of the magnetometer just described should be noted. First, its magnetic field sensor has small dimensions ($\varnothing 15 \times 200$ mm), which were achieved by employing a miniature glass cell of spherical shape ($\varnothing 10$ mm) containing cesium vapor (at room temperature) and the buffer gas neon at a pressure of 200 Torr as the working cell, as well as a resonant cesium lamp of similar dimensions and a nonmagnetic version of an FD-24K photodiode. The dimensions of the magnetic field sensor permitted performing measurements of the residual magnetic field and, consequently, the longitudinal shielding factor ($K = B_1/B_2$, where B_1 is the component of the external magnetic field directed along the axis of the cylindrical ferromagnetic shield and B_2 is the analogous component of the residual magnetic field within the shield) for ferromagnetic shields with an internal diameter $\varnothing \geqslant 15$ mm. Second, in order to simplify the design, we dispensed with the forced creation of the transverse magnetic field B_1 needed for the operation of the cesium magnetometer. The fact that such a field is needed can easily be seen from Eq. (1). In fact, setting $B_1 = 0$, we see that $M = M_0$ for any value of B_0, which automatically also implies the absence of an error signal under the conditions of modulation of this quantity. It was found experimentally that the magnetometer functions correctly if $30\ \text{nT} < B_1 < 300$ nT. Under the real conditions under which the measurements of the longitudinal shielding factor of a one- or two-layer ferromagnetic shield (in the earth's magnetic field) were performed it was sufficient to utilize the residual transverse (perpendicular to the axis of the shield) magnetic field within the shield as the transverse field B_1.

The testing of the one-component cesium magnetometer gave the following results: a range for measuring the longitudinal component of the magnetic induction from -1000 to $+1000$ nT[1)] and a sensitivity to variations of the magnetic field as small as 0.02 nT with a measurement error equal to ~ 3 nT.[2)]

[1)]The operating range of a quantum magnetometer is determined by the magnetic-field trapping band, which, as in any static automatic control system, depends on the width of the discriminator characteristic and the transmission factor of the controlling element (in the general case, on the constant of the feedback coil).

[2)]The amount by which the measurement error of the magnetometer described exceeds its sensitivity is determined mainly by the optical shift of the magnetic resonance line of cesium atoms[1] and the error of the calibration needed for this type of magnetometer.

[1] N. M. Pomerantsev, V. M. Ryzhkov, and G. V. Skrotskiĭ, *Physical Principles of Quantum Magnetometry* [in Russian], Nauka, Moscow (1972), 448 pp.
[2] R. E. Slocum, Rev. Phys. Appl. **5**, 109 (1970).
[3] E. B. Aleksandrov, A. M. Bonch-Bruevich, and V. A. Khodovoĭ, Opt. Spektrosk. **23**, 282 (1967) [Opt. Spectrosc. **23**, 151 (1967)].
[4] C. Cohen-Tannoudji, C. Dupont-Roc, J. Haroche, and F. Laloe, Rev. Phys. Appl. **5**, 95 (1970).
[5] E. V. Blinov, S. P. Dmitriev, P. P. Kuleshov, and A. I. Okunevich, in *Abstracts of VSOOAM* [in Russian], FTI, Leningrad (1986), p. 52.
[6] E. V. Blinov, R. A. Zhitnikov, and P. P. Kuleshov, Zh. Tekh. Fiz. **49**, 588 (1979) [Sov. Phys. Tech. Phys. **24**, 336 (1979)].

Translated by P. Shelnitz

Autostochastic ring system of triggers connected through integrating circuits

É. V. Kal'yanov

Institute of Radio Engineering and Electronics, Russian Academy of Sciences (Fryazino Section)
(Submitted October 1, 1998)
Pis'ma Zh. Tekh. Fiz. **25**, 47–51 (May 12, 1999)

A ring system of triggers connected to one another by integrating circuits is studied. Equations for a multiple-trigger ring systems are given, and the results of a numerical analysis for a system containing three triggers are presented. It is shown that chaotic oscillations with switching between two basins of attraction are excited in the ring system considered. The possibility of controlling chaotic oscillations is demonstrated. © *1999 American Institute of Physics.* [S1063-7850(99)00905-2]

Various generators with chaotic dynamics operating in both autonomous[1–7] and nonautonomous[8–13]regimes have been widely investigated in the recent period. Considerable attention has been focused on an autostochastic system with a double-scroll attractor governed by chaotic switchings of oscillations between two basins of attraction[1,4,10–12] This is the reason for the interest in ring systems of triggers connected to one another by integrating circuits. Such a system is examined in this paper. The excitation of chaotic oscillations with a double-scroll attractor is studied by numerical methods, and the possibility of controlling these oscillations is demonstrated.

A schematic representation of an autostochastic ring system containing n triggers ($n=1,2,3\ldots$) is shown in Fig. 1a. A diagram of an individual classical trigger[14] is presented in Fig. 1b. It is formed by the inductance L_n, the resistance R_n, the capacitance C_n, and the nonlinear active element g_n. The elements of the integrating circuit joining adjacent triggers (for example, the triggers T_{n-1} and T_n) in the diagram in Fig. 1a are obvious, i.e., they are the resistance R_n^s and the capacitance C_n^s.

The trigger T_n together with the capacitance C_n^s forms a familiar autostochastic Chua circuit.[1] For this reason, the scheme in Fig. 1a can be regarded as a system of n resistively coupled Chua generators. The latter allows us to expect a possibility of exciting chaotic oscillations with two basins of attraction in the system under consideration.

The ring system illustrated by Figs. 1a and 1b can be described in normalized variables by the following system of $3n$ equations.

$$\dot{x}_1=[\delta_1(y_1-x_1)+\gamma_2(y_2-x_1)-h_1(x_1)]\alpha_1 \tag{1.1}$$

$$\dot{x}_2=[\delta_2(y_2-x_2)+\gamma_3(y_3-x_2)-h_2(x_2)]\alpha_2 \tag{1.2}$$

$$\ldots\ldots\ldots\ldots\ldots\ldots\ldots\ldots\ldots\ldots\ldots\ldots\ldots$$

$$\dot{x}_n=[\delta_n(y_n-x_n)+\gamma_1(y_1-x_n)-h_n(x_n)]\alpha_n \tag{1.n}$$

$$\dot{y}_1=[\delta_1(x_1-y_1)+\gamma_1(x_n-y_1)+z_1]\sigma_1 \tag{2.1}$$

$$\dot{y}_2=[\delta_2(x_2-y_2)+\gamma_2(x_1-y_2)+z_2]\sigma_2 \tag{2.2}$$

$$\ldots\ldots\ldots\ldots\ldots\ldots\ldots\ldots\ldots\ldots\ldots\ldots\ldots$$

$$\dot{y}_n=[\delta_n(x_n-y_n)+\gamma_n(x_{n-1}-y_n)+z_n]\sigma_n \tag{2.n}$$

$$\dot{z}_1=-\beta_1 y_1 \tag{3.1}$$

$$\dot{z}_2=-\beta_2 y_2 \tag{3.2}$$

$$\ldots\ldots\ldots\ldots\ldots\ldots$$

$$\dot{z}_n=-\beta_n y_n, \tag{3.n}$$

where the variables x_i, y_i, and z_i ($i=\overline{1,n}$) are proportional, respectively, to the voltages on the capacitances C_i and C_i^s (the variables x_i and y_i) and the current in the inductance L_i (the variable z_i). A dot over a variable in the system (1)–(3) denotes differentiation with respect to the time t. The function $h_i(x_i)$ describes a nonlinear characteristic of the active element. It is approximated by the relation

$$h_i(x_i)=-D_i\tanh(x_i), \tag{4}$$

where D_i is a constant. The parameters of the ring system in Eqs. (1)–(3) are defined by the expressions

$$\alpha_i=C_1/C_i,\quad \beta_i=C_1/L_iG_1^2,\quad \gamma_i=G_i^s/G_1,$$

$$\delta_i=G_i/G_1,\quad \sigma_i=C_1/C_i^s,\quad G_i=1/R_i,\quad G_i^s=1/R_i^s.$$

A numerical analysis of Eqs. (1)–(4) was carried out for three ($n=3$) identical, symmetrically coupled triggers. In this case the subscript i in D_i, α_i, β_i, γ_i, δ_i, and σ_i can be omitted. It was then found that $\alpha=\delta=1$. When the control of the oscillations of the ring system using an external signal was calculated, the latter was included as a term on the right-hand side of Eq. (3.n): the right-hand side of this equation was set equal to $[-\beta(y_3+f(t))]$. Under a harmonic disturbance $f(t)=A_c\cos(\omega_c t)$, where A_c and ω_c are the amplitude and frequency of the external signal.

Figure 2 presents bifurcation diagrams of an autonomous ring system (a) and the analogous nonautonomous ring system under the influence of a controlling harmonic signal (b). They illustrate the distribution of the maximum values of the oscillatory process $x_1(t)$ (they are denoted by $[x_1]$) as a

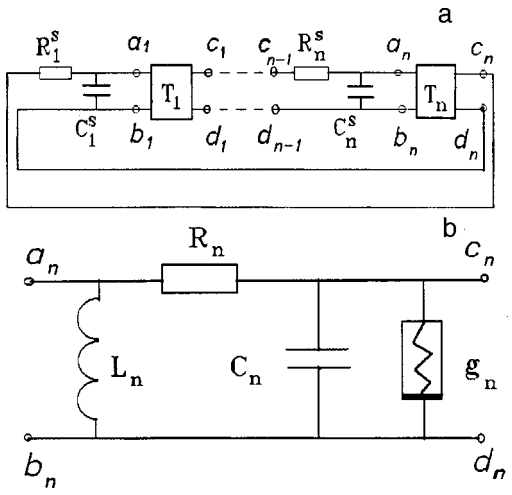

FIG. 1. Schematic representation of a ring system of triggers (a) and diagram of a partial trigger (b).

function of the coupling parameter γ. The diagrams were obtained for increasing γ and the following values of the remaining parameters: $D=3$, $\sigma=0.1$, $\beta=1.6$. The initial conditions were set equal to $x_i(0)=y_i(0)=z_i(0)=0.1$. The amplitude and frequency of the external signal in the case of Fig. 2b are equal to $A_c=0.4$ and $\omega_c=0.4$.

In the absence of coupling ($\gamma=0$) autonomous oscillations are not excited (Fig. 2a). In accordance with the positive initial conditions, the system is in a stable state with the value $[x_1]=4.8$. Increasing the coupling parameter leads to passage of the ring system from the stationary state to an oscillation regime with random passage from one basin of attraction to another. This corresponds to two bands with a random spread of maximum values of $x_1(t)$. An increase in γ is accompanied by greater irregularity in the spread of maximum values of the oscillatory process $x_1(t)$ and a rise

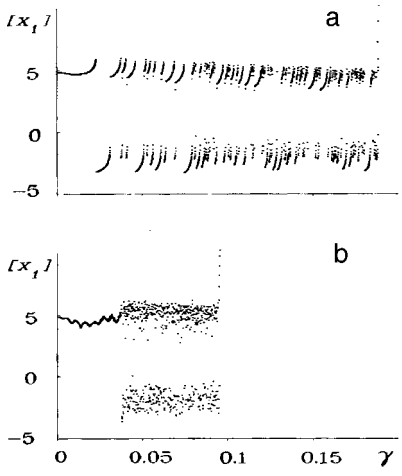

FIG. 2. Bifurcation diagrams for autonomous (a) and nonautonomous (b) operation of a three-trigger ring system.

in the density of the corresponding points. At $\gamma=0.19$ the system goes over to regular motions; the maximum value of $x_1(t)$ reaches $[x_1]=37.8$ at $\gamma=0.2$.

The introduction of a small external harmonic signal leads to alteration of the chaotic behavior of the system, and the transition of the system to regular oscillations occurs at a significantly smaller value of γ (at $\gamma=0.095$). In addition, the amplitude of the stimulated regular oscillations is almost two orders of magnitude greater than the amplitude of the disturbing oscillations, and at $\gamma=0.1$ it equals 32. This attests to a possibility of controlling the oscillations in the interval $\gamma\in[0.1;0.2]$ by an external signal. In fact, chaotic oscillations with random switching between two basins of attraction take place in this range of variation of γ in the autonomous regime, while regular oscillations occur in the presence of a weak external signal. A calculation of the attractors in these two regimes showed that a chaotic double-scroll attractor is observed in one case, while a simple limit cycle is observed in the other case. Control of the chaotic oscillations (in the sense of variation of the switchings between the two basins of attraction) is possible in the interval $\gamma\in[0.04;0.09]$. This is revealed by a comparison of the diagrams in Figs. 2a and 2b.

The investigations described attest to the possibility of employing a three-trigger autostochastic ring system as a generator of controlled chaotic oscillations.

The system considered is also of interest from the standpoint of studying the features of operation of triggers when their speed rises. This is because the capacitance of the integrating circuit in the scheme considered can be manifested as a parasitic capacitance of the inductive element of a partial trigger when the frequency is increased.

This work was carried out with support from the Russian Fund for Fundamental Research (Grant 98-02-16722).

[1] T. Matsumoto, Proc. IEEE **75**, 1033 (1987).
[2] V. A. Kats and S. P. Kuznetsov, Pis'ma Zh. Tekh. Fiz. **13**, 727 (1987) [Sov. Tech. Phys. Lett. **13**, 302 (1987)].
[3] V. Ya. Kislov, Radiotekh. Élektron. **38**, 1783 (1993).
[4] C. W. Wu, T. Yang, and L. O. Chua, Int. J. Bifurcation Chaos **6**, 455 (1996).
[5] É. V. Kal'yanov, Radiotekh. Élektron. **41**, 1490 (1996).
[6] R. V. Belyaev *et al.*, Radiotekh. Élektron. **42**, 188 (1997).
[7] A. S. Khramov, Pis'ma Zh. Tekh. Fiz. **24**(5), 51 (1998) [Tech. Phys. Lett. **24**(3), 189 (1998)].
[8] É. V. Kal'yanov, Izv. Vyssh. Uchebn. Zaved., Prikl. Nelineĭn. Din. **3**(5), 100 (1995).
[9] V. V. Astakhov *et al.*, Radiotekh. Élektron. **42**, 320 (1997).
[10] A. S. Dmitriev, A. I. Panas, and S. O. Starkov, Zarubezhn. Radioélektron., Usp. Sovrem. Radioélektron., No 10, 4 (1997).
[11] V. S. Anishchenko, A. N. Sil'chenko, and I. A. Khavanov, Pis'ma Zh. Tekh. Fiz. **24**(7), 22 (1998) [Tech. Phys. Lett. **24**(4), 257 (1998)].
[12] O. Calvo and J. H. E. Cartwright, in *Proceedings of the 6th International Specialist Workshop, Nonlinear Dynamics of Electron Systems (NDES'98)*, Budapest, Hungary, July 16–18, 1998, pp. 157–160.
[13] E. V. Kal'yanov, Radiotekh. Elektron. **43**, 206 (1998).
[14] W. J. Cunningham, *Introduction to Nonlinear Analysis*, McGraw–Hill, New York (1958), 456 pp.

Translated by P. Shelnitz

Emission of waves by a modulated electron beam

V. V. Dolgopolov

''Khar'kov Physicotechnical Institute'' National Scientific Center, Ukraine
(Submitted November 23, 1998)
Pis'ma Zh. Tekh. Fiz. **25**, 52–55 (May 12, 1999)

It is shown that a semifinite modulated electron beam in a vacuum emits an electromagnetic field. The radiation fields and the radiated power are found. © *1999 American Institute of Physics.* [S1063-7850(99)01005-8]

It is known that a modulated electron beam moving uniformly in a vacuum does not emit waves. We show that this statement does not apply to the portion of the beam adjacent to its source (the accelerator), and we find the radiation fields.

The transition radiation of a modulated electron beam emerging from a semifinite plasma was investigated in Ref. 1. Cases in which the dielectric constant of the plasma is equal to zero or infinity were analyzed in that paper. The transition radiation of modulated beams on the spherical plasma layer surrounding a conducting sphere and in a homogeneous plasma were investigated in Refs. 2 and 3. Let us examine the radiation from a semifinite beam in a vacuum, where there are no inhomogeneous media and the radiation is not of the transition type.

We represent the oscillating part of the density-modulated current of a beam of infinitesimal radius propagating along the z axis from the point $z=0$ in the form

$$J=0 \quad \text{at} \quad z<0,$$

$$J=-eNv\exp[i(kz-\omega t)] \quad \text{at} \quad z>0, \tag{1}$$

where $k>0$, $\omega>0$, $v=\omega/k$ is the beam velocity, N isthe modulation depth of the linear density of the beam, and $-e$ is the charge of an electron. Then, according to Ref. 4, the axial component (the only nonzero component) of the retarding vector potential $\mathbf{A}$ is defined by the expression

$$A_z(r,z)=-\frac{eNv}{c}\int_0^\infty dz'\frac{1}{R'}e^{i[kz'-\omega(t-R'/c)]}, \tag{2}$$

where $R'=[(z'-z)^2+r^2]^{1/2}$, c is the speed of light, and the r,φ,z cylindrical coordinate system is used.

Replacement of the integration variable in Eq. (2) gives

$$A_z=-\frac{eNv}{c}e^{i(kz-\omega t)}\int_\xi^\infty d\zeta\,\frac{e^{i\zeta}}{(\zeta^2+q^2r^2)^{1/2}}, \tag{3}$$

where $\xi=-kz+k_0R$, $k_0=\omega/c$, $q=(k^2-k_0^2)^{1/2}$, and $R=(r^2+z^2)^{1/2}$. When $qr\gg1$ (in the wave zone), the integral on the right-hand side of (3) can be taken approximately. As a result, we obtain

$$A_z\simeq -i\frac{eNv}{c\eta}e^{i(k_0R-\omega t)}, \tag{4}$$

where $\eta=kR-k_0z$. It follows from the relation (4) that at large distances the electromagnetic field represents a wave propagating from the portion of the beam adjacent to the beam source.

The expression for the only nonzero magnetic component of the wave field $H_\varphi=\partial A_z/\partial r$ in the wave zone can be brought into the form

$$H_\varphi\simeq-\frac{eNv^2}{c^2R}\frac{\sin\vartheta}{1-\frac{v}{c}\cos\vartheta}e^{i\theta}, \tag{5}$$

where $\theta=k_0R-\omega t$, $\sin\vartheta=r/R$, $\cos\vartheta=z/R$, and ϑ is the angle between the z axis and the propagation direction of the wave.

For a fixed value of R, the amplitude of the wave propagating at an angle ϑ satisfying the condition

$$\cos\vartheta=\frac{v}{c} \tag{6}$$

will be greatest.

In this case the expression (5) takes the form

$$H_\varphi\simeq-\frac{eNv^2\gamma}{c^2R}e^{i\theta}, \tag{7}$$

where $\gamma=(1-v^2/c^2)^{-1/2}$.

According to (6) and (7), as the relativistic factor γ increases, the radiation is squeezed toward the z axis, where the amplitude of the wave grows proportionally to γ. The components of the electric field of the wave are specified by the expressions

$$E_z=-\frac{\partial\Phi}{\partial z}-\frac{1}{c}\frac{\partial A_z}{\partial t}, \quad E_r=-\frac{\partial\Phi}{\partial r}, \tag{8}$$

where

$$\Phi=\Phi_1+\Phi_2, \quad \Phi_1=\frac{c}{v}A_z. \tag{9}$$

In order to determine the term Φ_2, we must take into account the charge conservation law. For this purpose we place a charge Q satisfying the condition

$$\frac{dQ}{dt}+J_{|_{z=0}}=0, \tag{10}$$

where J is defined by (1), at the point $r=0$, $z=0$. Then the potential Φ_2 created by the charge Q has the form

$$\Phi_2 = i\frac{eNv}{\omega R}e^{i\theta}. \tag{11}$$

The relations (4), (8), (9), and (11) specify the electric field of the waves emitted by the beam.

In the wave zone this field has the form

$$\mathbf{E} = \mathbf{e}_\vartheta H_\varphi, \tag{12}$$

where $\mathbf{e}$ is the unit vector along the direction ϑ, which is perpendicular to the propagation direction of the wave and the vector $\mathbf{H}$. Assuming that the real current J_r is related to the complex current J by the expression

$$J_r = \frac{1}{2}(J + J^*), \tag{13}$$

for the total energy radiated by the beam per unit time we obtain the following expression

$$I = \frac{|J|^2}{2c}\left(\frac{c}{v}\ln\frac{c+v}{c-v} - 2\right), \tag{14}$$

where $|J| = eNv$.

The calculations show that the mean work of the field over the currents per unit time $\int_0^\infty dz\overline{JE}_z$ is positive and equal to $|J|^2/c$. This means that both the electromagnetic energy associated with modulation of the beam and the radiated energy are drawn directly from the beam source.

We thank I. F. Kharchenko for taking an interest in this work and for some useful discussions.

[1] Ph. Parzen, J. Appl. Phys. **32**, 2484 (1961).
[2] V. A. Balakirev, V. A. Buts, and V. I. Kurilko, Zh. Tekh. Fiz. **46**, 477 (1976) [Sov. Phys. Tech. Phys. **21**, 272 (1976)].
[3] V. A. Balakirev and G. L. Sidel'nikov, ''Transition radiation of modulated electron beams in an inhomogeneous plasma'' [in Russian], Preprint, Khar'kov Physicotechnical Institute (1994), p. 104.
[4] L. D. Landau and E. M. Lifshitz, *The Classical Theory of Fields*, 4th ed., Pergamon, New York (1975) [Russ. original, Moscow (1948)].

Translated by P. Shelnitz

Influence of the solid-phase reaction in fullerite–alkali-metal-halide systems on optically detectable vibrational states of C_{60}

A. A. Sukhanov and V. A. Reznikov

St. Petersburg State University
(Submitted December 26 1998)
Pis'ma Zh. Tekh. Fiz. **25**, 56–62 (May 12, 1999)

Spectral data on the solid-phase reaction of powdered C_{60} with potassium halides, which is regarded as the main cause of the modification of the characteristic bands in the IR spectra, are presented. © *1999 American Institute of Physics.* [S1063-7850(99)01105-2]

Vibrational spectroscopy is widely used to investigate fullerenes and their derivatives, as well as for detecting them and determining their concentrations in solid samples. The spectra of C_{60} and C_{70}, which have been accessible in macroscopic quantities since 1990, have been studied most thoroughly. Among the various sample preparation methods, mechanical dispersion of powdered fullerite particles in a volume of powdered KBr has become dominant.

A comparative analysis of the vibrational absorption spectra obtained by various investigators reveals a more than twofold variation in the relative intensity of the characteristic bands of C_{60} and their position in ranges up to 5 cm^{-1}, as well as the appearance of bands which correspond to modes that are active in the Raman or inelastic neutron scattering spectra.[1–3] The observation of broad bands at 400–600, 900–1200, and 1400–1450 cm^{-1} and differences in the background level, which are most probably attributable to variation of the impurity composition of the supporting matrix, should also be noted.

The variation of the spectral features noted cannot be attributed to possible errors in the measurement of the optical density alone[4] and, according to Kratchmer's hypothesis,[5] can be associated with a reaction of the C_{60} molecules with the matrix. The problem has not previously been examined in this context because of the relatively high chemical stability of the solid-phase supporting matrix and the weak dependence of the spectral features on the degree of dispersion of the fullerene particles.[5–7]

The chemical stability, polarizability, and distribution of the electron density of the C_{60} molecule allow us to regard it as a unique adatom,[8,9] while the high electron affinity $E_a = 2.65$ eV allows drawing analogies with ions of heavy *d* metals.

It may be assumed that the adsorption of C_{60} on the surface of an ionic crystal can lead to polarization of the π-electron density and an accompanying displacement of charges in the near-surface region of the potassium halide (KHal).[10] The polarization model presumes a dependence of the results of the C_{60}–KHal reaction on the halide composition of the matrix, as well as a high degree of dispersion of fullerite.

To verify the dependence of the IR absorption spectra on the properties of the supporting matrix, we performed a comparative analysis of the IR spectra of C_{60} dispersed in KCl, KBr, and KI matrices. A fullerite powder with a concentration of C_{60} no less than 99.5% and powdered KCl, KBr, and high-purity KI were used. Mixtures of the KHal and fullerite powders were prepared in a vibratory ball mill. The possible reaction of the mixture components with the internal surface of the mixer was monitored by x-ray fluorescence analysis by inducing the Γe band and measuring the relative concentrations of K and Hal in the composite. Before mixing, the powders were dehydrated at 250 °C. The IR absorption spectra of the KHal–C_{60} composites and the corresponding supporting matrices were recorded on a Specord M-80 spectrophotometer.

The common features of the spectra of these mixtures (Fig. 1) include variation of the background level, which depends on the halide composition of the matrix, as well as the formation of broad bands in the spectral ranges 400–600, 900–1200, and 1350–1470 cm^{-1}. The intensity of the broad band at 900–1200 cm^{-1} decreases from KCl and KI, and its maximum undergoes a 25–30-cm^{-1} bathochromic shift.

Some samples of C_{60}–KBr and C_{60}–KI mixtures exhibit a periodic structure of equally spaced bands of identical intensity at 700–900 cm^{-1}. The dependence of the position of the bands in the periodic structure on the halide composition of the supporting matrix and the sample preparation and storage conditions, particularly on the thickness of the pellets, points out the interference nature of most of the bands in the periodic structure. The appearance of an interference pattern in the spectra of samples of heterogeneous composition is an indication of homogenization of the structure of the mixture in comparison to the structure of the original matrix, which is confirmed by a 10-fold decrease in the diameters of the ground particles of the C_{60}–KHal mixture in comparison to KHal particles ground under similar conditions.

Thus, the variation of the background level and the formation of broad bands and periodic structures at 700–900 cm^{-1} are spectral features which depend on the halide composition of the matrix and cannot appear as a result of purely mechanical contact between the particles of the semiconductor and the dielectric and which, taken together, indicate the occurrence of a reaction between the fullerite and KHal particles within the composite. The same conclu-

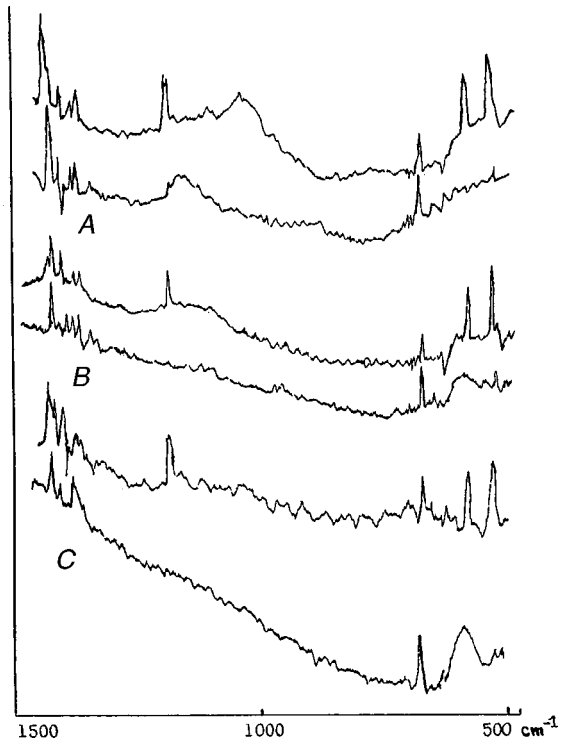

FIG. 1. IR spectra of C_{60} in KCl (*A*), KBr (*B*), and KI (*C*) matrices (the spectrum of the corresponding matrices are shown below each of the spectra).

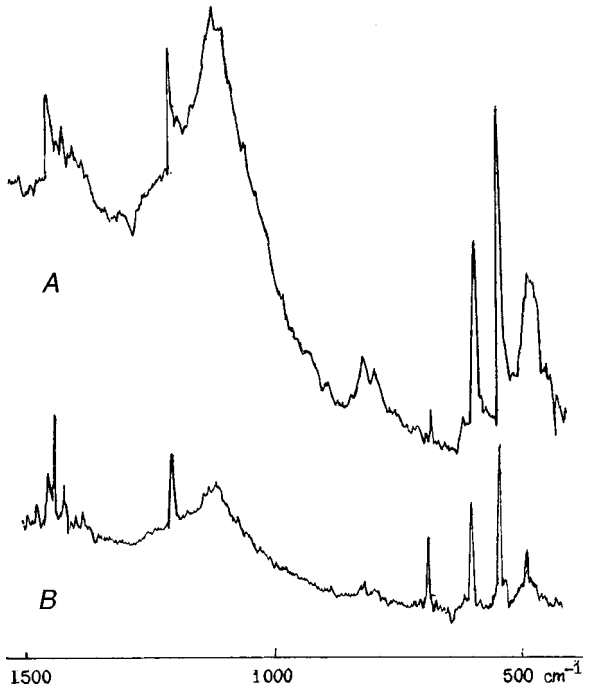

FIG. 2. IR spectra of the amorphized phase obtained from a C_{60}–KCl composite measured in a KCl matrix: *A* — high concentration of the amorphized phase; *B* — low concentration of the amorphized phase.

sion follows from the water solubility of all the C_{60}–KHal composites prepared.

Evaporative concentrating of aqueous solutions of the composites results in the precipitation of KHal crystals and a colored amorphized phase (AP) of fractal geometry. The volume ratios of KHal and the amorphized phase in the composition of the dry residues after evaporation of the water, as well as the fact that the mass of the dry amorphized phase is 1.5–2.0 times greater than the mass of C_{60} in the composite, rule out any connection between it and impurities in the KHal or undetected impurities in the distillate. The solubility of the amorphized phase in weakly polar solvents like benzene points out the possible presence of C_{60} molecules in its composition.

To identify C_{60} in the composition of the amorphized phase, we measured the IR spectra of the amorphized phase in matrices of the respective KHal. Figures 2 and 3 present the IR spectra of the amorphized phase precipitated from solutions of C_{60}–KCl (Fig. 2) and C_{60}–KBr (Fig. 3) composites. These spectra were measured in samples with a high (spectrum *A*) and a low (spectrum *B*) concentration of the amorphized phase relative to the matrix of the respective KHal. The presence of characteristic bands in the spectra in Fig. 2 (spectrum *B*) and Fig. 3 (spectrum *B*) indicates that C_{60} appears in the composition of the amorphized phase.

Diluting and mixing the amorphized phase in the material of the KHal matrix leads to a decrease in the intensity of the broad structured band at 900–1200 cm^{-1}. The spectrum of the highly concentrated amorphized phase recovered from the C_{60}–KBr composite (Fig. 2, spectrum *A*) does not contain characteristic bands of C_{60}, while the spectrum of the same amorphized phase diluted to a high degree is the classical spectrum for C_{60}, with the exception of a series of weak bands, some of which (the bands at 774 and 1250 cm^{-1}) are characteristic of the Raman spectra of C_{60}.[1] In particular, the bands at 713, 741, and 776 cm^{-1}, which have also been discovered in the inelastic neutron scattering spectra,[1–3] can be regarded as split-off bands of the band at 774–776 cm^{-1} in the low-frequency region, in agreement with the baric shift of the frequencies corresponding to the Hg(*3*) and Hg(*4*) vibrational modes.[11]

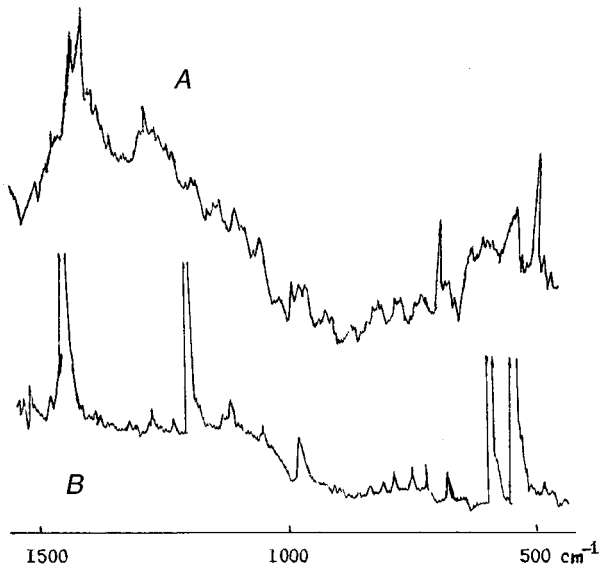

FIG. 3. IR spectra of the amorphized phase obtained from a C_{60}–KBr composite measured in a KBr matrix: *A* — high concentration of the amorphized phase; *B* — low concentration of the amorphized phase.

This finding means that at least some of the C_{60} molecules are found in a shell of interacting molecular centers of the matrix composition. The relative intensities of the characteristic bands and the broad bands in the range $900-1200\ cm^{-1}$ in the spectra of the $C_{60}-KCl$ (Fig. 1, spectrum *A*) and AP–KCl (Fig. 2, spectrum *B*) composites are roughly identical for the low concentration of the amorphized phase, while in the corresponding spectra of the $C_{60}-KBr$ (Fig. 1, spectrum *B*) and AP–KBr (Fig. 3, spectrum *B*) composites the relative intensities of these bands differ significantly, confirming the connection between the modification of the spectral features and the chemical composition of the supporting matrix.

A broad band was observed in the range $900-1200\ cm^{-1}$ in the IR spectra of polymerized C_{60} molecules in Refs. 12 and 13. The decrease in the intensity of this band in the spectra considered here is caused by dispersal of the amorphized phase, and, therefore, the self-similarity element of the amorphized phase as a fractal aggregate is a fullerene-containing molecular complex. In this context the decrease in the intensities of the broad bands in the spectra of the $C_{60}-KHal$ composites upon passage from KCl to KI corresponds to the decrease in the mobility of the complex molecular centers on the matrix surface and correlates with the increase in electron affinity from KCl (0.1 eV) and KB (0.7 eV) to K (1.0 eV).[14]

We thank N. A. Charykov for supplying the C_{60} samples, as well as S. V. Karpov, N. I. Kochnev, A. N. Krasovskiĭ, and A. Yu. Serov for participating in the discussion of the results.

[1] A. V. Eletskiĭ and B. M. Smirnov, Usp. Fiz. Nauk **165**, 977 (1995) [Phys. Usp. **38**, 935 (1995)].
[2] K. Prassides, T. John, S. Dennis, J. P. Hare *et al.*, Chem. Phys. Lett. **187**, 455 (1991).
[3] C. Coulombaux, H. Jobic, P. Bernier *et al.*, J. Phys. Chem. **96**, 22 (1992).
[4] A. L. Smith, *Applied Infrared Spectroscopy: Fundamentals, Techniques, and Analytical Problem Solving*, Wiley, New York (1979) [Russ. transl., Mir, Moscow (1982), p. 327].
[5] Kratchmer *et al.*, Chem. Phys. Lett. **170**, 167 (1990); Nature (London) **347**, 354 (1990).
[6] P. S. Bethune *et al.*, Chem. Phys. Lett., No. 1–2, 181 (1991).
[7] G. N. Churilov, O. A. Bayukov, É. A. Petrakovskaya *et al.* Zh. Tekh. Fiz. **67**(9), 142 (1997) [Tech. Phys. **42**, 1111 (1997)].
[8] S. V. Kozyrev and V. V. Rotkin, Fiz. Tekh. Poluprovodn. **27**, 1409 (1993) [Semiconductors **27**, 777 (1993)].
[9] V. V. Afrosimov, A. A. Basalaev, and M. N. Panov, Zh. Tekh. Fiz. **66**(5), 10 (1996) [Tech. Phys. **41**, 412 (1996)].
[10] B. F. Ormont, *Introduction to the Physical Chemistry and Crystal Chemistry of Semiconductors* [in Russian], Vysshaya Shkola, Moscow (1968), p. 487.
[11] K. P. Meletov, G. Kourouklis *et al.*, Zh. Éksp. Teor. Fiz. **108**, 1456 (1995) [JETP **81**, 798 (1995)].
[12] Ya-Ping Sun, Bin Ma, and E. Christopher, J. Am. Chem. Soc. **117**, 12 705 (1995).
[13] Shuichi Osawa, Jun Onoe, and Kazuo Takeuchi, Fullerene Sci. Technol. **6**(2), 301 (1998).
[14] É. D. Aluker, D. Yu. Lusis, and S. A. Cherkasov, *Electron Excitations and X-Ray Luminescence of Alkali-Metal Halide Crystals* [in Russian], Zinatne, Riga (1979), p. 251.

Translated by P. Shelnitz

Nonstationary photocurrent in a $Bi_{12}SiO_{20}$ crystal grown in an argon atmosphere

M. A. Bryushinin and I. A. Sokolov

Institute of Mechanical-Engineering Problems, Russian Academy of Sciences, St. Petersburg
(Submitted December 25, 1998)
Pis'ma Zh. Tekh. Fiz. **25**, 63–69 (May 12, 1999)

A detailed investigation of the nonstationary photocurrent in crystals with a sillenite structure grown in an oxygen-free (argon) atmosphere is performed. Basic parameters of the photoinduced charge carriers in the crystals investigated, such as the mean carrier lifetime and mobility, the mean photoconductivity, the carrier diffusion length, and the Debye screening length, are determined. © *1999 American Institute of Physics.* [S1063-7850(99)01205-7]

Measuring the nonstationary photo-emf[1] is an effective method for determining the parameters of photoinduced charge carriers in semiconductors. This method can be used to evaluate, for example, the mean photoconductivity σ_0 of a crystal, the carrier diffusion length L_D, the mean carrier lifetime τ, the mobility μ, and the concentration of impurity centers N_A on which the charge distribution is formed.[1–3] The mechanism for the appearance of a sign-alternating current in a photoconductive crystal illuminated by a oscillating interference pattern (Fig. 1) has already been described in detail many times:[1] a photocurrent appears in a short-circuited sample as a consequence of the periodic relative displacement of the distributions of the photoconductivity and the electric field of charges captured in deep traps. To obtain an oscillating interference pattern, one of the two coherent light beams is phase-modulated with a frequency ω.

This paper describes an investigation of the nonstationary photocurrent excited in a photorefractive crystal of bismuth silicosillenite $Bi_{12}SiO_{20}$ (BSO) grown in an argon atmosphere. An investigation of such crystals has already been reported in Ref. 4; however, the experiments were carried out in a fairly narrow range of values of the spatial frequency K of the interference pattern and the mean intensity I_0 of the light impinging on the crystal. A high photosensitivity of $Bi_{12}SiO_{20}$ crystals was discovered in that study, revealing a prospect for employing them as a material for constructing adaptive interferometric sensors.[3] Such an application of the nonstationary photo-emf, as well as prediction of the properties of devices and systems based on photorefractive crystals, require exact determination of the photoelectric parameters of the materials used. Therefore, the purpose of the present work was to thoroughly study the nonstationary photocurrent in a photoreactive $Bi_{12}SiO_{20}$ crystal and to determine the basic parameters of the photoinduced charge carriers over a broad range of variation of the parameters of the interference pattern K and I_0.

The photorefractive $Bi_{12}SiO_{20}$ crystal grown in an argon atmosphere measured $3\times5\times5$ mm. The front and rear surfaces of the crystal (3×5 mm) were polished, and electrodes were deposited on the two lateral surfaces (5×5 mm) using a silver paste. An LGN-215 helium-neon laser ($\lambda=0.633$ μm, $P=30$ mW) served as a source of coherentlight. An ML-102A electro-optic modulator was employed for phase modulation of one of the beams. The voltage on the load resistance ($R=33$ kΩ) was measured using a Unipan-233-7 selective amplifier and an SK 4-56 spectrum analyzer. The extinction coefficient of the crystal at the wavelength $\lambda=0.633$ μm was equal to $\alpha=0.86$ cm^{-1}.

Plots of the experimental dependence of the amplitude of the first harmonic of the nonstationary photocurrent on phase-modulation frequency are presented in Fig. 2. Altogether 34 frequency dependences of the photocurrent were recorded for spatial frequencies equal to 57, 130, 270, 570, 1100, and 2500 mm and the light intensities $I_0=5.9$, 12, 23, 64, 130, and 280 μW/mm^2.

The unusually large value of the photocurrent for BSO crystals grown under ordinary conditions should first be noted. Light intensities 2–3 orders of magnitude larger are ordinarily needed to obtain a similar signal amplitude. Thus, the photoconductivity of the crystal that we investigated ($\sigma_0=10^{-6}-10^{-5}$ Ω^{-1}m^{-1}) was 2–3 ordersof magnitude greater than the photoconductivity of ordinary sillenites grown in an oxygen atmosphere.

As was shown in Ref. 5, the amplitude of the first harmonic of the nonstationary photocurrent (for $\tau_I=\tau$) at the maximum of the frequency characteristic is determined mainly by the mean photoconductivity of the crystal σ_0:

$$J^{\omega}=\frac{0.5Sm^2\Delta E_D\sigma_0}{2+(KL_D')^2}\times\frac{-i\omega\tau_M}{2+(KL_D')^2-\omega^2\tau\tau_M+i\omega\{\tau+\tau_M[2+(KL_D)^2]\}}. \quad (1)$$

Here S is the area of the electrodes, m is the contrast of the interference pattern ($m=0.31$), Δ is the phase-modulation amplitude ($\Delta=0.26$), $E_D=Kk_BT/e$ is the diffusion field, $\sigma_0=e\mu n_0$ is the mean photoconductivity, $L_D=(\mu\tau k_BT/e)^{0.5}$ is the electron diffusion length, $L_D'=[(\varepsilon\varepsilon_0k_BT)/(e^2N_{A0})]^{0.5}$ is the Debye screeninglength, $\tau=(\gamma N_{A0})^{-1}$ is the lifetime, τ_I is the lifetimeof an ionized donor center, $\tau_M=\varepsilon\varepsilon_0/\sigma_0$ is the Maxwellian relaxation time, k_B is the Boltzmann constant, ε_0 is the permittivity of

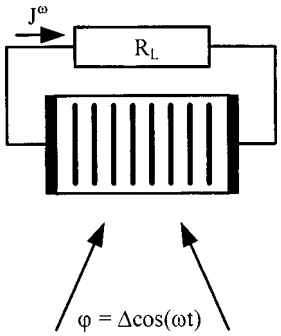

FIG. 1. Scheme for measuring the nonstationary photo-emf in photoconductive media.

free space, e is the charge of an electron, T is the temperature, μ is the electron mobility, γ is the electron capture coefficient, ε isthe dielectric constant of the material ($\varepsilon = 56$), N_{A0} is the concentration of ionized donors, and n_0 is the conduction-band electron density.

We also note the nonlinear character of the dependence of the amplitude of the nonstationary photo-emf on light intensity (for small values of K). Such behavior of the signal can be attributed to the quadratic law governing the recombination of photoexcited charge carriers in the crystal investigated. As was shown in Ref. 5, such effects can be observed in cases where the concentration of photoexcited electrons n_0 exceeds the concentration of deep centers in the absence of illumination $N_A(I_0=0)$. Then the lifetime of an electron is roughly equal to the lifetime of an ionized donor $\tau \approx \tau_I = (\gamma n_0)^{-1}$ and is significantly dependenton light intensity.

We performed additional experiments to measure the photoconduction relaxation time using amplitude-modulated light.[6] In these experiments an external field was applied to a crystal uniformly illuminated by amplitude-modulated light. A nonlinear dependence of the photoconduction relaxation time on light intensity was observed up to intensities of the order of 0.1 μW/nm^2 (Fig. 3).

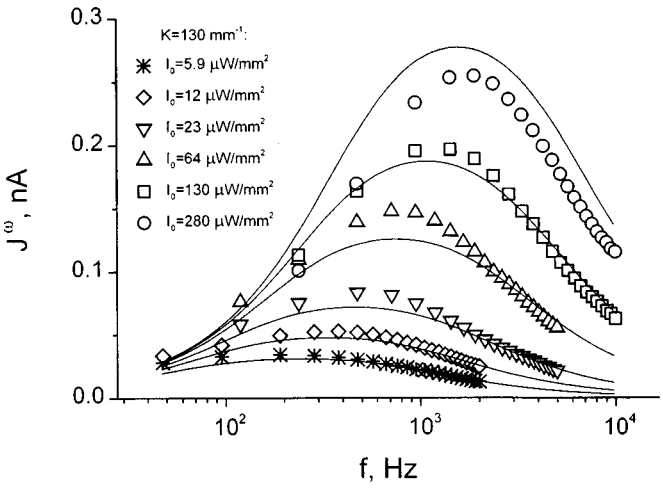

FIG. 2. Dependence of the amplitude of the nonstationary photocurrent on the phase-modulation frequency ω (BSO, $\lambda = 0.633$ μm, $K = 130$ mm).

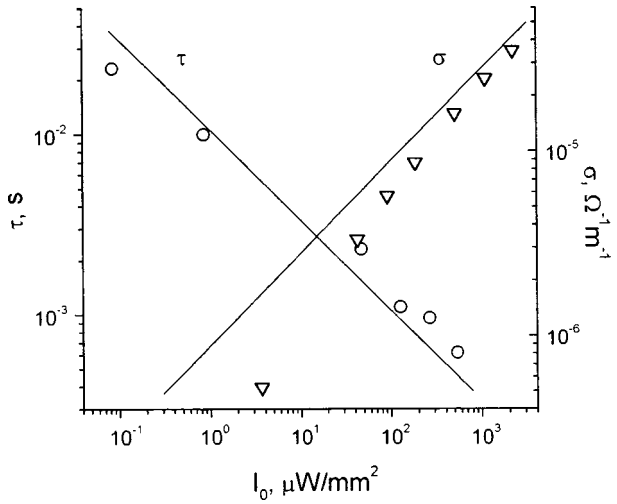

FIG. 3. Results of measurements of the photoconductivity and the lifetime by the standard method.[6] The solid lines are theoretical plots of $\sigma(I_0)$ and $\tau(I_0)$ calculated for the values of $S_D N_D$, γ, and μ obtained.

In the case of a quadratic law governing carrier trapping, the expressions for the stationary concentrations n_0 and N_{A0} can be written in the following form:

$$n_0 = N_{A0} = \sqrt{\frac{g_0}{\gamma}} = \sqrt{\frac{S_D N_D I_0}{\gamma}}. \tag{2}$$

Here $g_0 = S_D N_D I_0$ is the photoelectron generation rate, S_D is the generation cross section, and N_D is the concentration of donor centers from which charge carriers are generated.

The frequency dependence of the photocurrent $J^{\omega}(\omega)$ was approximated using formula (1). The quantities $S_D N_D$, γ, and μ were taken as parameters.

The following values were found for them: $S_D N_D = 2.1 \times 10^{18}$ J^{-1} cm^{-1}, $\gamma = 4.2 \times 10^{-11}$ cm^3 s^{-1}, and $\mu = 2.5 \times 10^{-2}$cm^{2}V^{-1}s^{-1}. The calculated value of $S_D N_D$ and the experimentally measured extinction coefficient α could be used to estimate the photoconduction quantum efficiency $\beta = 0.78$.

Beside the nonlinear dependence of the lifetime on light intensity, we should mention the relation between τ_M and τ, which is unusual for sillenites grown under ordinary conditions: $\tau \approx 20\tau_M$. Such a relation between these two parameters is confirmed both by calculations of τ_M and τ using the values of $S_D N_D$, γ, and μ found fromthe frequency dependences and by experiments devised to measure the lifetime. The value of τ for $I_0 = 540$ μW/mm^2 was equal to 6.2×10^{-4} s, and the mean photoconductivity σ_0 of the crystal for $I_0 = 510$ μW/mm^2 is equal to 1.6×10^{-5} Ω^{-1} m^{-1} (Fig. 3).

In the case of a quadratic type of carrier trapping, the ratio $\gamma/\mu = e/(\sigma_0 \tau) \approx 1.6 \times 10^{-9}$ V·cm can be estimated if τ and σ_0 are known. The value of this ratio for the parameters found from the frequency characteristics of the photo-emf equals $\gamma/\mu \approx 1.7 \times 10^{-9}$ V·cm. The relationship $\tau \gg \tau_M$ implies that the first cutoff frequency ω_0 (see Ref. 5) on the amplitude-frequency characteristics of the photo-emf recorded for an ''argon'' crystal at small values of K corre-

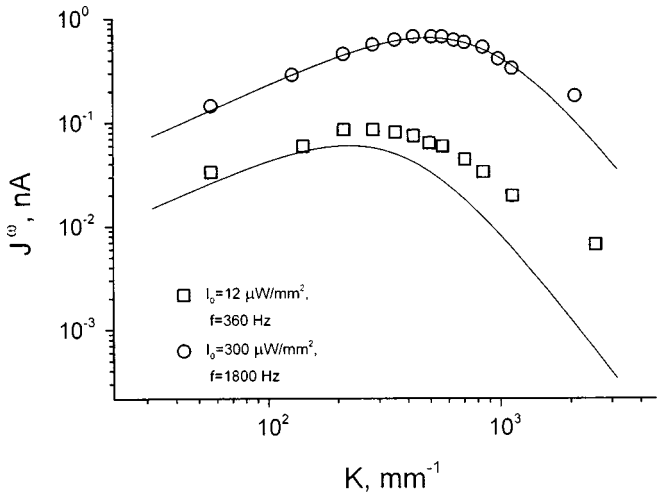

FIG. 4. Experimental and theoretical plots of the nonstationary photocurrent as function of the spatial frequency K of the interference pattern recorded for two values of the light intensity I_0 on the crystal.

sponds to $(\tau/2)^{-1}$ and that the second cutoff frequency ω_0' corresponds to the reciprocal of the Maxwellian relaxation time τ_M^{-1}.

Plots of the dependence of the photocurrent on the spatial frequency of the interference pattern are shown in Fig. 4. As is seen from the experimental curves presented, the maximum on the $J^\omega(K)$ curve shifts toward higher spatial frequencies when the light intensity is increased. A similar phenomenon was previously observed in sillenites, but for the blue-green region of the spectrum. The reason for such behavior of the photocurrent is the dependence of the diffusion and Debye lengths on light intensity which exists in the case of a quadratic trapping law. Figure 4 also shows theoretical plots of $J^\omega(K)$ calculated in accordance with the values of $S_D N_D$, γ, and μ obtained. The values of L_D and L_D' calculated for the intensities at which the experimental plots were recorded were, respectively, $L_D=14$ μm, $L_D'=3.2$ μm for $I_0=12$ μW/mm^2 and $L_D=6.1$ μm, $L_D'=1.4$ μm for $I_0=300$ μW/mm^2.

The values of γ and μ obtained are effective and are roughly two orders of magnitude smaller than the true values. Just these parameters determine the characteristics of instruments and devices based on photorefractive crystals. The difference between the effective and true parameters is due to the presence of a complex structure of shallow trapping centers in sillenites. The effective value of the mobility μ is consistent with the earlier investigations of sillenites [$\mu=2.9\times10^{-2}$ cm^2/V·s (Ref. 7)]. The role of the attachment levels is even greater in crystals grown in an argon atmosphere: the growth of a crystal with an oxygen deficiency leads to the appearance of a considerable number of shallow donor centers, which are responsible for populating the deep traps and corresponding increases in the photoconductivity and carrier lifetime.[8] The high photosensitivity of sillenites grown in an oxygen-free atmosphere suggests that these materials will find application in the construction of optical sensors that function in the infrared and red spectral ranges.

[1] M. P. Petrov, I. A. Sokolov, S. I. Stepanov, and G. S. Trofimov, J. Appl. Phys. **68**, 2216 (1990).
[2] G. S. Trofimov and S. I. Stepanov, Fiz. Tverd. Tela (Leningrad) **28**, 2785 (1986) [Sov. Phys. Solid State **28**, 1559 (1986)].
[3] M. P. Petrov, S. I. Stepanov, and A. V. Khomenko, in *Photorefractive Crystals in Coherent Optical Systems (Springer Series in Optical Sciences, Vol. 59)*, T. Tamir (Ed.), Springer-Verlag, Berlin (1991).
[4] Yu. B. Afanas'ev, V. V. Kulikov, E. V. Mokrushina, A. A. Petrov, and I. A. Sokolov, Pis'ma Zh. Tekh. Fiz. **23**(17), 28 (1997) [Tech. Phys. Lett. **23**(9), 668 (1997)].
[5] I. A. Sokolov and S. I. Stepanov, Optik (Stuttgart) **93**(4), 175 (1993).
[6] S. M. Ryvkin, *Photoelectric Effects in Semiconductors*, Consultants Bureau, New York (1964) [Russ. original, Fizmatgiz, Moscow (1963), 496 pp.].
[7] S. L. Hou, R. B. Lauer, and R. E. Aldrich, J. Appl. Phys. **44**, 2652 (1973).
[8] V. K. Malinovskiĭ, O. A. Gudaev, V. A. Gusev, and S. I. Demenko, *Photoinduced Phenomena in Sillenites* [in Russian], Nauka, Novosibirsk (1990), 160 pp.

Translated by P. Shelnitz

Phenomenological model of the anomalous behavior of the avalanche noise factor in metal-insulator-semiconductor structures

N. E. Kurochkin and V. A. Kholodnov

Orion Scientific-Industrial Association State Unitary Enterprise, Moscow
(Submitted September 25, 1998)
Pis'ma Zh. Tekh. Fiz. **25**, 70–76 (May 12, 1999)

A model which explains the experimentally observed drop in the avalanche noise factor F with increasing values of the stationary mean carrier multiplication factor $M=\langle\tilde{M}\rangle$ in metal-insulator-semiconductor (MIS) structures is proposed. The basis of the model is the retention of carriers at the interface due to trapping either in a potential well or on surface states. The results of the calculation correspond numerically to the experimental data. © *1999 American Institute of Physics.* [S1063-7850(99)01305-1]

It was discovered experimentally in MIS structures based on *p*-type Si in Refs. 1–3 that the avalanche noise factor F ceases to increase (and even drops) with increasing values of the stationary mean carrier multiplication factor M at values above $M=10^2-10^3$. Such behavior of F is paradoxical: because of the random character of an impact-ionization act, F should always increase with increasing M.[4–7] In Refs. 1–3 the avalanche was initiated by electrons flowing into the multiplication region. Therefore, according to the classical treatment in Ref. 4, when $M\gg 1$, it would be expected that $F\cong kM$ and increases with increasing M, where $k(E)\equiv\beta/\alpha$ is a monotonically increasing function of the electric field intensity $E\equiv\langle\tilde{E}\rangle$,[5–11] and α and β are the electron and hole impact-ionization coefficients. According to the data from the experiments in Refs. 1–3, $F\ll kM$ at fairly large values of M. It is shown below that this is actually the case.

Our model of the anomalous behavior of $F(M)$ is not associated with fluctuations of the potential along the interface.[1–3] It is based on the trapping of electrons for a certain time either by a potential well near the interface [such wells exist in SiO_2/Si and TiO_2/Si (Refs. 1 and 2); see Fig. 1a] or by surface states.[12] To find the surface density of trapped carriers $\tilde{N}_s$, we use the continuity equation

$$q\frac{d}{dt}\tilde{N}_s=\tilde{I}_{\text{in}}-\tilde{I}_{\text{out}}, \tag{1}$$

where $\tilde{I}_{\text{in}}=\tilde{M}\tilde{I}_1$ and $I_{\text{out}}=q\tilde{N}_s/\tau$ are the current densities of the electrons flowing toward the interface from the multiplication region in the narrow-gap (N) layer and the electrons flowing into the wide-gap (W) layer, respectively (Fig. 1a), $\tilde{I}_1$ is the current density for $M=1$, τ is the characteristic release time of the trapped carriers, and q is the charge of an electron.

The voltage on the structure $V=\tilde{V}_W+\tilde{V}_N$ is the sum of the voltages on the W- and N-layers $\tilde{V}_W$ and $\tilde{V}_N$ (Fig. 1b). Assuming that the N-layer is uniformly doped[1–3] and that the value of $\tilde{E}$ in the W-layer at large values of M is determined mainly by the charge $q\tilde{N}_s$ (Refs. 10, 12, and 13), under short-circuit conditions (Fig. 1b) we can write

$$V_N\frac{\delta E_N}{E_N}=-V_W\frac{\delta N_s}{N_s}, \tag{2}$$

where δE_N and δN_s are small (fluctuational) deviations from the stationary mean values $\langle\tilde{N}_s\rangle\equiv N_s$ and $\langle\tilde{E}_N\rangle\equiv E_N$ ($\tilde{E}_N$ is the field in the N-layer near the interface), $V_N=\langle\tilde{V}_N\rangle$, and $V_W=\langle\tilde{V}_W\rangle$. As can be seen from (2), a positive fluctuation $\delta N_s>0$ decreases [due to screening by the charge $-q\cdot\delta N_s<0$ (Refs. 13 and 22)] the field in the N-layer ($\delta E_N<0$) and consequently lowers the intensity of the avalanche process.

Since α and β drop sharply as E decreases and the gap width increases,[5–11,14] and $E(x)$ falls off across the width of the N layer, we assume that carrier multiplication occurs only in a narrow part of the space-charge layer (SCL) within the N-layer near the interface (the δ-function approximation[15]). In this approximation, using Read's relation[16]

$$\tilde{I}(t)=\frac{1}{\mathcal{L}}\int_{\text{SCL}}[\tilde{I}_n(t,x)+\tilde{I}_p(t,x)]\,dx, \tag{3}$$

where $\tilde{I}_n$ and $\tilde{I}_p$ are the electron and hole current densities in the space-charge layer, $\mathcal{L}$ is its thickness, and neglecting the small flux of carriers flowing from the W-layer into the N-layer, for $M\gg 1$ we can obtain the following expression for the current density in the external circuit:

$$\tilde{I}(t)=\frac{1}{T}\left(\int_{t-T_N}^{t}\tilde{I}_{\text{in}}(t')\,dt'+\int_{t-T_W}^{t}I_{\text{out}}(t')\,dt'\right), \tag{4}$$

where $T=T_N+T_W$, and T_N and T_W are the transit time of holes and electrons across the space-charge layer and the W-layer, respectively. The relations (2) and (4) allow us to write $\tilde{I}(t)$ in the form of a linear functional of $\delta N_s(t')$ averaged over the time T. This means that the smaller is the relaxation time τ_r of the fluctuational deviations compared to T, the smaller are the current fluctuations in the external circuit.

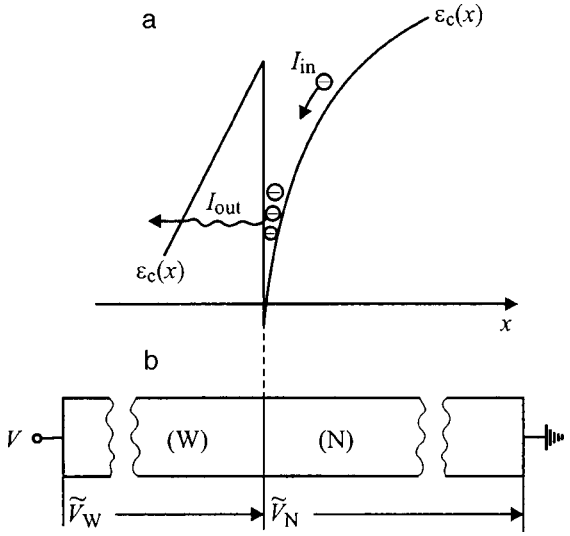

FIG. 1. Energy diagram of $[\mathcal{E}_c(x)]$ of the bottom of the conduction band of a structure near the interface (a) and electrical diagram (b).

At large values of M the time τ_r decreases with increasing M. In fact, after representing the function $M(V)$ in Miller's form[17–19]

$$M=\frac{1}{1-(V_N/V_{NB})s_n(V_N)}, \tag{5}$$

from the linearized equation (1) and the relation (2) we can obtain the following expressions for $M\gg 1$:

$$\frac{d}{dt}\delta N_s=-\frac{\delta N_s}{\tau_r}, \quad \tau_r=\frac{\tau}{1+(V/V_{NB}-1)s_{nB}M}, \tag{6}$$

where V_{NB} is the breakdown voltage of the N-layer,[5–10,18,19] $s_n(V_N)$ is the exponent for the flow of electrons into the multiplication region, and s_{nB} is the value of s_n for $V_N \to V_{NB}$, which was calculated numerically in Ref. 20. Analytical expressions for the exponent (also for the flow of holes into the multiplication region), which are quantitatively consistent with the results in Ref. 20 and the experimental data in Refs. 17 and 21–25, were derived in Refs. 18 and 19. The decrease in τ_r with increasing M also causes an anomalous dependence of F on M at large values of M.

When there is no correlation between the avalanche noise and the noise of the electrons flowing into the W-layer, the fluctuation spectrum of $\tilde{N}_s$ is the sum of the corresponding spectral noises[4–7] multiplied by the dynamic function of the system.[5,26] Therefore, using Eq. (6), we find that

$$\langle(\delta N_s)^2\rangle(\omega)=(2qI_0kM^3+2qI_{out})\frac{\tau_r^2}{(1+\omega^2\tau_r^2)q^2}$$

$$=\frac{2I_0M^2}{q}\cdot(kM+M^{-1})\frac{\tau_r^2}{1+\omega^2\tau_r^2}. \tag{7}$$

The dispersion of processes of the type $\tilde{i}(t)=(q/T)\cdot\int_{t-T}^{t}[\tilde{n}(t')/\tau_r]\,dt'$ can be described by the familiar McDonald formula[26]

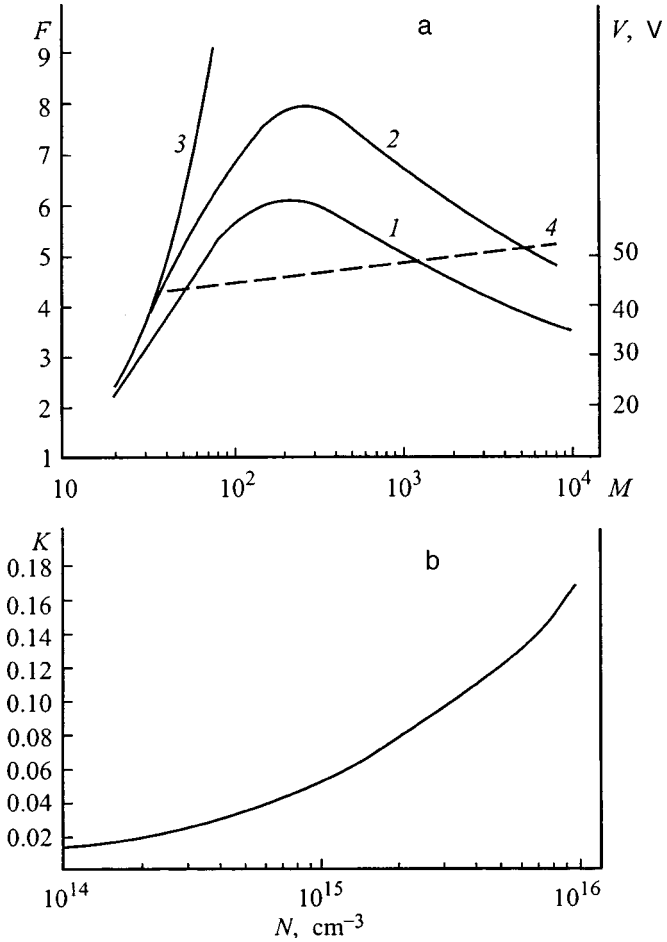

FIG. 2. a — Theoretical (*1*) and experimental (*2*, Refs. 3 and 27) dependences of the avalanche noise factor F on the carrier multiplication factor M for SiC/Si heterostructures. The experimental dependence of M on the voltage V applied to the structure that was used in the calculation of $F_{th}(M)$ (*3*, Refs. 3 and 27) and the $F(M)$ curve predicted by the generally known McIntire relation[4–7] (*4*) are also shown. b— Dependence of the ratio k_B between the hole and electron impact-ionization coefficients in silicon near an interface on the concentration of shallow impurity acceptors N_A for $V_N \to V_{NB}$ used in the calculation of $F_{th}(M)$.

$$\langle(\tilde{i}-\langle\tilde{i}\rangle)^2\rangle=\frac{1}{\pi T}\cdot\left(\frac{q}{\tau_r}\right)^2 \times\int_0^{\infty}\frac{\langle(\delta n)^2\rangle(\omega)}{\omega^2}\cdot[1-\cos(\omega T)]\,d\omega. \tag{8}$$

If $T_N \ll T_W$ (Refs. 3 and 27), the first term in (4) can be neglected. Then, for

$$M\gg M_a\equiv\frac{V_{NB}}{S_{nB}V_W}, \tag{9}$$

if we take into account that, as follows from Refs. 18 and 19,

$$S_{nB}=\frac{4k_B\ln k_B}{k_B-1} \tag{10}$$

under the conditions considered here, we can obtain

$$F \equiv \frac{\langle (\delta I)^2 \rangle}{\langle \tilde{I} \rangle^2} \cong \frac{k_B}{s_{nB}} \frac{V_{NB}}{V_W} = \frac{k_B^{-1}}{4 \ln k_B} \frac{V_{NB}}{V - V_{NB}}, \quad (11)$$

where k_B is the value of k near the interface for $V_N \rightarrow V_{NB}$.

It can be seen from formula (11) that F falls off with increasing V, i.e., with increasing M.

The experimental $M(V)$ and $F(M)$ curves presented in Refs. 3 and 27 for SiC/Si heterostructures (Fig. 2a) permit a numerical comparison of the conclusions of the theory proposed above with experimental data. The calculation was performed using the dependence of k_B on the concentration of shallow impurity acceptors N_A in Si shown in Fig. 2b.[7] It can be seen from Fig. 2a that the results of our calculation will be in satisfactory quantitative agreement with the experimental data if we set $N_A \cong 5 \times 10^{15}$ cm^{-3}. Such values of N_A correspond to the doping level of silicon in the experimental structures in Refs. 3 and 27. Approximately the same values of $F(M)$ as in Ref. 3 and 27 were observed in Ref. 1. The somewhat smaller theoretical value $F = F_{\text{th}}$ compared with the experimental value $F = F_{\text{exp}}$ can be attributed to the following factors.

First, in a real situation the exponent s_B in Miller's relation for $V_N \rightarrow V_{NB}$ is smaller than the value given by formula (10).[18,19] This is due to the ability of holes to also effect impact ionization, which, in principle, cannot be taken into account by the δ-function approximation[15] when they are not injected from the W-layer into the N-layer. Since, when such injection occurs, even the δ-function approximation gives a value $s_B < s_{nB}$ (Refs. 15, 18, and 19) (in the case of appreciable injection s_B can be as much as four times smaller than s_{nB}[18,19]). Third, the carrier multiplication in the W-layer was neglected in our treatment. Such an approximation (like the neglect of carrier multiplication in the highly doped part of a sharply asymmetric $p-n$ homojunction[28]) is not always permissible even when there is large difference between the gap widths in the W- and N-layers.[29] The last two factors are possibly responsible for the roughly threefold increase in the value of $F_{\text{exp}}(M)$ in Ref. 2 in comparison to the values of $F_{\text{exp}}(M)$ in Refs. 1, 3, and 27 [we also note that for $N_A > 10^{16}$ cm^{-3} (Ref. 2) the value of s_{nB} falls off with increasing N_A (Refs. 18 and 19)].

[1] T. M. Burbaev, V. V. Kravchenko, V. A. Kurbatov, and V. É. Shubin, Kratk. Soobshch. Fiz. , No. 4, 19 (1990).
[2] A. P. Boltaev, T. M. Burbaev, G. A. Kalyuzhnaya *et al.*, Fiz. Tekh. Poluprovodn. **29**, 1220 (1995) [Semiconductors **29**, 630 (1995)].
[3] N. Bacchetta, D. Bisello, Z. Sadygov *et al.*, Nucl. Instrum. Methods Phys. Res. A **387**, 225 (1997).
[4] R. J. McIntire, IEEE Trans. Electron Devices **ED-13**, 164 (1966).
[5] A. C. Tager and V. M. Val'd-Perlov, *Avalanche Diodes and Their Application in Microwave Technology* [in Russian], Sov. Radio (1968), 480 pp.
[6] G. E. Stillman and C. M. Wolf, in *Semiconductors and Semimetals*, R. K. Willardson and A. C. Beer (Eds.), Academic Press, New York and other cities (1977), Vol. 12, pp. 291–393.
[7] *Semiconductors and Semimetals. Lightwave Communication Technology. Photodetectors*, W. T. Tsang (Ed.), Academic Press, Orlando, FA (1985) [Russ. transl., Mir, Moscow (1988), 528 pp.].
[8] S. M. Sze and G. Gibbons, Appl. Phys. Lett. **8**(5), 111 (1966).
[9] I. V. Grekhov and Yu. N. Serezhkin, *Avalanche Breakdown of a p–n Junction in Semiconductors* [in Russian], Énergiya, Leningrad (1980), 152 pp.
[10] S. M. Sze, *Physics of Semiconductor Devices*, 2nd ed. Wiley-Interscience, New York (1969) [Russ. transl., Mir, Moscow (1984), Vol. 1, 455 pp.].
[11] V. A. Kuz'min, N. N. Kryukov, A. S. Kyuregyan, T. P. Mnatsekanov, and V. B. Shuman, Fiz. Tekh. Poluprovodn. **9**, 735 (1975) [Sov. Phys. Semicond. **9**, 481 (1975)].
[12] E. H. Nicollian and J. R. Brews, *MOS Physics and Technology*, Wiley, New York (1982), 908 pp.
[13] V. V. Osipov, A. A. Pankratov, and V. A. Kholodnov, Pis'ma Zh. Tekh. Fiz. **14**, 1889 (1988) [Sov. Tech. Phys. Lett. **14**, 819 (1988)]; Fiz. Tekh. Poluprovodn. **23**, 1148 (1989) [Sov. Phys. Semicond. **23**, 719 (1989)].
[14] V. A. Kholodnov, Pis'ma Zh. Tekh. Fiz. **14**, 551 (1988) [Sov. Tech. Phys. Lett. **14**, 246 (1988)].
[15] N. Kh. Artsis and V. A. Kholodnov, Radiotekh. Elektron. **29**, 151 (1984).
[16] W. T. Read, Bell Syst. Tech. J. **37**, 401–446 (1958).
[17] S. L. Miller, Phys. Rev. **99**, 1234 (1955).
[18] V. A. Kholodnov, Pis'ma Zh. Tekh. Fiz. **14**, 1349 (1988) [Sov. Tech. Phys. Lett. **14**, 589 (1988)].
[19] V. A. Kholodnov, Fiz. Tekh. Poluprovodn. **30**, 1051 (1996) [Semiconductors **30**, 558 (1996)].
[20] R. Leguerre and J. Urgell, Solid-State Electron. **19**, 875 (1976).
[21] A. P. Shotov, Zh. Tekh. Fiz. **28**, 437 (1958) [Sov. Phys. Tech. Phys. **3**, 413 (1958)].
[22] S. V. Bogdanov, A. B. Kravchenko, A. F. Plotnicov, and V. E. Shubin, Phys. Status Solidi A **93**, 361 (1986).
[23] G. E. Stillman, L. W. Cook, N. Tabatanaie, G. E. Bulman, and V. M. Robbins, IEEE Trans. Electron Devices **ED-30**, 364 (1983).
[24] R. D. Baertsch, J. Appl. Phys. **38**, 4267 (1967).
[25] V. V. Gavryushko, O. V. Kosogov, and V. D. Lebedev, Fiz. Tekh. Poluprovodn. **12**, 2351 (1978) [Sov. Phys. Semicond. **12**, 1398 (1978)].
[26] M. J. Buckingham, *Noise in Electronic Devices and Systems*, E. Horwood, Chichester; Halsted Press, New York (1983) [Russ. transl., Mir, Moscow (1986), 400 pp.].
[27] Z. Ya. Sadygov, ''Physical processes in avalanche photodetectors based on silicon/wide-band-layer structures,'' Doctoral Dissertation, Moscow Engineering-Physics Institute, Moscow (1997), 136 pp.
[28] V. A. Kholodnov, Opt. Zh. **6**, 53 (1996).
[29] V. A. Kholodnov and N. E. Kurochkin, Pis'ma Zh. Tekh. Fiz. **24**(17), 9 (1998) [Tech. Phys. Lett. **24**(9), 668 (1998)].

Translated by P. Shelnitz

Instability of a Bose condensate of neutral atoms in an external light field of nonuniform intensity

I. E. Mazets

A. F. Ioffe Physicotechnical Institute, Russian Academy of Sciences, St. Petersburg
(Submitted October 20, 1998)
Pis'ma Zh. Tekh. Fiz. **25**, 77–81 (May 12, 1999)

The existence of a new of type of instability of a Bose condensate in a rarefied atomic gas due to momentum exchange with an external resonant spatially nonuniform radiation field is demonstrated theoretically. [S1063-7850(99)01405-6]

The creation of a Bose condensate of rarefied atomic gases is one of the most interesting achievements in atomic physics in recent years. The experimental results of various groups were generalized, for example, in the reviews in Refs. 1 and 2, while the current theory was illuminated in Ref. 3. The main interest is this subject stems from the fact that a Bose condensate of an atomic gas is a mesoscopic system, in which the interaction of the particles is characterized by a single parameter (which can be determined fairly reliably by experimental means), viz., the scattering length of the atoms in an *s*-wave upon a binary collision. This presents a possibility for a first-principles calculation of the macroscopic parameters of a system of interacting particles and, accordingly, for testing the fundamental conceptions of the physics of nonideal gases and condensed media.

It has also aroused interest in the investigation of collective excitations of a Bose condensate, particularly the propagation of sound waves in it.[2] It should be noted that the dynamics of collective excitations are decisively influenced by the fact that a condensate consists of atoms confined in a magnetic trap.[4,5] The eigenfrequencies of the modes of such a system are proportional to the fundamental frequency of the trap, but the proportionality factor is expressed by an irrational number in the case of a sufficiently large number of atoms in the condensate.[3,4]

All calculations of the imaginary part of the oscillation frequency have hitherto revealed only damping for diverse conditions. This paper presents the first theoretical calculation that predicts the development of an instability (exponential growth of a small disturbance) in a condensate under definite conditions, which are associated with the effects of external electromagnetic radiation.

Let us consider an ensemble of atoms in state 1 (which can be identified with, for example, the $|F=1,\ m_F=-1\rangle$ sublevel of the hyperfine structure of the ground state of an alkali metal). The atom is subjected to the action of bichromatic laser radiation, which causes stimulated Raman transitions between states 1 and 2 (the latter should also be held in a trap, as, for example, $|F=2,\ m_F=1\rangle$; in addition, the linewidth of the Raman transition between the components of the hyperfine structure is small, so that it can be neglected). The effective Rabi frequencies of the transitions is u, the detuning from two-photon resonance equals Ω, and the momentum $\mathbf{q}$, which is equal to the difference between photons in the first and second modes of the light field, is transferred to the atom during a transition. Then, if Ω is significantly greater than both the Rabi frequency and the fundamental frequency of the trap, level 2 can be excluded adiabatically, and the ''quantum-hydrodynamic'' equations of the Bose condensate take the form

$$\frac{\partial}{\partial t}n+\mathrm{div}(n\mathbf{v})=0,$$

$$M\frac{\partial}{\partial t}\mathbf{v}+\mathrm{grad}\left[\frac{M\nu^2}{2}+U_{\mathrm{ext}}(\mathbf{r})+gn+\frac{u^2}{\Omega-\mathbf{q}\cdot\mathbf{v}}\right]=0. \qquad (1)$$

Here n and $\mathbf{v}$ are the local values of the density and velocity of the condensate, respectively; M is the mass of an atom; g is a constant, which characterizes the interatomic interaction and is proportional to the scattering length; and $U_{\mathrm{ext}}(\mathbf{r})=M/2\,(\omega_x^2x^2+\omega_y^2y^2+\omega_z^2z^2)$ is the trap potential, which is assumed to be harmonic. We use a system of units in which Planck's constant is taken as unity.

The main difference between Eqs. (1) and the equations which describe a condensate in the absence of laser radiation[3–5] is the inclusion of the light shift $u^2/(\Omega-\mathbf{q}\cdot\mathbf{v})$, inwhich the Doppler effect is taken into account, in the energy per atom in the condensate. The stationary solution of Eqs. (1) corresponds to a quiescent condensate (the stationary values of the density and velocity are labeled by the subscript 0):

$$n_0=\frac{1}{g}\left(\mu-U_{\mathrm{ext}}-\frac{u^2}{\Omega}\right),\quad \mathbf{v}_0=0. \qquad (2)$$

Here μ is the chemical potential. Let us now consider a disturbance (the quantities for it are marked with a prime sign) on the background of the state (2). The system (1) should be linearized with respect to n' and $\mathbf{v}'$. After elimination of the density disturbance, it reduces to the following equation in partial derivatives:

$$\frac{\partial^2\mathbf{v}'}{\partial t^2}+\mathrm{grad}\left(\mathbf{V}\frac{\partial\mathbf{v}'}{\partial t}\right)-\mathrm{grad}\,\mathrm{div}(n_0\mathbf{v}')=0. \qquad (3)$$

The characteristic velocity $\mathbf{V}=(u^2\mathbf{q}/\Omega^2M)$appears as a result of momentum transfer from the field to an atom when

the latter is excited to state 2, which is occupied with a probability equal to u^2/Ω^2. We stress that spatial nonuniformity of the beam can arise and u depends explicitly on the coordinates in the general case. Let us now make some assumptions regarding the form of the trap. As in most experiments,[1,2] its form is assumed to be prolate, i.e., $\omega_x \ll \omega_y, \omega_z$. Then oscillations occurring alongthe x axis do not cause appreciable motion in the perpendicular direction,[5] and the problem reduces essentially to the one-dimensional case. We also assume that the vector **q** is directed parallel to the x axis and, to fix ideas, in the positive direction.

We also assume that the square of the Rabi frequency of the two-photon transition is linearly dependent on the coordinate: $u^2=\tilde{u}^2(1+\beta x)$. In this case the function $V(x)$ will also be linear, i.e., $V=\tilde{V}(1+\beta x)$, and the equilibrium density will take the form $n_0=(M\omega_x^2/2g)[R_x^2-(x+x_0)^2]$ for $|x+x_0|<R_x^2$, where $x_0=u^2\beta/(\Omega M\omega_x^2)$. In this case Eq. (3) is written as

$$\frac{\partial^2}{\partial t^2}\nu' + \frac{\partial}{\partial x}\left[\tilde{V}(1+\beta x)\frac{\partial}{\partial t}\nu'\right] - \frac{\partial^2}{\partial x^2}\left[\frac{\omega_x^2}{2}(R_x^2-x^2)\nu'\right]=0. \tag{4}$$

It is easy to find a partial solution, which does not depend on the coordinate, i.e., which describes dipole oscillations of the condensate as a whole in the trap:

$$\nu'(t)=\nu'(0)e^{-\tilde{V}\beta t/2}\cos(\omega_x' t+\alpha),$$
$$\omega_x=\sqrt{\omega_x^2-(\tilde{V}\beta/2)^2}, \tag{5}$$

where $\nu'(0)$ and α are the amplitude and initial phase of the oscillations. If $\beta<0$ (we note that $\tilde{V}>0$ by definition), i.e., if the field intensity decreases in the direction in which the momentum transfer is oriented, the oscillation amplitude increases. This can easily be understood on the basis of Eq. (1): if the condensate moves as whole parallel to the x axis in the positive direction, the proximity of the Raman transition to resonance varies as a consequence of the Doppler effect, and, regardless of the sign of Ω, the light shift is modified so that the minimum of the energy per atom is shifted relative to x_0 toward larger values of x. Because of momentum exchange with the field, an additional force begins to act on the atoms, accelerating them parallel to the x axis in the positive direction. Energy is transferred from the field to the translational degree of freedom of the condensate, and growth of the oscillations according an exponential law takes place.

If $\beta>0$, oscillations of the condensate and the transfer of momentum from the field occur in antiphase, and the oscillations are damped.

Let us obtain some estimates. The maximum possible value of the velocity is determined by the wave number of a photon of the radiation field and is equal to about 1 cm/s for alkali metals. We also take $u^2/\Omega^2\approx 0.2$ and $\beta\approx R_x^{-1}$. Taking into account that the characteristic dimension of a condensate is about 0.01 cm,[1,2] we obtain a growth rate of the oscillations of the order of 10 s^{-1}. This value is already comparable to the value of the experimentally observed damping[2] (about 4 s^{-1}), which is usually identified with the Landau mechanism.[3] Thus, we can hope to detect the phenomenon theoretically considered in this paper already at the present level of the development of the experimental means.

In practice, a gradient of the radiated intensity can be created when light beams focused to a diameter of the order of R_x intersect. Another interesting possibility is associated with the use of an optically dense ensemble of atoms in the trap; however, in that case the cooling of the atoms must be continued continuously in order to maintain a balance between the number of particles which have passed into the condensate and the number which have left it as a result of the incoherent scattering of a photon upon resonant fluorescence.

This work was supported by the ''Basic Metrology'' State Scientific Program.

We thank Corresponding Member of the Russian Academy of Sciences D. A. Varshalovich and Prof. W. Ketterle for some useful discussions.

[1] W. Ketterle, M. R. Andrews, K. B. Davis *et al.*, Phys. Scr. **66**, 31 (1998).
[2] M. R. Andrews, D. S. Durfee, S. Inouye *et al.*, J. Low Temp. Phys. **110**, 153 (1998).
[3] L. P. Pitaevskiĭ, Usp. Fiz. Nauk **168**, 641 (1998) [Phys. Usp. **41**, 569 (1998)].
[4] S. Stringari, Phys. Rev. Lett. **77**, 2360 (1996).
[5] Yu. M. Kagan, E. L. Surkov, and G. V. Shlyapnikov, Phys. Rev. A **54**, R1753 (1996).

Translated by P. Shelnitz

Suppression of large-scale structures in a gas-saturated impact jet

S. V. Alekseenko, D. M. Markovich, and V. I. Semenov

Institute of Thermal Physics, Russian Academy of Sciences, Siberian Branch, Novosibirsk
(Submitted June 2, 1998)
Pis'ma Zh. Tekh. Fiz. **25**, 82–88 (May 12, 1999)

The suppression of large-scale vortex formations under gas-saturation conditions is detected on the basis of measurements of the pulsation component of the surface friction when an axisymmetric hot jet of a fluid impinges on an obstacle. The conditions for the resonant enhancement of coherent structures and the suppression of broad-band turbulence are determined for single-phase and gas-saturated impact jets. The evolution of various pulsation components in the gradient region of an impact jet is analyzed. © *1999 American Institute of Physics.* [S1063-7850(99)01505-0]

As a rule, the bubbles in gas-liquid bubbly flows are not simply tracers moving with the flow. On the contrary, nonuniformity of the velocity field can lead both to dispersion of the bubbles and to variation of the level of fluctuations in the continuous phase. The effects can often be mutual when the local nonstationary turbulence of the continuous phase influences the trajectory of the dispersed phase (turbulent dispersion) and the positions of the bubbles and the wakes behind them influence the turbulence in the liquid (turbulence modulation).

Significant variation of the turbulent characteristics of flows in the presence of a second phase has been observed in many experimental studies. It was concluded in the review in Ref. 1 that in most cases small particles reduce the intensity of turbulence in a flow, while large particles enhance it. The main mechanisms determining the influences acting on a turbulent structure are: the dissipation of turbulent kinetic energy on particles, increases in the effective viscosity due to the presence of particles, the generation of vortices or the formation of wakes behind particles, the entrainment of liquid by a particle (the added-mass effect); increases in the velocity gradients between two particles, and the deformation and oscillation of the boundaries of the dispersed phase. Different mechanisms from the list just enumerated can dominate, depending on the concentration of the dispersed phase, the dimensions of the particles, and the character of the flow.

Free shear flows, particularly turbulent jets, have been studied to the least extent in regard to the influence of a second phase on turbulence. The principal special feature of jet flows is the presence of large-scale vortex formations (coherent structures) in the mixing layer. A periodic influence acting on such a flow with frequencies from the region of greatest susceptibility of the jet is known to permit effective control of the large-scale structure of the flow up to resonant enhancement of the coherent structures and an influence on the broad-band turbulence.[2,3] The characteristics of turbulent bubble jets have been investigated in several studies,[4–6] but the mutual influence of the gas phase and the large-scale structure of the jet mixing layer has scarcely been examined.

The present work was devoted to an experimental study of the evolution of instabilities in the shear layer of an axisymmetric impact jet in the presence of a finely dispersed gas phase. The main results regarding the turbulent structure of the flow were obtained using an electrodiffusion method for measuring the tangential stress on the wall.

The experimental apparatus was a closed hydrodynamic loop consisting of a working section, a reservoir, a system of connecting tubes, and measuring instruments. The working section was a Perspex channel of rectangular cross section measuring $162\times 86\times 2000$ mm. A nozzle unit was inserted horizontally into the channel through a lateral wall. The nozzle used had a diameter of 10 mm and biradial generatrix. The ratio between the nozzle outlet diameter and the throat diameter was 1:4. The velocity profile at the nozzle tip was nearly uniform, and the momentum loss thickness at $x/d=0.15$ was $\theta\approx 0.1$ mm. The measured degree of natural turbulence at that distance was $u'/U_0=\sqrt{\overline{u'^2}}/U_0=0.005-0.008$ on the nozzle axis and $0.05-0.06$ at the center of the mixing layer.

An electrodiffusion method was used to measure the local values of the velocity and tangential stress on the wall. Details of the method were presented in Ref. 7. Tangential-stress sensors were placed on the moving wall of the channel, onto which the jet impinged. The accuracy of the measurement of the translation of the wall was 0.1 mm.

The jet was excited by a standard ESE 201 electrodynamic vibrator with the aid of a bellows connected to a damping chamber. The initial sinusoidal oscillations had a zero-order mode, and their rms value varied from $\tilde{u}/U_0=\sqrt{\overline{\tilde{u}^2}}/U_0=0.0001$ to 0.001, depending on the experimental conditions. The excitation frequency f_f was characterized by the Strouhal number $\mathrm{Sh}_d=f_f\cdot d/U_0$. The experiments showed that superimposed small-amplitude oscillations have essentially no effect on the flow characteristics near the nozzle rim.

Air bubbles were fed into the distributing unit through a finely porous plate by a compressor. The volume flow rate was varied during the experiment from 0 to 164 l/h. This corresponds to a volumetric gas content $\alpha=0-12.1\%$ for a

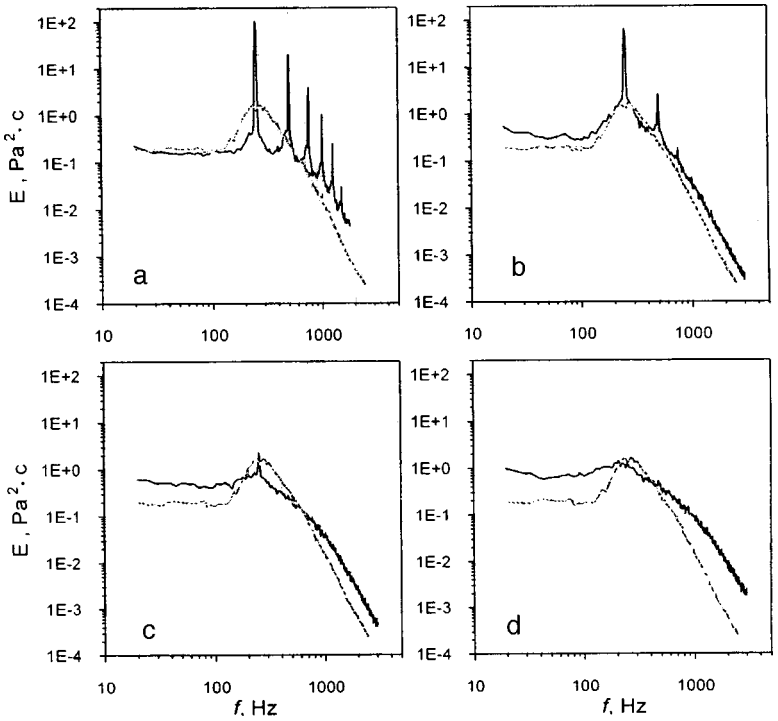

FIG. 1. Spectral density of pulsations of the tangential stress on the wall. Gray lines — unexcited single-phase jet. $H/d=2$, $f_f=250$ Hz ($\mathrm{Sh}_d=0.6$), Re=40400, $r/d=1.1$. a — $\alpha=0$; b —3.4%; c — 5.9%; d — 10.1%.

liquid flow rate $Q_l=0.33$ l/h. The mean diameter of the bubbles was 200 μm, and the spread of their diameters was small; therefore, the gas phase was regarded as monodisperse in these experiments.

The experiments were performed for two Reynolds numbers: Re=25200−40400. Here $\mathrm{Re}=U_0\cdot d/\nu$, U_0 is the mean velocity of the liquid at the nozzle tip, d is the diameter of the nozzle, and ν is the kinematic viscosity of the solution used, which equals 1.04×10^{-6} m^2. The distance between the nozzle rim and the plane was not varied in the experiments and was equal to 20 mm ($H/d=2$).

The basic information on the turbulent structure of the flow in the near-wall region was obtained by measuring the averaged and pulsation values of the tangential stress on an obstacle in the flow, as well as the spectral characteristics.

It is known[3,8] that if the mixing layer is excited at a frequency lying in the vicinity of the most probable frequency f_{mp} for the conditions under consideration, the coherent structures will be resonantly enhanced at that frequency. In the present case (Re=40400) the sensitivity range lies in the interval $190<f_f<350$ Hz ($0.45<\mathrm{Sh}_d<0.83$), where f_f is the excitation frequency. Excitation at the most probable frequency $f_f=250$ Hz ($\mathrm{Sh}_d=0.6$) leads to overall lowering of the frictional resistance by more than 30%. The pulsation level increases by almost two fold, predominantly due to the increment of the coherent component. Thus, in the zone of intense penetration of the structures into the near-wall region the spectral density of the pulsations at the resonance frequency increases by two orders of magnitude in comparison to the unexcited jet (Fig. 1a). The distributions of the integral characteristics of the jet become similar to the distributions for small Reynolds numbers,[9] and the spectral dependences (Fig. 1a) lead to the conclusion that a significant portion of the stochastic friction pulsations is suppressed at moderate frequencies. Thus, it can be stated that quasilaminarization of the flow occurs upon resonant enhancement of large-scale vortex structures. When the jet is excited at frequencies lying above the range of greatest sensitivity, only weak enhancement of the fundamental harmonic, which does not alter the basic flow characteristics, can be observed. Excitation at low frequencies leads to enhancement of multiple harmonics, i.e., $2f_f$, $3f_f$, etc., if they are suppressed in the range of greatest sensitivity. The amplitude of the superimposed oscillations has essentially no influence on the flow characteristics in the range investigated.

The measurements for a two-phase jet were performed at high Reynolds numbers, Re=25200 and 40400, for the purpose of excluding effects associated with the lift of bubbles by Archimedes forces. These effects are insignificant for large Reynolds numbers and small bubble dimensions. For example, when Re=40400, the difference between the measured values of the tangential stress on the wall at points (upper and lower) that are symmetric relative to the horizontal axis of the flow amounted to no more than 5% for all the gas contents investigated. Saturation of the jet with gas leads to a significant increase in the mean friction, but the character of the flow remains unchanged up to values of the gas content $\alpha=8-9\%$. The amplitude of the rms friction pulsations relative to the friction maximum for each gas content falls off monotonically over the entire region of flow, with the exception of the vicinity of the critical point, where the absolute pulsation level rises. At $\alpha>8-9\%$ the flow structure undergoes changes, the near-wall characteristics loss their clearly expressed jet character, and the pulsation maximum moves closer to the critical point. Figures 1b–d compare the spectral density distributions of the friction pulsations at the point on the obstacle where the large-scale vortex structures penetrate from the jet mixing layer with the high-

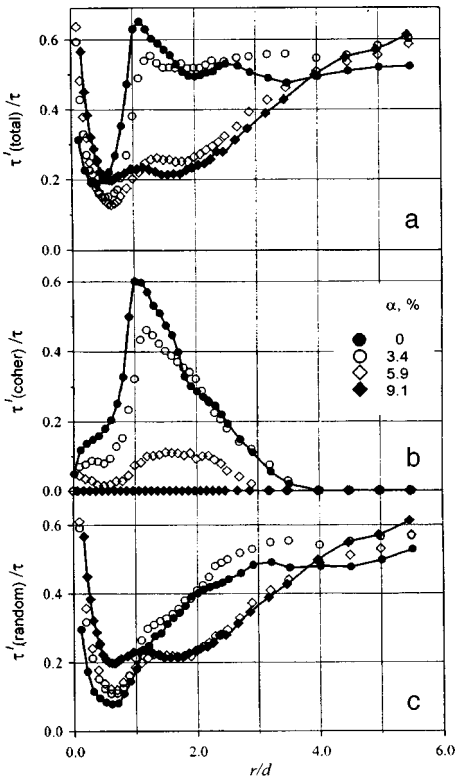

FIG. 2. Total (a), coherent (b), and stochastic (c) components of the surface friction pulsations as a function of gas content. $H/d=2$, $f_f=250$ Hz ($\mathrm{Sh}_d=0.6$), Re=40400.

est intensity ($r/d=1.1$). Suppression of the coherent component of the pulsations with increasing gas content is clearly observed. At significantly higher gas contents the coherent component essentially vanishes from the spectra for all values of r/d.

An analysis of the evolution of the coherent and stochastic components of the pulsations along the radial coordinate reveals (Fig. 2) that the coherent component of the pulsations is significant only in a definite range of radial coordinates ($0.5<r/d<3$) and falls off to zero with increasing gas content at $\alpha>8\%$. In Fig. 2 $\tau'(\mathrm{total}/\tau$, $\tau'(\mathrm{coher})/\tau$, and $\tau'(\mathrm{random})/\tau$ are,respectively, the rms values of the total, coherent, and stochastic components of the tangential stress pulsations relative to the averaged value of the friction at the respective point. At $r/d>3$ the main contribution to the turbulent energy is made by the stochastic pulsations. The level of stochastic pulsations relative to the local value of the mean friction in this region varies weakly as the gas content increases (Fig. 2c). This conclusion is attributed to the decrease in the local concentration of bubbles with increasing distance from the critical point.

Thus, the suppression of stochastic turbulent pulsations upon the resonant enhancement of large-scale organized structures in an excited impact jet, as well as the suppression of these structures when the jet is saturated with a finely dispersed gas phase, have been detected in this work. The results obtained can serve as a basis for developing methods to control heat and mass transfer in confined two-phase jet flows.

This work was carried out as part of Project 274 of the ''Basic Research in the Area of Physics and High Technologies'' Section of the Federal Special-Purpose Program ''State Support of the Integration of Higher Education and Basic Science in 1997–2000.''

[1] R. A. Gore and C. T. Crowe, Int. J. Multiphase Flow **15**, 279 (1989).
[2] S. C. Crow and F. H. Champagne, J. Fluid Mech. **48**, 547 (1971).
[3] C. M. Ho and L. S. Huang, J. Fluid Mech. **119**, 443 (1982).
[4] V. W. Goldschmidt, M. K. Householder, and S. C. Chuang, in *Progress in Heat and Mass Transfer*, Pergamon Press, Oxford (1971), Vol. 6, pp. 487–508.
[5] J. H. Milgram, J. Fluid Mech. **85**, 345 (1983).
[6] T.-Y. Sun and G. M. Faeth, Int. J. Multiphase Flow **12**, 99 (1986).
[7] S. V. Alekseenko and D. M. Markovich, J. Appl. Electrochem. **24**, 626 (1994).
[8] S. V. Alekseenko, D. M. Markovich, and V. I. Semenov, in *Proceedings of the 4th World Conference on Experimental Heat Transfer, Fluid Mechanics, and Thermodynamics*, Brussels, (1997), Vol. 3, pp. 1815–1822.
[9] S. V. Alekseenko, V. V. Kulebyakin, and D. M. Markovich *et al.*, Inzh.-Fiz. Zh. **69**, 615 (1996).

Translated by P. Shelnitz

38-GHz relativistic backward-wave tube based on a modulator with an inductive energy accumulator and a semiconductor current interrupter

S. K. Lyubutin, G. A. Mesyats, S. N. Rukin, B. G. Slovikovskiĭ, V. G. Shpak, S. A. Shunaĭlov, M. R. Ul'maskulov, and M. I. Yalandin

Institute of Electrophysics, Russian Academy of Sciences, Ekaterinburg
(Submitted January 15, 1999)
Pis'ma Zh. Tekh. Fiz. **25**, 89–95 (May 12, 1999)

The results of an investigation of a 38-GHz relativistic backward-wave tube with an output power up to 40 MW are presented. An electron-beam injector based on a 5-ns high-current pulsed periodic modulator with an inductive energy accumulator and a semiconductor current interrupter is used for the first time in experiments. © *1999 American Institute of Physics.* [S1063-7850(99)01605-5]

1. Since the nineteen-eighties the efforts to perfect high-current nanosecond electron accelerators[1] have permitted the creation of relativistic microwave generators with pulsed periodic operation. The most powerful among them are the relativistic backward-wave tubes for the millimeter and centimeter wavelength ranges.[2–4] An operating regime of these devices with repetition rates up to hundreds of hertz became accessible when effective charge devices were developed for high-voltage generators on the basis of forming lines[5] and the conditions for the stable operation of gas discharges were found.[6]

Since the appearance of high-voltage high-current semiconductor current interrupters[7] it has been possible, in principle, to create high-power nanosecond modulators with an inductive energy accumulator that can support a periodic operating regime of an accelerator with a repetition rate greater than 1 kHz and high amplitude stability. The discovery of subnanosecond current cutoff in SOS diodes[8] and new circuit designs and technical solutions made it possible to subsequently obtain peak powers of 300–500 MW with a pulse duration of 5–6 ns on 150–200-Ω resistive loads. These parameters are close to the values achieved for miniature generators with forming lines and spark dischargers.[1,4] Voltage pulses with an amplitude of $\sim$250 kV are already perfectly suitable for generating the electron beam needed to excite a 38-GHz relativistic backward-wave tube. The purpose of the present work was to experimentally verify such a possibility and to determine the operating features of a modular with a semiconductor current interrupter and a load in the form of a magnetically insulated coaxial diode.

2. The experimental setup (Fig. 1) included a high-voltage modulator with an inductive energy accumulator and a semiconductor interrupter, a magnetically insulated coaxial diode containing a graphite explosive-emission cathode, and an electrodynamic delay system for the backward-wave tube in the form of a circular corrugated waveguide, which provides for synchronism of electrons having an energy of $\sim$250 keV with the first backward spatial harmonic of the wave (E_{01}). The output of the delay system was connected to a conical horn antenna. The residual pressure in the system was 10^{-2} Torr.

To form and transport a tubular electron beam with a diameter of 5.5 mm and a current equal to $\sim$1 kA, the graphite cathode was immersed in a longitudinal magnetic field created by a pulsed solenoid. A field strength of 50 kOe was provided in the single-pulse regime. The field strength reached 15 kOe at repetition rates up to 15 Hz, and the short-term repeated-pulse operating regime was limited by the design of the solenoid, which did not have forced cooling.

The pump current of the semiconductor interrupter and the voltage on the load were monitored in the experiments. The electron-beam current was measured by a Faraday cylinder, which was installed in the drift chamber instead of the delay system for this purpose. The peak power of the microwave pulse was measured by scanning the radiation pattern using a silicon hot-carrier detector. All the measuring devices were calibrated and had times for the transient processes from 1.5 ns (the microwave detector) to 150 ps (the beam-current pickup). The configuration of the magnetically insulated coaxial diode (Fig. 1) had small dimensions. The radial gap between the cathode and the anode was equal to 4 mm, and the axial gap (between the end surface of the cathode and the anode constriction) was equal to 10 mm. The Faraday cylinder was installed in the drift chamber at a distance of 10 mm from the entrance.

3. The absence of spark dischargers with their characteristic deficiencies is a fundamental feature of the experimental setup. The high-voltage modulator circuit is connected galvanically to the cathode of the magnetically insulated coaxial diode. Therefore, the switching process of the saturated magnetic switch in the next-to-last energy-compression unit at a time $\sim$200 ns before current cutoff in the interrupter leads to the appearance of a negative prepulse with an amplitude of 20 kV and a duration of 70 ns on the load (Fig. 2a). The finite resistance of the semiconductor interrupter, in turn, is responsible for the appearance of a positive prepulse ($\sim$40 ns, 15 kV) in the forward current pumping stage, and a negative prepulse of approximately the same amplitude with a duration of $\sim$20 ns is generated in the backward pumping stage before the moment of current cutoff (Fig. 2c). Thus, the prepulses are caused, in principle, by the circuit design of the last energy-compression cascade. This is an important differ-

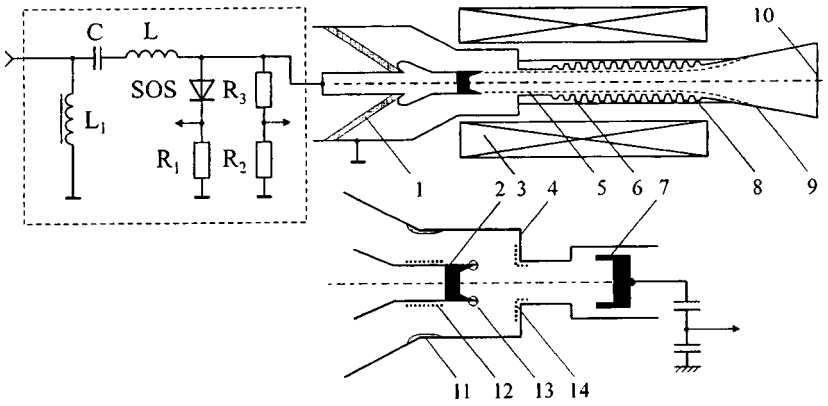

FIG. 1. Diagram of the experimental setup: *C* — capacitive accumulator; *L* — inductive accumulator; L_1 – saturated choke; SOS — semiconductor interrupter; R_1–R_3 — current shunt and resistive divider; *1* — insulator; *2*— cathode; *3* — solenoid; *4* — anode; *5* — electronbeam; *6* — grounding system; *7* — Faraday cylinder; *8* — vacuum driftchamber; *9* — horn antenna; *10* — vacuum microwave window; *11–14* — zones of the cathodic and anodic emission processes.

ence between a modulator with an inductive accumulator and a semiconductor interrupter, on the one hand, and systems with forming lines and dischargers, on the other hand.

4. It was previously shown in Ref. 9 that even when the duration is 1–2 ns and the amplitude is $\sim 10-15$ kV, the negative prepulse directly preceding the accelerating pulse plays a significant role in initiating electron emission on the cathode. Therefore, in the present experiments the presence of the prepulses of opposite polarity determined the operating features of the electron diode and the microwave generator itself.

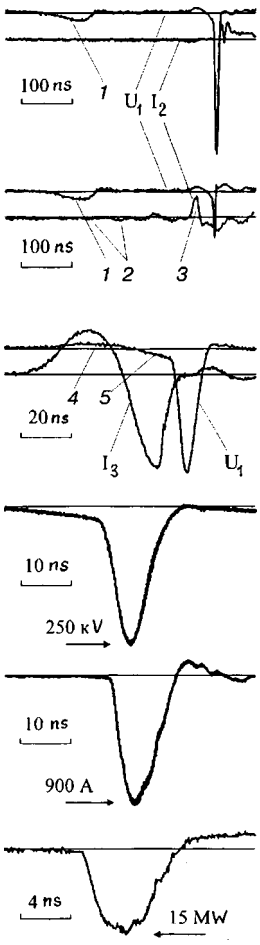

FIG. 2. Oscillograms: a — voltage on the vacuum diode (U_1) and beam current (I_2) in a regime without shunting of the interrupter; b — same signals in a regime without shunting of the interrupter; c — pump current of the interrupter (I_3) and voltage on the vacuum diode in the standard operating regime of the modulator; d, e — voltage on the vacuum diode and beam current recorded in the regime with the accumulation of 20 pulses; f — microwave pulse recorded in a stroboscopic regime with the accumulation of 100 pulses; *1–5* — prepulses.

The evolution of the emission processes in the magnetically insulated coaxial diode was determined from a set of oscillograms of the pump current, the voltage on the interrupter, and the beam current and erosion tracks on the electrodes. Several specific operating regimes of the magnetically insulated coaxial diode were noted. When intense electron emission developed from the cathode in prepulse *1* (Fig. 2b), a time interval of 200 ns was sufficient for expansion of the cathode plasma from region *13* (Fig. 1) in the axial and radial directions. When electrons impinged on the end surface of anode *4* (Fig. 1), a collector plasma appeared (erosion tracks in region *14*, Fig. 1). When the expansion velocities of the cathode-collector plasma in the radial and axial directions were $\sim 10^6$ and $\sim 10^7$ cm/s, respectively,[10] the electrode diode essentially completely shunted the interrupter. In this case (Fig. 2b) the output voltage dropped sharply, and the Faraday cylinder detected both an electron current from the cathode equal to $\sim 10-20$ A (pulses *2*, Fig. 2b),and a positive current surge with an amplitude of ~ 100 A, which appears when the plasma strikes the pickup (pulse 3, Fig. 2b). The plasma could arrive either from the cathode or the collector, i.e., from region *13* or *14* (Fig. 1). Itis noteworthy that the picture presented in Fig. 2b was rarely observed. This indicates the threshold, random character of the initiation of electron emission during the prepulse.

The interrupter pump current and the accelerating voltage pulse on the magnetically insulated coaxial diode in the usual regime are shown in Fig. 2c. Such a regime was achieved after activation of the electrodes of the magnetically insulated coaxial diode, which required from several tens to hundreds of pulses. During the activation, partial shunting of the interrupter was observed from time to time, which was associated with the development of electron emission from the anode electrode in positive prepulse *4* (Fig. 2c). Emissionzone *11* (Fig. 1) exhibited pronounced erosion, and the opposite surface *12* (Fig. 1) exhibited traces of ''treatment'' by the electron beam. As these processes evolved, the amplitude of the accelerating pulse decreased by 20–30%. As the electrodes were activated, the amount of

dephasing decreased, and the accelerating voltage pulse (Fig. 2d) and the beam pulse (Fig. 2e) became fairly stable. We note that the last two oscillograms were obtained for several tens of pulses by a Tek-TDS684B digital oscillogram in the envelop-accumulation mode. When stability of the accelerating voltage and the beam current was achieved, the microwave pulses were recorded at a frequency of 10–15 Hz in a stroboscopic regime with the accumulation of 40–100 pulses (Fig. 2f). In the single-pulse regime with a longitudinal magnetic field of 50 kOe the peak power of the microwave radiation was ~ 40 MW, and in the regime with pulse repetition it was $15-20$ MW. The maximum electron efficiency of the microwave generator was on the $10-15\%$ level.

5. Thus, an experimental setup, which has combined a high-current microwave instrument with and an electron diode based on an explosive-emission cathode and a modulator with an inductive accumulator and a semiconductor current interrupter for the first time, has been created. The stability of the generation of microwave radiation in such a system is shown to be determined to a considerable extent by the influence of the set of advanced prepulses of opposite polarity on the operation of the electron diode. It is theorized that optimization of the diode configuration, activation of the electrode surfaces, improvement of the vacuum conditions, and the employment of a constant magnetic field (a superconducting solenoid or a permanent magnet) will provide for operation of a microwave generator with a repetition rate above 1 kHz.

[1] G. A. Mesyats, in *Relativistic High-Frequency Electronics*, No. 4 [in Russian], Inst. Prikl. Fiz. SSSR, Gor'kiĭ (1984), pp. 192–216.
[2] N. F. Kovalev *et al.*, JETP Lett. **18**, 138 (1973).
[3] V. I. Belousov *et al.*, Pis'ma Zh. Tekh. Fiz. **4**(12), 1443 (1978) [Sov. Tech. Phys. Lett. **4**, 584 (1978)]; S. I. Krementsov, M. D. Raĭzer, and A. V. Smorgonskiĭ, Pis'ma Zh. Tekh. Fiz. **2**(10), 453 (1976) [Sov. Tech. Phys. Lett. **2**(5), 175 (1976)].
[4] M. I. Yalandin *et al.*, in *Proceedings of the 9thIEEE International Pulsed Power Conference*, Albuquerque, NM (1993), pp. 388–391.
[5] A. S. El'chaninov *et al.*, in *High-Current Pulsed Electron Beams in Technology* [in Russian], G. A. Mesyats (Ed.), Nauka, Novosibirsk (1983), pp. 5–21.
[6] A. S. El'chaninov *et al.*, Prib. Tekh. Eksp. No. 4, 162 (1979).
[7] S. K. Lyubutin *et al.*, in *Proceedings of the 11thIEEE International Pulsed Power Conference*, Baltimore, MD (1997), Vol. 2, pp. 992–998.
[8] S. K. Lyubutin *et al.*, Dokl. Akad. Nauk **360**, 477 (1998) [Phys. Dokl. **43**, 349 (1998)].
[9] M. I. Yalandin *et al.* in *Proceedings of the 17th International Symposium on Discharges and Electrical Insulation in Vacuum*, Berkeley, CA, (1996), Vol. 2, pp. 635–639.
[10] S. P. Bugaev *et al.*, in *Relativistic High-Frequency Electronics* [in Russian], Inst. Prikl. Fiz. SSSR, Gor'kiĭ (1979), pp. 5–75.

Translated by P. Shelnitz

The analogy between a problem of magnetohydrodynamics and the Benard problem in the Boussinesq approximation

N. B. Volkov, N. M. Zubarev, and O. V. Zubareva

Electrophysics Institute, Ural Branch, Russian Academy of Sciences, Ekaterinburg
(Submitted November 23, 1998)
Pis'ma Zh. Tekh. Fiz. **25**, 1–6 (May 26, 1999)

It is shown that the equations of motion written in a longitudinal plane of symmetry of a liquid-metal current-carrying conductor of rectangular cross section are identical with the equations that describe heat conduction in a flat layer of liquid heated from below in the Boussinesq approximation. The main parameters that determine the threshold of the convective instability that develops under the action of Lorentz forces in a current-carrying liquid metal are found. © *1999 American Institute of Physics.* [S1063-7850(99)01705-X]

Soliner *et al.*[1] proposed the hypothesis that there is an analogy between the initial stages in the development of turbulence in heat convection and the electrical explosion of a current-carrying conductor. This analogy was subsequently used to explain various physical effects in current-carrying plasmalike media: the stratification of a current-carrying conductor,[2] the formation of hot spots,[3] and the interruption of an electric current.[4,5] However, despite its fruitfulness, this analogy had only a qualitative character for the problems considered in Refs. 1–5. In this article, we shall show that the equations of magnetohydrodynamics written in a longitudinal symmetry plane of a current-carrying liquid-metal conductor with greatly differing dimensions in the cross section are identical with the equations that describe the formation of the so-called Benard cells during heat convection in the Boussinesq approximation.

Thus, let us consider a liquid-metal conductor of the following geometry: The cross section of the conductor is a rectangle with sides $2b$ and $2a$, which correspond to the y and x axes of a rectangular coordinate system. An electric current flows along the z axis, which is the symmetry axis of the conductor. We shall assume for simplicity that $a \ll b$ (in the limit $a/b \to 0$, this is the simplest case of plane geometry).

We shall assume the conductive liquid to be incompressible and its kinetic coefficients to be constant. The equations of magnetohydrodynamics then take the form

$$\frac{\partial \mathbf{v}}{\partial t} + (\mathbf{v}\cdot\nabla)\mathbf{v} = -\frac{1}{\rho}\nabla P + \frac{1}{4\pi\rho}((\nabla\times\mathbf{H})\times\mathbf{H}) + \nu\nabla^2\mathbf{v}, \tag{1}$$

$$\frac{\partial \mathbf{H}}{\partial t} + (\mathbf{v}\cdot\nabla)\mathbf{H} = (\mathbf{H}\cdot\nabla)\mathbf{v} + \nu_m\nabla^2\mathbf{H}, \tag{2}$$

$$\nabla\cdot\mathbf{v} = 0, \quad \nabla\cdot\mathbf{H} = 0, \tag{3}$$

where $\mathbf{v}$, $\mathbf{H}$, and P are, respectively, the velocity, the magnetic field, and the pressure; ρ is the density; $\nu = \eta/\rho$ is the kinematic viscosity (η is the dynamic viscosity); $\nu_m = c^2(4\pi\sigma)^{-1}$ is the magnetic viscosity; σ is the conductivity; and c is the velocity of light.

Since the perturbations that grow do not bend the magnetic field lines in first order, we shall assume that all the fields are symmetrical relative to the $y=0$ plane. In such a case, applying the curl operation to Eq. (2), we get in the $y=0$ symmetry plane of the conductor that

$$\left[\frac{\partial}{\partial t} - \frac{\partial v_y}{\partial y} + v_x\frac{\partial}{\partial x} + v_z\frac{\partial}{\partial z} - \nu\nabla^2\right]\left(\frac{\partial v_x}{\partial z} - \frac{\partial v_z}{\partial x}\right) = \frac{1}{4\pi\rho}\frac{\partial H_x}{\partial y}\frac{\partial H_y}{\partial z}, \tag{4}$$

$$\left[\frac{\partial}{\partial t} - \frac{\partial v_y}{\partial y} + v_x\frac{\partial}{\partial x} + v_z\frac{\partial}{\partial z} - \nu_m\nabla^2\right]H_y = 0, \tag{5}$$

where ∇^2 is the three-dimensional Laplace operator. Note that no simplifying assumptions were made in obtaining Eqs. (4) and (5), except for using the symmetry of the solutions.

Let us represent the magnetic field $\mathbf{H}$ as a sum of the unperturbed magnetic field corresponding to the absence of hydrodynamic motion in the conductor, $\mathbf{v}=0$, and a perturbation of the magnetic field:

$$\mathbf{H} = \mathbf{H_0} + \mathbf{h}.$$

To first order in the perturbations $\mathbf{v}$ and $\mathbf{h}$, the system of Eqs. (4) and (5) can be rewritten as

$$\left[\frac{\partial}{\partial t} - \nu\nabla^2\right]\left(\frac{\partial v_x}{\partial z} - \frac{\partial v_z}{\partial x}\right) = \frac{1}{4\pi\rho}\frac{\partial H_{0x}}{\partial y}\frac{\partial h_y}{\partial z}, \tag{6}$$

$$\left[\frac{\partial}{\partial t} - \nu_m\nabla^2\right]h_y = H_{0y}\frac{\partial v_y}{\partial y} - \frac{\partial H_{0y}}{\partial x}v_x. \tag{7}$$

The unperturbed magnetic field distribution over the conductor is determined by the Biot–Savart law:[6]

$$\mathbf{H}_0 = \int_V \frac{\mathbf{j}\times\mathbf{R}}{cR^3}dV = \int_S \frac{2\mathbf{j}\times\mathbf{r}}{cr^2}dS,$$

where $\mathbf{R}$ is the radius vector drawn from volume element dV of the conductor to the observation point, $\mathbf{r}$ is the projection of this vector onto the cross section of the conductor (the $\{x,y\}$ plane), and dS is an area element of this cross section.

Assuming the total current I through the conductor to be constant and the unperturbed current-density distribution to be homogeneous, we get the following for the unperturbed magnetic field close to the $y=0$ symmetry plane of the conductor to lowest order in the small parameter a/b:

$$\mathbf{H}_0=\left\{-\frac{2Iy}{cb^2},\frac{\pi Ix}{abc},0\right\}. \tag{8}$$

We introduce the pair of functions $h(x,z,t)=h_y|_{y=0}$ and $\psi(x,z,t)=\omega_y|_{y=0}$, where the vector field $\mathbf{w}$ is given by $\nabla\times\mathbf{w}=\mathbf{v}$ (the vector $\mathbf{w}$ can always be chosen so that, in the $y=0$ plane, it has only a component directed along the y axis). Using these functions and also assuming that the spatial scale of variation of the quantities is much greater along the y axis than along the x and z axes, we get from Eqs. (6) and (7) to lowest order in a/b the following system of equations, from which the spatial variable y has been eliminated:

$$\left[\frac{\partial}{\partial t}-\nu\Delta\right]\Delta\psi=\frac{I}{2\pi c\rho b^2}\frac{\partial h}{\partial z}, \tag{9}$$

$$\left[\frac{\partial}{\partial t}-\nu_m\Delta\right]h=\frac{\pi I}{cab}\frac{\partial\psi}{\partial z}, \tag{10}$$

where $\Delta=\partial^2/\partial x^2+\partial^2/\partial z^2$ is the two-dimensional Laplacian. If the perturbed magnetic field is replaced by by the temperature field, these equations are identical with the equations describing homogeneous heat convection in a flat layer of liquid heated from below in the Boussinesq approximation.[7] This is evidence that, in a resistive, viscous, current-carrying medium with a rigid boundary, under the action of Lorentz forces, large-scale hydrodynamic and current vortex structures can develop with a characteristic size on the order of the cross sectional size of the system. Such structures differ from heat-convection structures mainly in that there is a distinct direction (that in which the electric field points) that orients the spatial structures.

By analogy with the problem of thermal convection, where the Rayleigh number[8] was used as a control parameter, let us now introduce its analog:

$$\mathcal{R}\equiv\frac{8I^2a^3}{c^2b^3\nu\nu_m\rho}. \tag{11}$$

The critical value of this parameter, i.e., the value at which an initially unperturbed state of the system becomes unstable, is determined by the character of the boundary conditions. Thus, it is $\mathcal{R}_c=656$ for free boundaries,[9] $\mathcal{R}_c=1708$ when one boundary is rigid while the other is free,[8] etc. It is clear from Eq. (11) that the stability limit is determined by the total current through the conductor, with the threshold current being

$$I_c=c\left(\frac{b}{2a}\right)^{3/2}\sqrt{\mathcal{R}_c\nu_m\eta}. \tag{12}$$

Assuming, for example, that the ratio of the characteristic dimensions in the cross section of the conductor is $b/a=10$ and recalling that $\eta\sim10^{-2}$ Pa and $\nu_m\sim10^3$ cm^2/sec for most liquid metals, we get that I_c amounts to a few kiloamperes. This agrees in order of magnitude with the threshold values for current interruption in a eutectic,[4,5] as well as with characteristic currents in experiments on the electrical explosion of conductors[2] accompanied by the onset of large-scale instabilities.

It should be noted that, for liquid-metal conductors of cylindrical geometry, convective structures (annular vortices) can be generated only when the current through the conductor is increasing;[2,5] when the current is constant, unlike the situation considered in this article, spontaneous appearance of the structures is impossible.

Note also that, as can be seen from Eq. (12), instability is possible only in the presence of curvature of the magnetic field lines (as $b\to\infty$, the critical currents become infinite). This is because, in this limit, the Lorentz force becomes a potential force and consequently has no effect on the rotational motion of the medium.

It is interesting that, if we formally assume that close to the symmetry plane the perturbation h_y depends only on the spatial variables x and z (and is independent of y), the nonlinear equations of motion take the form

$$\frac{\partial\Delta\psi}{\partial t}=\frac{\partial(\Delta\psi,\psi)}{\partial(x,z)}+\frac{I}{2\pi c\rho b^2}\frac{\partial h}{\partial z}+\nu\Delta\Delta\psi, \tag{13}$$

$$\frac{\partial h}{\partial t}=\frac{\partial(h,\psi)}{\partial(x,z)}+\frac{\pi I}{cab}\frac{\partial\psi}{\partial z}+\nu_m\Delta h, \tag{14}$$

where $\partial(f,g)/\partial(x,z)=(\partial f/\partial x)(\partial g/\partial z)-(\partial f/\partial z)(\partial g/\partial x)$ is the Jacobian. This system is identical with the system that describes the nonlinear dynamics of perturbed temperature and velocity fields in the theory of the Benard effect[7] (the formation of so-called Benard cells).

We have thus shown under what conditions the analogy with the Benard problem can be used in the magnetohydrodynamics of an incompressible conductive liquid with finite viscosity and conductivity.

We are pleased to express our gratitude to A. M. Iskol'dskiĭ for interest in our work and for fruitful discussions, as well as to the Russian Fund for Fundamental Research for partial financial support (Project 97–02–16177).

[1] N. B. Volkov and A. M. Iskol'dskiĭ, JETP Lett. **51**, 634 (1990).
[2] A. M. Iskoldsky, N. B. Volkov, and N. M. Zubarev, Phys. Lett. A **217**, 330 (1996).
[3] A. M. Iskoldsky, N. B. Volkov, and O. V. Zubareva, Physica D **91**, 182 (1996).
[4] N. B. Volkov, N. M. Zubarev, O. V. Zubareva, and V. T. Shkatov, Pis'ma Zh. Tekh. Fiz. **22**(13), 43 (1996) [Tech. Phys. Lett. **22**, 538 (1996)].
[5] N. B. Volkov, N. M. Zubarev, O. V. Zubareva, and V. T. Shkatov, Physica D **109**, 315 (1997).
[6] L. D. Landau and E. M. Lifshitz, *Electrodynamics of Continuous Media* (Nauka, Moscow, 1982; Pergamon Press, Oxford, 1960).
[7] G. Z. Gershunin, E. M. Zhukhovitskiĭ, and A. A. Nepomnyashchiĭ, *Stability of Convective Currents*, (Nauka, Moscow, 1989).
[8] L. D. Landau and E. M. Lifshitz, *Fluid Mechanics* (Nauka, Moscow, 1986; Pergamon Press, Oxford, 1987).
[9] Rayleigh, Philos. Mag. **32**, 529 (1916).

Translated by W. J. Manthey

Resonance-tunnel-transit diode with coherent tunneling as an oscillator in the submillimeter range

É. A. Gel'vich, E. I. Golant, A. B. Pashkovskiĭ, and V. P. Sazonov

''Istok'' State Scientific Production Enterprise, Fryazino
(Submitted January 11, 1999)
Pis'ma Zh. Tekh. Fiz. **25**, 7–12 (May 26, 1999)

This paper presents an improved method for designing a resonance-tunnel-transit diode that makes it possible to substantially increase its negative dynamic resistance. © *1999 American Institute of Physics.* [S1063-7850(99)01805-4]

The great efforts made in recent years to create efficient generators of electromagnetic oscillations based on reliable semiconductor devices—Gunn diodes and avalanche-transit diodes in the millimeter range and quantum cascade lasers in the far-IR region—have left the submillimeter region virtually untouched. At the same time, a requirement for such oscillators exists and is constantly increasing. In particular, the spectral absorption lines of the molecules of many substances used in industry and scientific research lie in the submillimeter region.

There is in fact a semiconductor device that for a rather long time has aspired to the role of an active semiconductor element in the submillimeter range: the resonance-tunnel-transit diode (RTTD), which is a variety of the injection-transit diode in which the electrons are injected through a dual-barrier size-quantized resonance-tunnelling heterostructure (DBRTS). It has been experimentally shown that the active section of such diodes possesses negative dynamic conductivity up to frequencies of about 2.5 THz (Ref. 1), while operating as masers at a frequency of 712 GHz (Ref. 2). However, the resulting power levels were too small to be used in practice, and this experimental work was carried no further.

It should be pointed out that diode oscillators can be conventionally divided into two groups: parallel, in which the electromagnetic wave propagates parallel to the heteroboundaries of the semiconductor structure, as in lasers based on Fabry–Perot cavities in which the light is emitted through the side faces of the crystal, and series, as in oscillators based on avalanche transit-time diodes (ATDs) and Gunn diodes and in vertical-cavity surface-emission lasers (VCSELs),[3] in which the electromagnetic wave leaves the active section perpendicular to its heteroboundaries. The series layout has a number of substantial advantages over the parallel, but it has the disadvantage that passive ohmic sections are unavoidably present on the path of the electromagnetic wave, making the conditions for oscillation extremely rigorous: the negative resistance of the active section must be greater in absolute value than the total resistance of the passive layers, which, for a cross-sectional area of 10^{-6} cm^2, is on the order of a few ohms.[4] Thus, the key requirement on the interaction region for the series layout of the oscillator is that the negative resistance (per unit area) be greater than $10^{-6}(\Omega\ \mathrm{cm}^2)$.

Reference 4 drew attention to the possibility of using the resonant character of the frequency dependence of the active negative dynamic resistance (NDR) of the transit section of any injection-transit diode with delayed injection to substantially increase the NDR of the RTTD. The resonant character of this dependence appears when the reactive conductivity (inductive because of the delay of the injection) of the electric flux approaches the capacitive conductivity of the transit section. It is clear that the frequency corresponding to this resonance is determined by the ratio of the current and field amplitudes at the output of the DBRTS and by the lag angle of the current relative to the field and is an analog of the avalanche (characteristic) frequency of an ATD. Based on published data, the limiting oscillation frequency of an RTTD with the power level used in practice was estimated in Ref. 4 as 300–400 GHz.

An improved RTTD circuit was subsequently proposed that assumed that an additional hot-electron injector was used to introduce electrons with the necessary longitudinal energy onto one of the size-quantization levels of a dual-barrier structure, with the barriers being sufficiently transparent for the electrons to be coherently transported through the structure. It was theoretically shown that it is promising to use such a layout to create lasers with a Fabry–Perot cavity in the far IR (Ref. 5) and RTTD-based oscillators in the submillimeter wavelength region.[6] However, the NDR values of the RTTD calculated in Ref. 6 for a frequency of 2 THz were still too small for the output power to be of practical use. It should be pointed out that, despite the rigorous quantum-mechanical calculation of the conductivity of the RTTD in Ref. 6, the active resistance of the diode was calculated only approximately, on the assumption that the electronic component of the reactive conductivity is small by comparison with the capacitive conductivity of the diode. This approximation neglected the effect described in Ref. 4, in which the NDR of the RTTD increases close to its characteristic frequency, when the total reactive conductivity of the diode is close to zero. This paper uses an improved calculational method that is free of this drawback, making it possible to demonstrate that the NDR of an RTTD can be substantially increased in the submillimeter region.

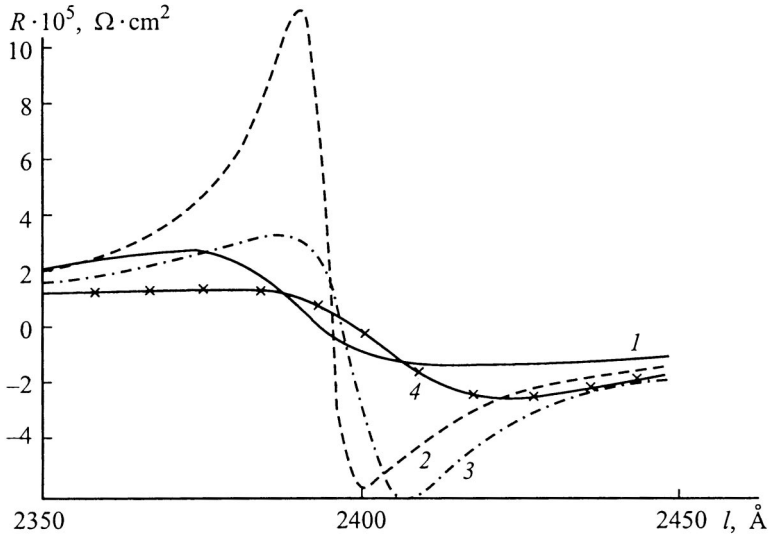

FIG. 1. Resistivity of an RTTD vs the length of the transit section at $T=77$ K. The relative injector height is $E_g/E_0=0.83$ (*1*), $E_g/E_0=0.84$ (*2*), $E_g/E_0=0.85$ (*3*), $E_g/E_0=0.83$ (*4*).

The calculation was done for diode structures with coherent electron transport, similar to those studied in Ref. 6. It is assumed that the electrons arrive at the DBRTS from a heteroinjector in which they have a Fermi distribution, density n, and temperature T. Reflection of the electrons from the heteroinjector boundaries is neglected.

Figure 1 shows the results of a calculation of the active resistance R of the RTTD at a frequency of $\nu=3$ THz vs the length of the transit section of a diode based on a GaAs/AlGaAs DBRTS with barrier heights of $\varphi_B=1.04$ eV, a thickness of $b=11$ Å, and a distance between the barriers of $a=65$ Å (the energy of the resonance level is $E_0\approx100$ meV) for $n=10^{18}$ cm^{-3} and $T=77$ K. The various curves correspond to various ratios of the heteroinjector height E_g to the energy E_0 of the resonance level. It can be seen that there are optimum values of this ratio [in this case, $E_g/E_0\approx0.84$–0.85, which provides a negative dynamic resistivity of the RTTD of $6\times10^{-5}(\Omega\cdot\text{cm}^2)$ when the transit sections are sufficiently short, ≈0.24 μm, assuming ballistic transport of the electrons].

In a quasi-classical RTTD the characteristic frequency of the diode strongly depends on the structural parameters, which determine the slope and the phase of the injection of the density-modulated electron flux into the transit section. A complete quantum calculation gives just as strong a dependence: it can be seen from Fig. 1 that a deviation of the injector height by a few millielectron volts from the optimum value reduces the NDR of the diode by a large factor. It can also be seen that the effect shows up in a very narrow region of lengths of the transit section, ~50 Å. It is interesting to note that a temperature increase of the crystal, whose influence was taken into account via the temperature dependence of the Fermi distribution of the electrons in the injector, increases the resonant value of the NDR. This can be clearly seen in Fig. 2, where, for the same frequency of 3 THz and a diode structure that differs only by a small change of the relative injector height, a negative resistance of $5\times10^{-4}(\Omega\,\text{cm}^2)$ is obtained at $T=300$ K, which is more typical of the centimeter region than of the submillimeter region.

A consistent quantum-mechanical calculation of the in-

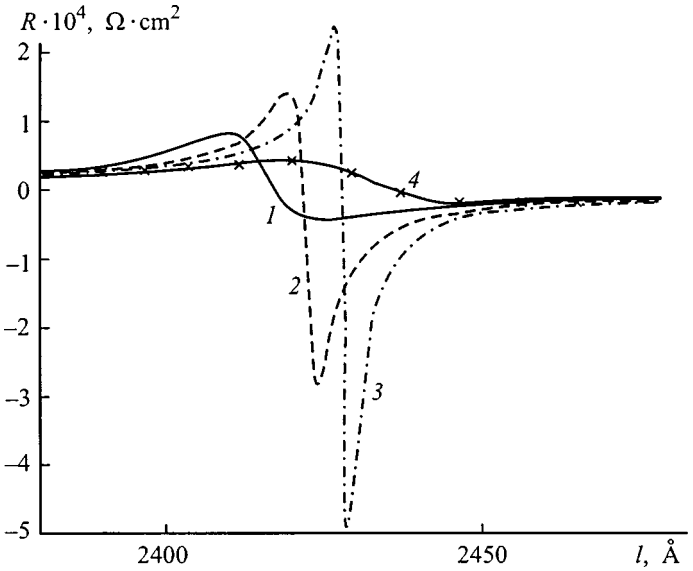

FIG. 2. Resistivity of an RTTD vs the length of the transit section at $T=300$ K. The relative injector height is $E_g/E_0=0.88$ (*1*), $E_g/E_0=0.90$ (*2*), $E_g/E_0=0.92$ (*3*), $E_g/E_0=0.94$ (*4*).

teraction of the electrons that coherently tunnel through the active region of an RTTD with a high-frequency electric field thus confirms the possibility of a resonant increase of the NDR of the diode close to its characteristic frequency, which, as shown by the calculation, can reach 3 THz ($\lambda = 0.1$ mm) during tunneling through the size-quantization ground state of a GaAs/AlGaAs DBRTS.

It should be pointed out that, because the NDR of the proposed (extremely specific) structure is strongly dependent on the parameters, the observation and use of this effect requires the structure to be very accurately fabricated.

However, this is quite feasible at the modern level of technology.

[1] T. C. L. G. Sollner, W. D. Goodhue, P. E. Tannewald, C. D. Parker, and D. D. Peck, Appl. Phys. Lett. **43**, 588 (1983).
[2] E. R. Brown, J. R. Soderstrom, C. D. Parker, L. J. Mahoney, K. M. Molvar, and T. C. McGill, Appl. Phys. Lett. **58**, 2291 (1991).
[3] S. Moneger, H. Qiang, F. H. Pollak, D. L. Mathin, R. Droopard, and G. N. Maracas, Solid-State Electron. **39**, 871 (1995).
[4] E. I. Golant and A. S. Tager, Élektron. Tekh. Ser. Élektron. Sverkh. Visok. Chast. No. 8(422), 19 (1989).
[5] E. I. Golant, A. B. Pashkovskiĭ, and A. S. Tager, Pis'ma Zh. Tekh. Fiz. **20**, No. 21, 74 (1994) [Tech. Phys. Lett. **20**, 886 (1994)].
[6] E. I. Golant and A. B. Pashkovskiĭ, Pis'ma Zh. Tekh. Fiz. **21**, No. 7, 16 (1995) [Tech. Phys. Lett. **21**, 246 (1995)].

Translated by W. J. Manthey

Photoinduced self-organization of gallium nanowires on a GaN surface

D. A. Bedarev, S. O. Kognovitskiĭ, and V. V. Lundin

A. F. Ioffe Physicotechnical Institute, Russian Academy of Sciences, St. Petersburg
(Submitted January 18, 1999)
Pis'ma Zh. Tekh. Fiz. **25**, 13–18 (May 26, 1999)

The mechanism of ultraviolet laser ablation of GaN epitaxial films is determined: it is found to be based on the dissociation of GaN molecules to form volatile nitrogen-containing components. The conditions of exposure under which the formation of gallium nanoclusters on the GaN surface are determined. Regimes of epitaxial growth of GaN are found in which parallel microterraces form on the surface of the samples. It is found that when samples with microterraces in the as-grown state are irradiated by high-power ultraviolet radiation, gallium nanowires are formed on the surface. It is proposed to use these phenomena to develop new UV optical lithographic techniques and to fabricate single-electron devices based on GaN. © *1999 American Institute of Physics.* [S1063-7850(99)01905-9]

The study of effects wherein the self-organization of nanostructures occurs on semiconductor surfaces is very important for modern optoelectronics and has already led to the creation of lasers utilizing quantum dots of III–V and II–VI compounds grown in a submonolayer growth regime.[1,2] The possibility of forming ordered structures of these materials on disoriented substrates can be utilized for efficient control of their optical-polarization and spectral properties.

A promising new material for making light-emitting devices for the short-wavelength part of the visible spectrum is GaN.[3] However, the self-organization processes leading to the necessary modification of the optical properties of the material have been insufficiently studied in GaN. In this paper we propose an efficient new method of forming ordered arrays of parallel gallium nanowires on a slightly corrugated GaN surface under excimer laser radiation.

The GaN epitaxial film samples were grown by MOCVD on sapphire substrates in the $(0001)\pm 30'$ orientation.[4] The growth processes were carried out in a horizontal reactor, in a hydrogen flow at reduced pressure (200 mbar). Ammonia and trimethyl gallium were used as sources. Magnesium-doped films were obtained with the use of magnesium bicylopentadienyl.

The epitaxial process included the deposition of a GaN buffer layer at a reduced temperature ($\sim 500\,^{\circ}$C) and annealing of the buffer layer and the subsequent epitaxial growth of the main layer or multilayer structure at a high temperature (~ 1000–$1040\,^{\circ}$C). During the epitaxial growth the flow of trimethyl gallium was 36 μmole/min, which corresponded to an epitaxial growth rate of 2.6–2.8 μm/h.

The undoped epitaxial films grown at an epitaxial growth temperature of $1040\,^{\circ}$C had atomically smooth surfaces with not more than 1 nm of nonplanarity, according to atomic-force microscope (AFM) data; this attests to the two-dimensional character of the epitaxial growth. A similar morphology of the layers was observed for magnesium-doped films with magnesium concentrations $N_{[\mathrm{Mg}]}$ of 4×10^{19} cm^{-3} or less. As the doping level was raised or the epitaxial growth temperature was lowered the nonplanarity of the surface increased significantly, even to such an extent that mac-

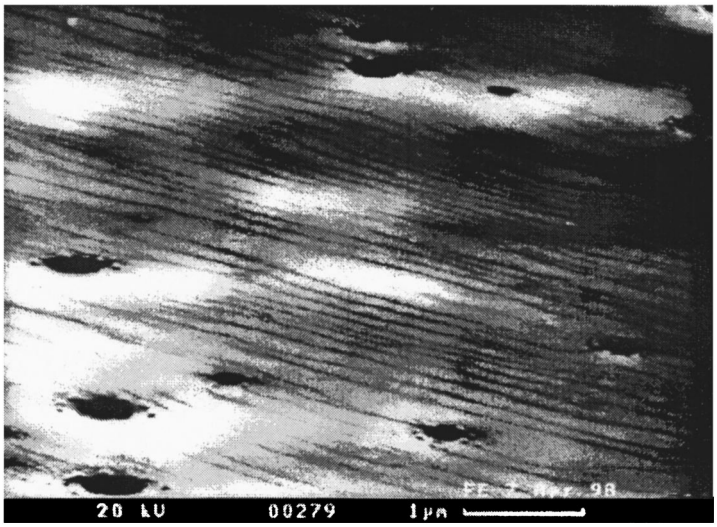

FIG. 1. Scanning electron micrograph of the surface of a GaN sample with quasiperiodic microterraces.

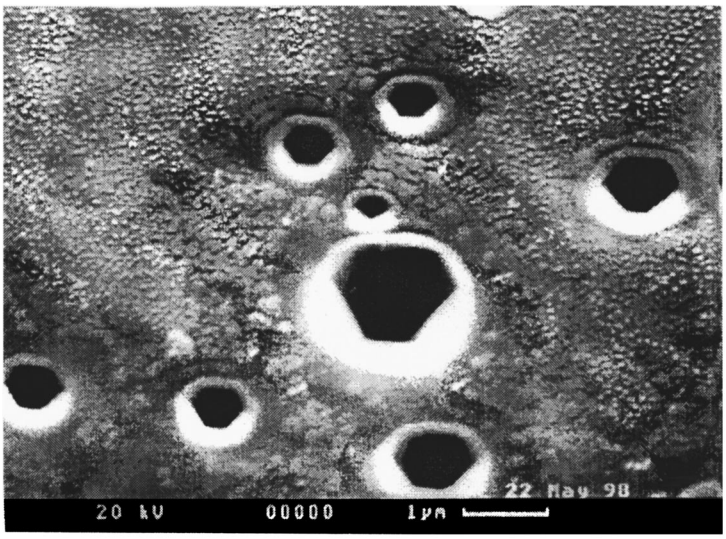

FIG. 2. Scanning electron micrograph of a planar GaN surface after excimer laser irradiation.

roscopic terraces with heights of the order of 100 nm were formed.

Under certain intermediate conditions of growth, in a narrow range of parameters, we observed the formation of a quasiperiodic array of parallel microscopic growth steps on the surface of the resulting samples (Fig. 1). A single direction of the steps was maintained over an area of up to 5 mm in diameter. According to AFM images, the average repetition period of the steps was around 200 nm, and the height of the steps was 6 nm.

The GaN samples obtained, some of which were grown with a slightly corrugated surface, were irradiated in air by 248 nm radiation from an excimer laser. A single pulse with a duration of 10 ns and an energy of around 80 mJ was used for the exposure. The intensity distribution over the cross section of the focused laser beam was close to Gaussian.

The investigation revealed a characteristic and specific redistribution of the photoablation products of GaN. Irradiation by intense UV light causes dissociation of GaN molecules, with the nitrogen passing into the gas phase and the metallic gallium settling on the surface of the sample. This causes substantial changes in the optical properties of the surface, e.g., the reflection takes on a metallic character. This peculiarity of the ablation of GaN can be exploited in UV optical lithography.

After laser exposure the central part of the irradiated region on the surface of the sample, where the energy density reached 2.1 J/cm^2, was covered by a continuous gallium film, while no modification of the morphology of the surface was observed at the edges of the irradiated region.

For excitation corresponding to a narrow range of intermediate energy densities, estimated with allowance for the spatial distribution of the intensity of the laser beam, we observed the formation of an array of isolated gallium clusters.

On samples with a uniform planar surface the clusters formed were plane clusters about 70 nm in diameter. These clusters were distributed chaotically over the surface (the region in the upper part of Fig. 2).

Randomly distributed gallium clusters up to 25 μm in diameter were previously observed on a GaAs surface during epitaxial growth with an As deficit.[5] Chaotically distributed ''magic'' clusters 1–2 nm in size and with a definite number of Ga atoms in a cluster have recently been produced on the Si (111) surface.[6]

The use of the new GaN samples with growth microterraces disrupting the uniformity of the surface permitted the formation, by the indicated laser irradiation, of gallium clusters predominantly joined into a quasiperiodic system of parallel metallic wires (Fig. 3). These wires were localized along the growth steps, apparently because of the higher rate of photoablation and the redistribution of the surface tension in the vicinity of the steps. The cross-sectional diameter of the wires was around 50 nm.

In summary, on the GaN surface we have for the first time created a self-organizing system of oriented metallic nanowires with a small repetition period; these wires comprise a unique object for investigating the plasmon–polariton interaction in quasi-one-dimensional structures. In addition, such a system of metallic wires might play the role of a built-in polarizer for GaN-based light-emitting devices and might also be used as a semitransparent contact to provide a more uniform distribution of injected carriers along the surface of a sample.

The authors are grateful to R. P. Seĭsyan and N. S. Averkiev for showing interest in this study, to V. M. Bursov

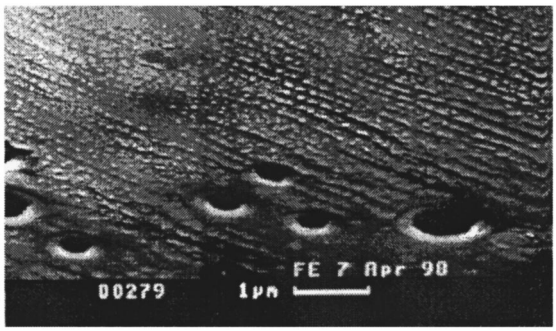

FIG. 3. Scanning electron micrograph of a GaN surface with gallium wires.

for providing us the means to investigate the morphology of the sample surfaces under a high-resolution scanning electron microscope, and to A. K. Kryzhanovskiĭ for investigating the morphology of the sample surfaces with an atomic-force microscope.

[1] N. N. Ledentsov, V. A. Schukin, M. Grundmann, N. Kirstaedter, J. Bohrer, O. Schmidt, D. Bimberg, V. M. Ustinov, A. Yu. Egorov, A. E. Zhukov, P. S. Kop'ev, S. V. Zaitsev, Zh. I. Alferov, A. I. Borovkov, A. O. Kosogov, S. S. Ruvimov, P. Werner, and U. Gosele, Phys. Rev. B **54**, 8743 (1996).

[2] S. V. Ivanov, A. A. Toropov, T. V. Shubina, S. V. Sorokin, A. V. Lebedev, I. V. Sedova, P. S. Kop'ev, G. R. Pozina, J. P. Bergman, and B. Monemar, J. Appl. Phys. **83**, 3168 (1998).

[3] I. Akasaki and H. Amano, Jpn. J. Appl. Phys. **36**, 5393 (1997).

[4] W. V. Lundin, A. S. Usikov *et al.*, ''Optical and electrical properties III–N structures grown by MOCVD on sapphire substrates,'' *EW MOVPE VII*, Berlin, June 8–11, 1997, Workshop Booklet, F10.

[5] T. D. Lowes and M. Zinke-Allmang, J. Appl. Phys. **73**, 4937 (1993).

[6] M. Y. Lai and Y. L. Wang, Phys. Rev. Lett. **81**, 164 (1998).

Translated by Steve Torstveit

Experimental study of the transient process in a pulsed relativistic backward-wave tube for the millimeter range

M. I. Yalandin, V. G. Shpak, S. A. Shunaĭlov, and M. R. Ul'maskulov

Institute of Electrophysics, Urals Branch of the Russian Academy of Sciences, Ekaterinburg
(Submitted July 14, 1998; resubmitted January 14, 1999)
Pis'ma Zh. Tekh. Fiz. **25**, 19–23 (May 26, 1999)

The influence of the rise time of the current pulse of a nanosecond high-current electron beam on the self-oscillation regime that is established in a relativistic backward-wave tube for the 38 GHz range is investigated experimentally. It is shown that a peak power of more than 50 MW is attained in a time of ~300 ps. © *1999 American Institute of Physics.* [S1063-7850(99)02005-4]

The nature of the transient process in a relativistic backward-wave tube (BWT) depends on the amount by which the working current of the oscillator exceeds the starting current and on the power level of the initial microwave signal in the synchronism band of the device. This signal is the spectral component of the radiation of the front of a dense electron beam injected into the slow-wave system.[1] At present there is heightened interest in the study of the fine structure of the transient process in connection with the fact that, according to Refs. 1 and 2, a relativistic BWT can, even over times of the order of $t \sim L/v_g$, generate a short burst of microwave radiation with a power level higher than in the steady state. Here L is the length of the slow-wave system and v_g is the group velocity of the wave in the interaction space. For a BWT at 38 GHz and a beam density of ~200 keV the characteristic value (L/v_g) is some hundreds of picoseconds. The study of the relaxation to steady-state generation in a device of this kind[3] has become possible with the construction of a high-current electron accelerator[4] (~250 keV, ~2 kA, 5 ns) with stable characteristics and a continuously adjustable rise time of the accelerating voltage pulse (0.3–1.5 ns). A hot-carrier germanium microwave detector and a beam current sensor, with time resolutions of 150 and 200 ps, respectively, were developed for such studies.

The slow-wave systems of the BWT were circular waveguides with a sinusoidal corrugation of the wall. One end of the slow-wave system was connected to an electron vacuum diode with a cold cathode, and the other end was connected to a beam collector and a horn antenna for output. The vacuum diode was isolated from the slow-wave system by a circular cutoff waveguide. An annular beam with a diameter of 5.5 mm and a wall thickness of 0.4 mm was confined by the axial magnetic field of a pulsed solenoid with an induction of 5 T. The first backward spatial harmonic of the E_{01} mode was synchronous with the beam. It has been shown[5] by numerical calculations and experiments that at subnanosecond rise times of the accelerating voltage, the longitudinal crossover is formed at the entrance to the drift chamber (the slow-wave system), 1.5–2 cm away from the explosive-emission cathode. The rise time of the current pulse of an electron bunch in this region is shorter than that of the accelerating voltage. This is because of dynamic bunching of the electrons starting from the cathode as the voltage rises with time. Additional sharpening of the nanosecond front of the accelerating voltage should lead to a substantial increase in the level of the initial microwave signal in the synchronism band of the BWT. The implementation of such a regime was the main goal of the present experiments.

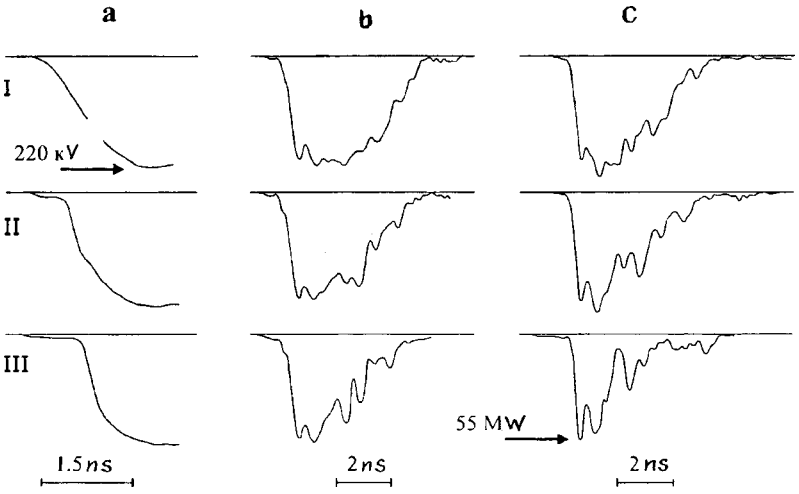

FIG. 1. Variation of the shape of the microwave radiation pulse from a BWT with slow-wave systems of length 60 and 100 mm (b and c, respectively) as the accelerating voltage pulse applied to the cathode (a) is successively sharpened.

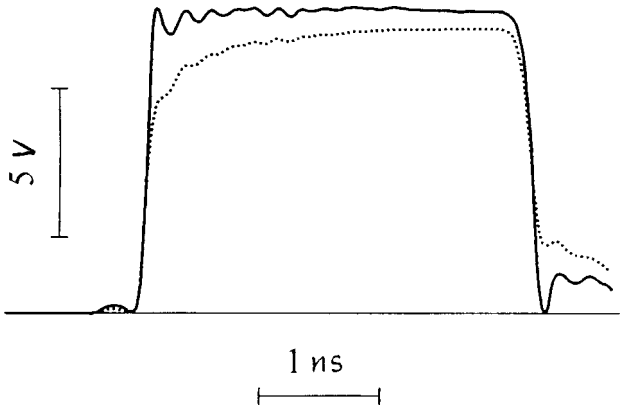

FIG. 2. Distortion of a 3.5-ns calibration pulse with a rise time of 70 ps (solid curve) after passage through a 50-ns cable delay line (dotted line).

Figure 1a shows the character of the change in shape of the front of the accelerating pulse as the gap was varied in a high-pressure (50 atm) nitrogen-filled peaking spark gap at the output of the 5-ns high-voltage modulator of the accelerator. The corresponding change in the shape of the signal of the microwave detector recording the radiation of the BWT is shown in Fig. 1b and 1c. The series of oscilloscope traces in Fig. 1c were obtained with a 1.7 times longer slow-wave system than for the series in Fig. 1b. Thus the starting currents for these two versions of the BWT differed by about a factor of 5 ($I_{st} \sim L^{-3}$); for the short slow-wave system (Fig. 1b) it had the value $I_{st1} \approx 0.4$ kA. The working beam current was $I_{op} \approx 1.6$ kA for both experiments (Fig. 1b and 1c). One can see from curve I in Fig. 1b that when the working current is 4 times higher than the starting current a slight modulation of the microwave signal is observed even without additional sharpening of the front of the beam current. Sharpening increases the modulation (curve III in Fig. 1b), and in the case of the long slow-wave system ($I_{op}/I_{st2} \approx 20$) a beam current pulse with a sharp front leads to a pronounced stochastization of the generation, with a power modulation index close to 100% (curve III in Fig. 1c). In the last case one notices a shortening in the duration of the generation. It should be noted that the shape of the microwave pulses in Fig. 1 is well reproduced from pulse to pulse.

For recording the amplitude and time characteristics of the microwave radiation pulses with subnanosecond resolution it was necessary to correct the results of the measurements for the finite pass band of the detection system. Since the S7-19 oscilloscope used in the experiment has an adequate bandwidth (5 GHz), the main problem was due to the delay lines and connecting cables. These elements were calibrated by a test pulse with a duration of 3.5 ns and a rise time of 70 ps (Fig. 2), which was recorded by a Techtronix TDS820 stroboscopic oscilloscope with a bandwidth of 6 GHz. For calibration we used even shorter pulses, with durations at half maximum of from 190 to 550 ps and rise times of 90–300 ps. Analysis of the oscillograms obtained in the experiment and the channel calibration data showed that the rise times of the microwave radiation pulses varied from 500 ps (curve I in Fig. 1b) to 200 ps (curve III in Fig. 1c). For both lengths of the slow-wave system we observed an increase in the growth rate of the microwave power as the beam front was sharpened (I→ II→ III). The maximum value attained was 300 MW/ns (curve III in Fig. 1c). When the impulse characteristic of the detection channel (Fig. 2) is taken into account, one finds, for example, that the amplitude of the first spike of microwave power (curve III in Fig. 1c) is at least 10% higher than that of the next spike. Furthermore, limiting the frequency characteristic leads to a certain smoothing of the modulation of the microwave signal and to a 10–15% broadening of the spikes at durations of 500–300 ps. When the necessary amplitude corrections are taken into account, one can estimate that the power of the first subnanosecond spike under these conditions is 50–55 MW.

The possible influence of reflections from the collector end of the slow-wave system on the irregularity of the microwave signals at times $t \geqslant L/v_g$ was investigated in a special series of experiments. For this we used a procedure wherein a preliminarily sharpened 5-ns accelerating voltage pulse (curve III in Fig. 1a) is shortened to ~ 1 ns by means of a cutoff spark gap. In this case the duration of the beam current pulse was sufficient for generating only the first spike of microwave radiation, with a duration of 300–500 ps at the same power. If the corrugation of the slow-wave system is abruptly discontinued, a short microwave pulse gives rise to a sequence of reflections with a fixed delay of $2L/v_g$ (Ref. 6). In the present experiments we used slow-wave systems in which the amplitude of the last four periods of the corrugation was gradually decreased. As a result, the corrugated waveguide made a smooth transition to the circular output waveguide, the level of reflections was less than 5%, and they caused only a slight distortion of the recorded oscillograms.

In summary, in this paper we have confirmed the importance of the current rise parameter dI/dt of the high-current beam for varying the self-oscillatory mode of the millimeter-wave BWT and the attainment of peak powers of tens of megawatts in a picosecond interval. In this connection it appears promising to persue the idea[7] of making an oscillator with an even higher rate of rise of the microwave power through the use of an accelerating voltage pulse synthesized on the principle of having a short spike on the front, followed by a quasiplanar section.

This study was supported by the Russian Fund for Fundamental Research, Grant 98-02-17308.

[1] N. S. Ginzburg *et al.*, Izv. Vyssh. Uchebn. Zaved. Radiofiz. **21**, 137 (1978).
[2] N. S. Ginzburg *et al.*, Pis'ma Zh. Tekh. Fiz. **22**(9), 39 (1996) [Tech. Phys. Lett. **22**(5), 359 (1996)].
[3] N. M. Bykov *et al.*, Pis'ma Zh. Tekh. Fiz. **11**, 541 (1985) [Sov. Tech. Phys. Lett. **11**, 225 (1985)].
[4] V. G. Shpak *et al.*, *Proceedings of BEAMS'96 — Eleventh International Conference on High Power Particle Beams*, Prague, Czech Republic (1996), pp. 913–916.
[5] V. G. Shpak *et al.*, Pis'ma Zh. Tekh. Fiz. **22**(7), 65 (1996) [Tech. Phys. Lett. **22**(4), 297 (1996)].
[6] N. S. Ginzburg *et al.*, Nucl. Instrum. Methods Phys. Res. A **393**, 352 (1997).
[7] V. G. Shpak *et al.*, *Proceedings of the Eleventh IEEE International Pulsed Power Conference*, Baltimore, MD, USA (1997), pp. 1581–1585.

Translated by Steve Torstveit

Quantitative analysis of endohedral metallofullerenes by Rutherford backscattering of protons

E. G. Alekseev, Yu. S. Grushko, V. S. Kozlov, and V. M. Lebedev

B. P. Konstantinov St. Petersburg Institute of Nuclear Physics, Russian Academy of Sciences, St. Petersburg
(Submitted November 4, 1998)
Pis'ma Zh. Tekh. Fiz. **25**, 24–30 (May 26, 1999)

Samples containing endohedral metallofullerenes of gadolinium ($Gd@C_{82}$) and dysprosium ($Dy@C_{82}$) are investigated by the Rutherford backscattering of protons. It is shown that the concentration of endohedral metallofullerenes can be determined to within a few percent. The measured concentration of endohedral metallofullerenes $Gd@C_{82}$ and $Dy@C_{82}$ in samples prepared by selective multistep extraction is $\sim 60\%$. © *1999 American Institute of Physics.* [S1063-7850(99)02105-9]

Endohedral metallofullerenes are ordinarily analyzed by secondary-ion mass spectrometry, using various means of desorption of the sample to be investigated. However, this method gives only qualitative results as to the concentrations of metallofullerenes in the fullerene mixture, since the conditions for the molecules to pass into the gas phase are substantially different.[1,2]

For a quantitative determination of the concentrations of endohedral metallofullerenes doped with rare-earth elements, specifically, $Gd@C_{82}$ and $Dy@C_{82}$, in a fullerene mixture, we have employed the Rutherford backscattering of protons.[3,4] Since this method gives only the elemental composition and not the form of the chemical compound, the presence of specifically endohedral metallofullerenes in a mixture is determined by methods used for separating them from the fullerene mixture and by mass spectrometric measurements.[1,2]

This study was carried out on an analytical unit for materials research, built around the electrostatic accelerator at the B. P. Konstantinov St. Petersburg Institute of Nuclear Physics, Russian Academy of Sciences.[5]

In the backscattering method one investigates how the intensity of protons scattered into the reverse hemisphere depends on their energy at a constant energy of the incoming particles. For a massive sample one observes steps in the continuous experimental spectrum, at energies corresponding to the scattering of particles on surface atoms of the target (Fig. 1a). The number of steps observed is equal to the number of different kinds of atoms in the sample.

Starting from the laws of energy and momentum conservation in binary collisions, one obtains a unique relation between the initial energy E_0 of the proton (of mass m) and its energy E_i after an elastic collision with a target atom of mass M_i:

$$E_i = K_i E_0 = E_0 \cdot \{m \cdot \cos\theta + (M_i^2 - m^2 \cdot \sin^2\theta)^{1/2}/(m + M_i)\}^2, \quad (1)$$

where K_i is a kinematic factor and θ is the scattering angle. The elemental composition of the sample is determined from measurements of $K_i \cdot E_0$. At a scattering angle $\theta = 135°$ the kinematic factor of carbon is $K_C = 0.752$ and that of the rare-earth elements is $K \approx 0.98$, i.e., one can easily distinguish the contributions from scattering on these atoms in the measured spectrum (Fig. 1a).

In the analysis of the experimental spectra obtained for samples with a constant composition over the thickness, one uses the subtraction (or step) method. This method is based on the assumption that the scattering of the ions on atoms of each species occurs independently. The plateaus in the spectrum near the steps are approximated by straight lines, whose positions on the individual parts of the spectra are found by the least squares method.

The atomic ratio C_i/C_j in a sample under analysis is calculated from the step heights H_i and H_j for these elements in the experimental spectrum:

$$C_i/C_j = (H_i/H_j) \cdot (\sigma_i/\sigma_j) \cdot ([S]_j/[S]_i), \quad (2)$$

where σ is the scattering cross section and $[S]$ is an energy-loss parameter.[4] The factor $([S]_j/[S]_i)$ takes into account the difference of the energy losses for the protons emerging from the target after scattering on the different kinds of atoms; for the pair carbon/gadolinium one has $[S]_C/[S]_{Gd} \cong 1.01$ (Ref. 6).

The differential scattering cross section for ions with charge z on atoms with charge Z_i is calculated from the Rutherford formula:[3]

$$d\sigma/d\Omega = (z \cdot Z_i \cdot e^2/2 \cdot E_0 \cdot \sin^2\theta)^2 \times \{\cos\theta + [1 - (m \cdot \sin\theta/M_i)^2]^{1/2}\}^2 / [1 - (m \cdot \sin\theta/M_i)^2]^{1/2}, \quad (3)$$

where $d\Omega = 2\pi\theta d\theta$ is an element of solid angle.

The fact that the scattering cross section depends on the square of the charge of the scattering atom gives this method a high sensitivity to elements with a large atomic number in a host material consisting mainly of elements of small atomic number. This circumstance makes it possible to determine the concentration of a rare-earth element in carbon at a level of 0.01%. In a number of cases, however, it is necessary to take into account the deviation of the scattering cross section from that calculated by the Rutherford formula. Below the Coulomb barrier the scattering cross section is decreased on

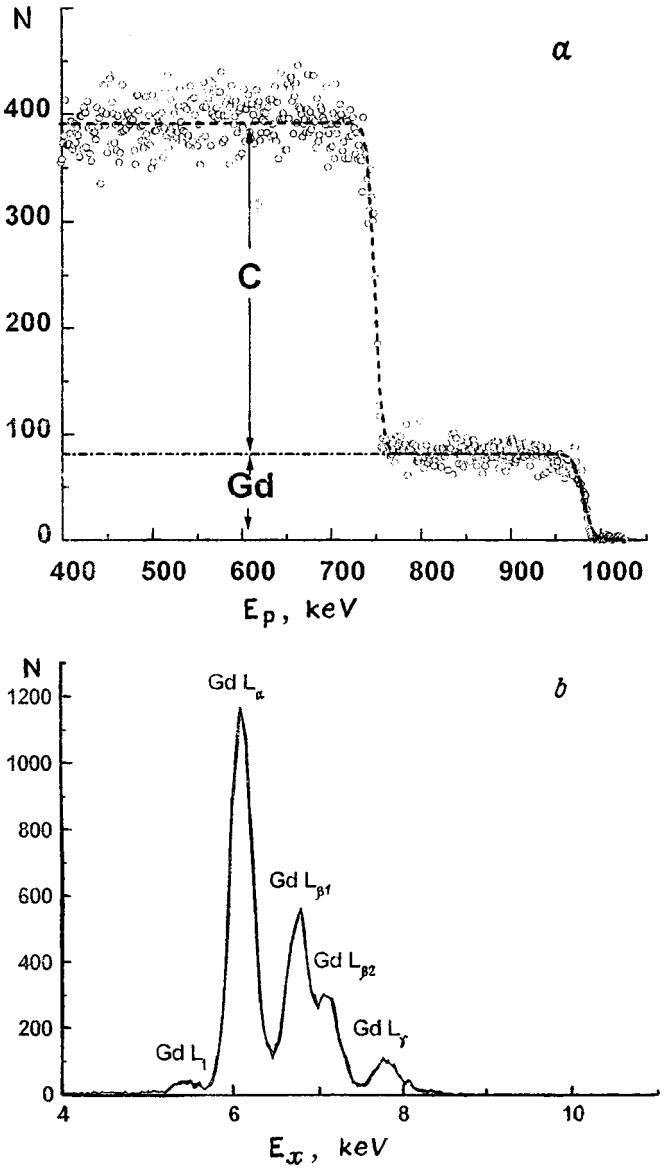

FIG. 1. Experimental spectra for a sample containing Gd@C_{82}: a — the spectrum of protons scattered at an angle $\theta=135°$ for an initial proton energy $E_p=1$ MeV; b — the spectrum of the characteristic x-ray emission excited by the protons. The thickness of the carbon absorber at the Si(Li) x-ray detector was 80 mg/cm^2. The atomic ratio Gd/C$=(6.5\pm0.3)\times10^{-3}$.

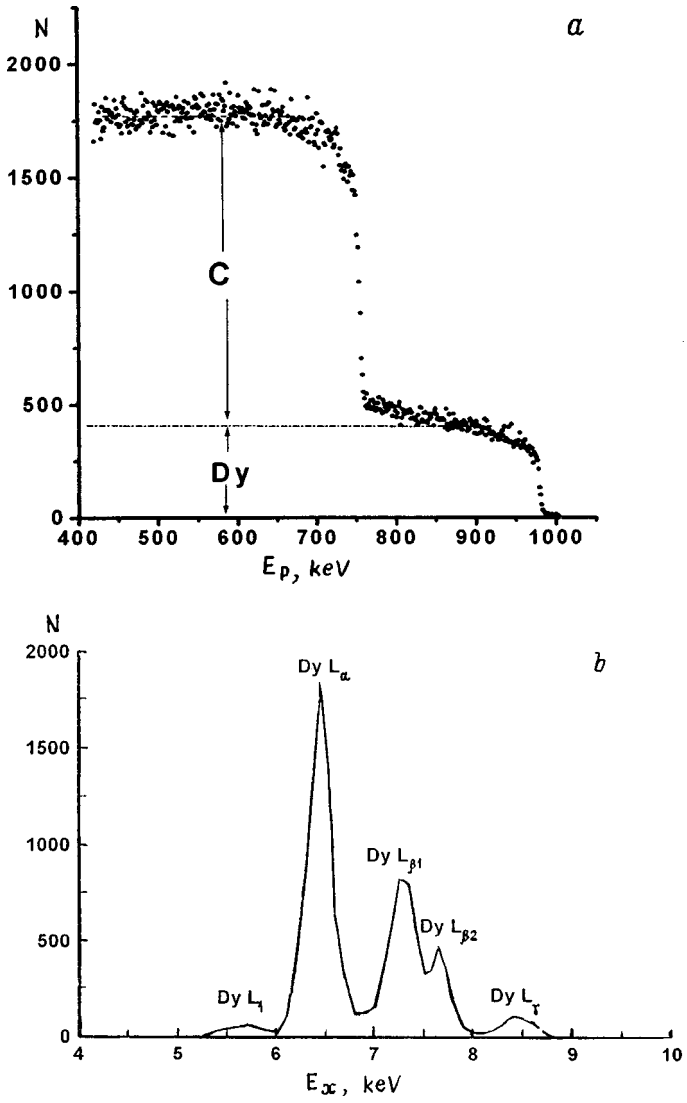

FIG. 2. The experimental spectra for a sample containing Dy@C_{82}: a — the spectrum of protons scattered at an angle $\theta=135°$ for an initial proton energy $E_p=1$ MeV; b — the spectrum of the characteristic x-ray emission excited by the protons. The thickness of the carbon absorber at the Si(Li) x-ray detector was 80 mg/cm^2. The atomic ratio Dy/C$=(7.3\pm0.3)\times10^{-3}$.

account of the screening of the electric field of the target nucleus by the atomic electrons. The presence of the nuclear potential and resonance scattering also complicates the calculation of the cross sections for light atoms; they can change by a factor of some tens of times, especially for elements with a small atomic number.[3]

We therefore measured the scattering cross section for carbon experimentally. For this purpose we prepared model samples containing carbon and gadolinium with an atomic ratio Gd/C from 0.05 to 0.001. We chose a proton energy $E_0=1$ MeV and a scattering angle $\theta=135°$, since under these conditions the scattering cross section on carbon varies smoothly with energy.[3] The measurements showed that the scattering cross section on carbon is increased by a factor of 3.06 ± 0.03 in comparison with the purely Rutherford cross section, on account of the nuclear scattering contribution. The differential scattering cross sections of protons under these experimental conditions ($E_p=1$ MeV, $\theta=135°$) are as follows: 0.194×10^{-24} cm^2/sr for carbon, 7.28×10^{-24} cm^2/sr for gadolinium, and 7.76×10^{-24} cm^2/sr for dysprosium.

This method was used for real-time elemental analysis of endohedral metallofullerenes of gadolinium and dysprosium during their enrichment and extraction from a fullerene mixture by the methods of selective multistep extraction.[2] Samples of soot, a cathode deposit, and a mixture of fullerenes in the form of a solution or suspension were placed in an aluminum cup, dessicated, and then used for accelerator experiments. A sample of 0.005 g of material, uniformly deposited on a substrate, was sufficient for determination of the elemental composition.

The samples were irradiated by protons with energy $E_p=1$ MeV at an ion beam current of 50 to 100 nA. The scattered protons were detected by a planar silicon spectrometer

positioned at an angle $\theta = 135°$ to the beam direction. The time of study for each sample was ~15 min. Since the backscattering method does not have sufficient mass resolution in the region of the rare-earth elements (the kinematic factors for gadolinium and dysprosium are practically equal, $K_{Cd} \approx K_{Dy} = 0.979$), they were identified from the characteristic x-ray emission excited by the protons in the same experiment.

Figure 1 shows the Rutherford backscattering spectrum of the protons (Fig. 1a) and the spectrum of the characteristic x radiation (Fig. 1b), obtained for a sample enriched by the selective extraction of the gadolinium endohedral metallofullerene $Gd@C_{82}$. The spectrum in Fig. 1a clearly exhibits the steps corresponding to scattering on carbon and gadolinium. The atomic ratio $Gd/C = (6.5 \pm 0.3) \times 10^{-3}$. As is shown by a mass spectrometric analysis, the gadolinium in the sample is found in the form of an endohedral metallofullerene $Gd@C_{82}$ (Refs. 1 and 2). Consequently, the mass content of $Gd@C_{82}$ in the target is ~57%.

For a sample containing the dysprosium endohedral metallofullerene (Fig. 2a,b), the atomic ratio $Dy/C = (7.3 \pm 0.3) \times 10^{-3}$, and the mass content of $Dy@C_{82}$ in it is ~63%.

Thus the Rutherford backscattering method can be used for a quantitative determination of the concentration of endohedral metallofullerenes to an accuracy of a few percent in samples as small as 0.005 g of material.

This study was carried out under Project No. 98066 ''Tracer'' under the auspices of the Russian Science and Engineering Progam ''Fullerenes and Atomic Clusters.''

[1] V. I. Karataev, Pis'ma Zh. Tekh. Fiz. **24**(5), 1 (1998) [Tech. Phys. Lett. **24**(3), 167 (1998)].
[2] E. G. Alekseev, V. I. Karataev, V. S. Kozlov *et al.*, *Abstracts of Invited Lectures and Contributed Papers of the Third International Workshop ''Fullerenes and Atomic Clusters,''* St. Petersburg, Russia, June 30–July 4, 1997, p. 21.
[3] J. W. Mayer and E. Rimini, *Ion Beam Handbook for Material Analysis*, Academic Press, New York (1977), 488 pp.
[4] W. K. Chu, J. W. Mayer, and M. A. Nicolet, *Backcsattering Spectrometry*, Academic Press, New York (1978), 376 pp.
[5] V. M. Lebedev, V. A. Smolin, and B. B. Tokarev, PNPI Research Report 1994–1995, pp. 292–297.
[6] J. E. Ziegler, J. P. Biersack, and U. Littmark, *The Stopping and Range of Ions in Solids*, Pergamon Press (1985), 300 pp.

Translated by Steve Torstveit

Photoluminescence properties of erbium-doped single-crystal and porous silicon films

L. K. Orlov, S. V. Ivin, D. V. Shengurov, and É. A. Shteĭnman

Physicotechnical Research Institute at the N. I. Lobachevski State University, Nizhniĭ Novgorod; Institute of Solid State Physics, Russian Academy of Sciences, Chernogolovka

(Submitted July 1, 1998)
Pis'ma Zh. Tekh. Fiz. **25**, 31–34 (May 26, 1999)

The features of the photoluminescence spectra of single-crystal and porous Si:Er films grown by molecular beam epitaxy are discussed. © *1999 American Institute of Physics.* [S1063-7850(99)02205-3]

The problem of optical transitions in erbium atoms imbedded by various methods in a silicon host has been actively discussed in the literature in recent years in connection with applications in optoelectronics. Detailed studies have been done on the properties of silicon doped with erbium either directly during epitaxial growth[1,2] or by ion implantation and diffusion methods.[3] To improve the emission efficiency of erbium it has been proposed to use porous silicon[4] into which erbium is introduced from solution during the electrochemical etching. In that case, however, the erbium most likely would remain either on the surface of the pores, forming light-emitting complexes radiating at a wavelength of 1.54 μm, or would diffuse into the subsurface layers of oxidized silicon. The emission efficiency of the Er complexes in that case would be increased on account of the greater surface area, but the emission mechanism would remain the conventional one for Er. For this reason it would be hard to expect that the photoluminescence efficiency of erbium in porous silicon could compare with that in ordinary glasses. However, the role of bulk effects in porous silicon remains unclear; in particular, whether the electronic structure of porous silicon would increase the efficiency of radiative transitions of Er in silicon.

In the present study we have undertaken to answer this last question by comparing the photoluminescence spectra of epitaxial silicon films and erbium-doped films prepared from them. For growing the erbium-doped autoepitaxial silicon structures we used molecular beam epitaxy (MBE) of silicon in sublimating solid-phase sources.[5] The sources of the fluxes of silicon and erbium atoms in the reactor of the apparatus were high-resistance rods of silicon doped with erbium directly during their growth by the floating zone method. This method of growing the erbium-doped silicon epitaxial films was proposed and implemented here for the first time. Mass spectrometric studies of the erbium distribution in the source showed that it has a gradient distribution along the length of the source in a concentration range $N_{\mathrm{Er}} \sim 10^{17}-10^{20}$ cm^{-3}.

Single-crystal films of erbium-doped silicon up to 2.0 μm thick were grown by this epitaxial method at a growth temperature $T_p \approx 600\,^{\circ}$C. The concentration of oxygen atoms in the silicon epitaxial films was set by the residual gas pressure in the reactor, which was at a level of $\sim 1\times 10^{-6}$ torr. The structure of the surface of the epitaxial film in this case had an orange-peel look, and a metallographic analysis revealed the presence of inclined dislocations (up to 6×10^{6} cm^{-2}) growing from the substrate toward the surface. This fact attests to the efficient incorporation of the erbium atoms in the growing film (the erbium concentration in the film, according to a mass spectrometric analysis, reached $\sim 1\times 10^{19}$ cm^{-3}). The presence of erbium in the samples was also confirmed by measurements of the profile of the structure by the CV and Hall-effect methods. In general, erbium atoms in Si can impart *n*- or *p*-type conductivity, the concentration of electrically active states in the system being a few percent of the total number of erbium atoms in the film. As we have said, the initial Si:Er source had *p*-type

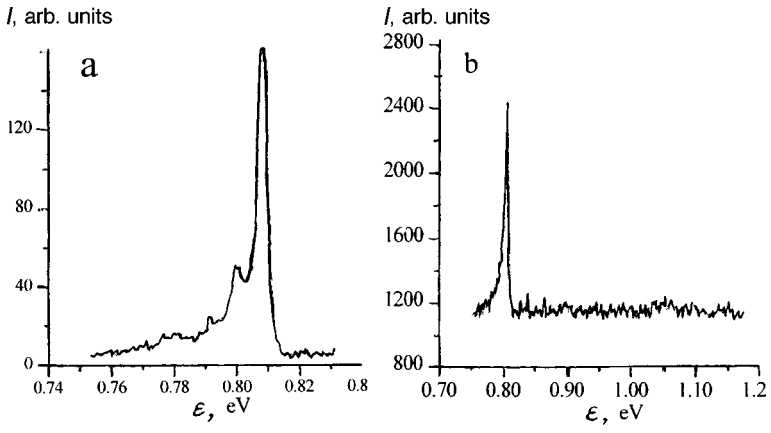

FIG. 1. Photoluminescence spectra of two single-crystal samples of Si:Er.

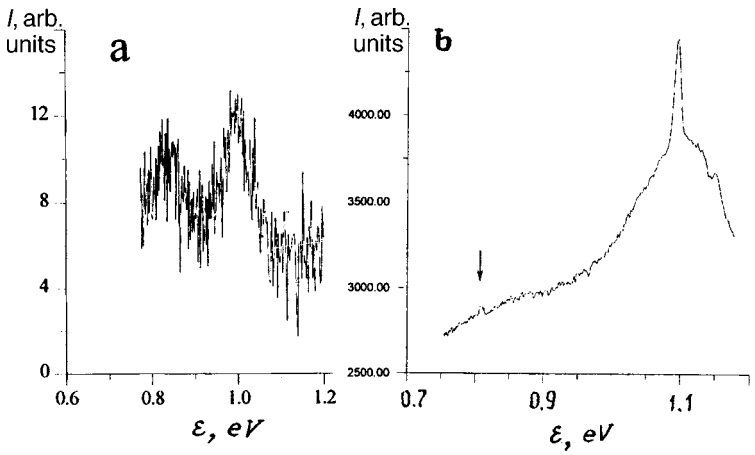

FIG. 2. Photoluminescence spectrum of the corresponding samples of porous Si:Er.

conductivity and was a rather high-resistance material ($p<10^{14}$ cm^{-3}).

A typical photoluminescence spectrum taken at $T=4.2$ K on two of the samples grown is shown in Fig. 1. It is seen that the rather efficient radiative recombination via states of the erbium atoms (the line at wavelength 1.54 μm) almost completely suppressed the radiative transitions D_1 and D_2 at dislocation pileups in the film.

Electrochemical etching of the grown Si:Er epitaxial structures produced films of porous silicon in which, unlike those studied in Ref. 4, the erbium atoms were located not on the surface of the pores but in the bulk of single-crystal grains. Figure 2 shows their photoluminescence spectra. It is seen that after the electrochemical etching, the role of erbium in the radiative recombination was sharply diminished: the intensity of the line at wavelength 1.54 μm was greatly weakened, while at the same time the efficiency of radiative recombination involving an optical phonon increased. This effect may be due to the circumstance that etching of the sample occurs mainly along the inclined dislocations growing from the substrate toward the surface, and it is likely that the maximum concentration of both erbium and oxygen occurs around these dislocations. The etching away of these regions in the formation of the porous structure substantially decreases the erbium concentration in the remaining part of the silicon matrix, and electronic, particularly low-dimensional, effects do not compensate for this decrease, nor do they lead to any noticeable features.

This study was supported by the Government Science and Engineering Program ''Physics of Solid-State Nanostructures'' (Grant 97-2023).

The authors are also grateful to M. G. Mil'vidskiĭ and N. A. Sobolev for coming up with the problem and seeing it through, and to Yu. A. Karpov for preparing the Si:Er sources.

[1] J. Stimmer, A. Reittinger, J. F. Nutzel, G. Abstreiter, H. Holzbbrecher, C. Buchal, Appl. Phys. Lett. **68**, 3290 (1996).
[2] S. Binetti, M. Donghi, S. Pizzini, A. Castaldini, A. Cavallini, B. Fraboni, and N. A. Sobolev, Solid State Phenomena **57–58**, 197 (1997).
[3] N. A. Sobolev, Fiz. Tekh. Poluprovodn. **29**, 1153 (1995) [Semiconductors **29**, 595 (1995)].
[4] H. Przybylinska, W. Jantsch, Yu. Suprun-Belevitch, M. Stepikhova, L. Palmetshofer, G. Hendorfer, A. Kozanecki, R. J. Wilson, and B. J. Sealy, Phys. Rev. B **54**, 2532 (1996).
[5] V. A. Tolomasov, L. N. Abrosimova, and G. N. Gorshenin, Kristallogr. **15**, 1233 (1970) [Sov. Phys. Crystallogr. **15**, 1076 (1970)].

Translated by Steve Torstveit

AlGaAsSb lasers emitting in the 1.6 μm region

T. N. Danilova, B. E. Zhurtanov, A. N. Imenkov, M. A. Sipovskaya, and Yu. P. Yakovlev

A. F. Ioffe Physicotechnical Institute, Russian Academy of Sciences, St. Petersburg
(Submitted November 19, 1998)
Pis'ma Zh. Tekh. Fiz. **25**, 35–41 (May 26, 1999)

AlGaAsSb lasers with different Al concentrations in the active and confinement regions are fabricated and investigated. The structures lase in the region $\sim$1.6 μm. The AlGaAsSb solid solution in the active region is a direct-gap material with a small energy separation ($\sim$56 meV) between the direct-gap Γ minimum and the indirect-gap L minimum of the conduction band. The lasers have a single-mode spectrum with a predominant longitudinal mode in the spatial distribution of the emission. The lasers operate at room temperature in a pulsed mode. © *1999 American Institute of Physics.* [S1063-7850(99)02305-8]

1. Lasers emitting in the spectral region near 1.6 μm are promising for diode-laser spectroscopy, since they operate at room temperature and this spectral region contains overtones of the absorption lines of certain gases of great practical interest, such as methane (CH_4), carbon dioxide (CO_2), and others, whose fundamental absorption bands lie in the mid-infrared region (3–4 μm), where room-temperature lasing has not been achieved. To compensate for the weak absorption of light at overtones in comparison with the fundamental absorption, one usually uses multipass cells containing the gas under study.[1] This principle has been used, e.g., to construct a portable methane analyzer using a laser in the solid solution InGaAsP for measurements in the open atmosphere.[2] By now devices with a very high spectral resolution have been made using InGaAsP/InP heterostructure diode lasers for sensitive optical detection and differentiation of the close-lying overtone $2\nu_3$ of the CH_4 absorption line and the $6\nu_2+\nu_3$ combination line of CO_2 in the 1.6 μm spectral region.[3,4]

We undertook the construction and study of diode lasers based on another semiconducting solid solution, AlGaAsSb, and working in the $\sim$1.6 μm spectral region. The lasers contain a heterostructure with active and wide-gap regions consisting of the same solid solution AlGaAsSb but with different Al concentrations. In the AlGaAsSb solid solution the energy distance between the direct-gap Γ minimum and the indirect-gap L minimum in the direct-gap compositions is less than 100 meV. It is of interest to determine whether lasing is possible with an active region containing this semiconductor material.

2. The laser structures were fabricated by liquid-phase epitaxy (LPE) on an *n*-GaSb(100) substrate doped with Te to a free electron concentration of $(8-9)\times10^{17}$ cm^{-3}. The arrangement of the layers in the laser structure is illustrated in Fig. 1a. All the layers grown were isoperiodic with the substrate. The matching of the periods of the substrate and narrow-gap layer was $\Delta a/a=(8-9)\times10^{-4}$, and that of the substrate and wide-gap layers was $\Delta a/a\sim10^{-3}$. The narrow-gap layer of the active region, with a composition of $Al_{0.05}Ga_{0.95}As_{0.044}Sb_{0.956}$ was doped with Te to a free electron concentration of $(3-5)\times10^{17}$ cm^{-3}. The thickness of this narrow-gap layer was 0.5 μm. Wide-gap layers with a larger Al concentration ($Al_{0.34}Ga_{0.66}As_{0.044}Sb_{0.956}$) were then grown. The *N*-type wide-gap layer was doped with Te to a free electron concentration of $(3-5)\times10^{17}$ cm^{-3} and a the *P*-type wide-gap layer was doped with Ge to a free hole concentration of $\sim7\times10^{17}$ cm^{-3}. The narrow-gap *P*-layer near the contacts had the same composition as the active region and was doped to a hole concentration of $\sim1\times10^{19}$ cm^{-3}. The wide-gap layers were $\sim$2.5 μm thick, and the heavily doped layer near the contact was $\sim$1.5 μm thick.

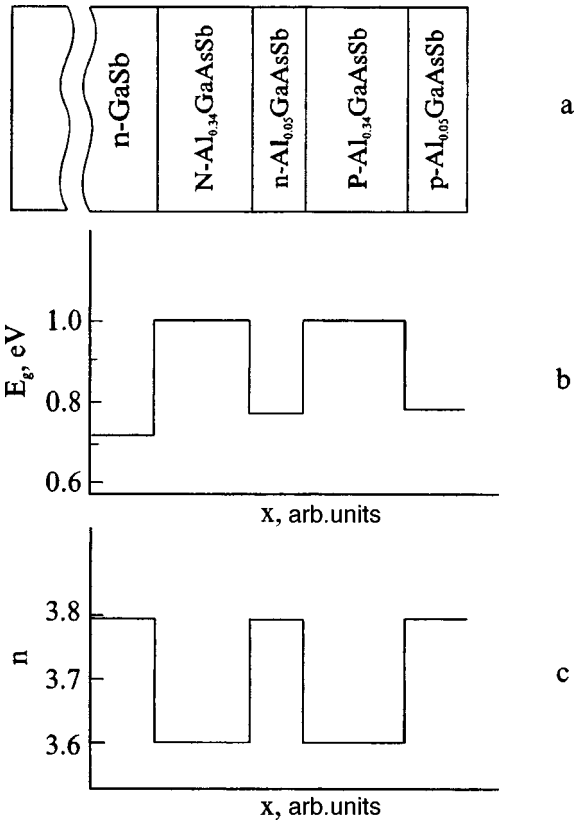

FIG. 1. Diagram of the arrangement of the layers in the laser structure (a), the band gap E_g in the layers (b), and the refractive index n in the layers (c).

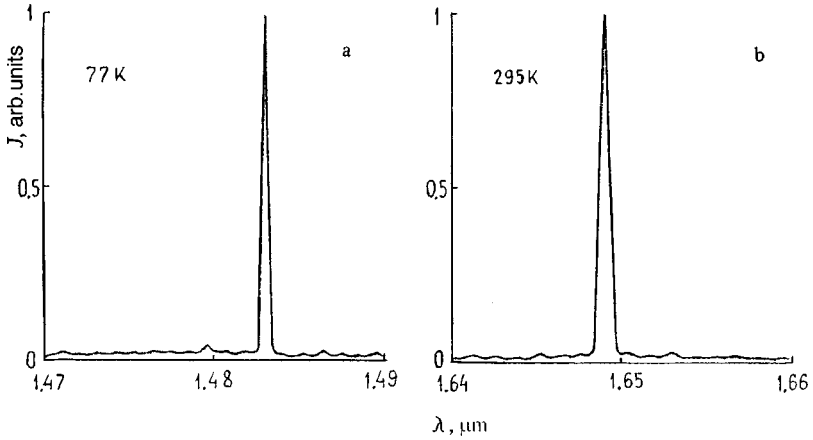

FIG. 2. Emission spectra of the laser E-174 N 14 at 77 K (a) and at room temperature (b).

The variation of the band gap E_g over the thickness of the structure at room temperature is shown in Fig. 1b. In the active region $E_g \sim 0.775$ eV, corresponding to a radiation wavelength $\lambda \sim 1.6$ μm. In the wide-gap confinement regions E_g has a value of ~ 1.0 eV. The heavily doped *P*-layer near the contacts has approximately the same value of E_g as the active region. The solid solution $Al_xGa_{1-x}AsSb$ in the active region ($x=0.05$) is a direct-gap material, while that in the wide-gap regions ($x=0.34$) is indirect-gap, since the transition from an absolute Γ minimum to an absolute *L* minimum occurs at $x=0.25$ (Refs. 5 and 6). In the active region, however, the indirect-gap *L* minimum is close to the direct-gap Γ minimum, with an energy separation between them of ~ 56 meV. The heterointerfaces between the active region and the wide-gap confinement regions are type-*I* heterojunctions with a discontinuity in the conduction band of $E_c \sim 120-150$ meV and with a discontinuity in the valence band of $E_v \sim 150-170$ meV.

The variation of the refractive index *n* over the thickness of the structure is sketched in Fig. 1c. The numbers given are calculated values. The refractive index in the active region has a value close to that in GaSb, approximately 3.79. The refractive index in the $Al_{0.34}Ga_{0.66}As_{0.044}Sb_{0.956}$ wide-gap confinement region was ~ 3.6. Thus the difference of the refractive indices between the active and wide-gap regions was $\Delta n \sim 0.19$.

Mesa stripes ~ 10 μm in width were prepared from the epitaxial laser structure by photolithography. Fabry–Perot laser cavities 200–250 μm long were formed by cleaving.

The emission spectra, far-field radiation pattern, and current–voltage characteristics of the lasers were measured.

The emission spectra were measured at 77 K and at room temperature. An MDR-2 monochromator was used as a dispersive device. The photodetector was a GaInAsSb photodiode.[7] In the measurements at 77 K the supply current was in the form of a ''meander'' of pulses with a repetition rate of 400 Hz. At room temperature the supply current pulses had a duration $\tau=500$ ns and a repetition rate of 30 kHz.

3. The emission spectrum of one of the lasers investigated (E-174 N 14) is shown in Fig. 2; the spectrum at 77 K at a current of 40 mA is shown in Fig. 2a, and the spectrum at room temperature and 880 mA is shown in Fig. 2b. The laser has a threshold current of 27.5 mA at 77 K and ~ 800 mA at room temperature. All the lasers have single-mode emission spectra. The shift of the wavelength with temperature from 77 K to room temperature occurs at a rate of ~ 7.6 Å/deg.

Figure 3 shows the far-field spatial distribution of the laser radiation in the plane of the $p-n$ junction for a current of 30 mA and a temperature of 77 K. The directional pattern has a predominant longitudinal mode with a width of 10.8° at half maximum intensity. The side maxima probably correspond to transverse modes, their combined intensity being approximately one-fourth the intensity of the longitudinal mode. The intensity of the transverse modes decreases with increasing mode number. In a plane perpendicular to the $p-n$ junction the width of the directional pattern at half maximum intensity is 40–50°.

From the measured current–voltage characteristics of the

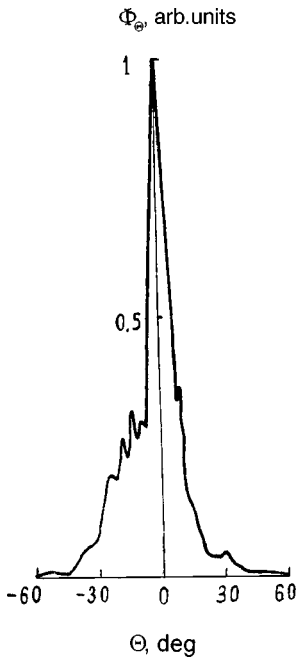

FIG. 3. Distribution of the emission energy Φ in the far zone versus the radiation detection angle Θ for the laser E-174 N 14.

laser at room temperature it was found that the residual resistance of the laser structures is $\sim 28\ \Omega$.

4. Let us discuss the results.

The main result of this study is the achievement of lasing in a laser with an active region consisting of a direct-gap material in which the indirect-gap L minimum lies close to the direct-gap Γ minimum, at an energy separation of ~ 56 meV. Estimates show that under conditions of lasing in such a material the energy density in the side, indirect-gap minimum of the conduction band is an order of magnitude higher than in the main, direct-gap minimum.

The lasers have a single-mode spectrum with a spatial distribution predominantly in the longitudinal mode. The shift of the coherent emission wavelength as the temperature is raised from 77 K to room temperature occurs at a rate which is approximately one-half as large as the rate that would correspond to the change in the band gap in the active region of the laser in this same temperature interval.

The presence of transverse modes in the spatial distribution of the laser emission is probably due to the fact that the stripe width is too large for an emission wavelength of 1.6 μm. This may be taken into consideration in a later study.

Because the confinement layers of the structure are indirect-gap, the lasers have a high series resistance (28 Ω), which, however, can be decreased by increasing the doping of these layers.

This study was supported in part by the contract INCO-Copernicus N 1C15-CT97-0802 (DG12-CDPF) and in part by a grant from the Ministry of Science of the Russian Federation under the program ''Optics and Laser Physics.''

[1] S. M. Chernin and E. G. Barskaya, Appl. Opt. **30**, 51 (1991).
[2] A. Beresin, S. Chernin, O. Ershov, V. Kutnyak, and A. Nadezhdinskii, *Second International Conference on Tunable Diode Laser Spectroscopy*, Moscow (1998), Abstracts of papers, p. 33.
[3] V. Weldon, P. Phelan, and J. Hegarty, Electron. Lett. **28**, 2098 (1992).
[4] V. Weldon, P. Phelan, and J. Hegarty, Electron. Lett. **29**, 560 (1993).
[5] C. A. Mead and W. G. Spitzer, Phys. Rev. Lett. **11**, 358 (1963).
[6] Yu. A. Akimov, A. A. Burov, E. A. Zagarinskiĭ, I. V. Kryukova, Yu. V. Petrushenko, and B. M. Stepanov, Kvantovaya Elektron. (Moscow) **2**, 68 (1975) [Sov. J. Quantum Electron. **5**, 37 (1975)].
[7] I. A. Andreev, A. N. Baranov, M. A. Afrailov, V. G. Danil'chenko, M. P. Mikhaĭlova, and Yu. P. Yakovlev, Pis'ma Zh. Tekh. Fiz. **12**(21), 1311 (1986) [Sov. Tech. Phys. Lett. **12**(11), 542 (1986)].

Translated by Steve Torstveit

Magnetoresistance of nanobridges of lanthanum–strontium manganite

V. A. Berezin, V. I. Nikolaïchik, V. T. Volkov, Yu. B. Gorbatov, V. I. Levashov, G. L. Klimenko, V. A. Tulin, V. N. Matveev, and I. I. Khodos

Institute of Microelectronics and High Purity Materials, Russian Academy of Sciences, Chernogolovka
(Submitted December 22, 1998)
Pis'ma Zh. Tekh. Fiz. **25**, 42–50 (May 26, 1999)

Nanobridges are fabricated from lanthanum–strontium manganite deposited on Si_3N_4 membranes perforated by a focused ion beam. The magnetoresistance is $\approx 9\%$ in fields of ~ 1 kOe. Nonlinearity of the current–voltage characteristic of the bridges is observed, and it is found that the maximum of the resistance is shifted to lower temperatures from that of a control film sample of composition $La_{0.8}Sr_{0.2}MnO_3$. © *1999 American Institute of Physics.* [S1063-7850(99)02405-2]

The properties of rare-earth manganites $A_{1-x}B_xMnO_3$, where A is a rare-earth element (La, Pr, Nd) and B is an alkaline-earth (Ca, Ba, Sr) are currently under active study. These materials are of interest because of the colossal magnetoresistance effect observed in them.[1] The published data on the conductivity of manganite materials were obtained for bulk and film samples of macroscopic dimensions. To understand the mechanisms of electron transport in manganites and to use these materials to make various nanosensors and magnetic recording devices, it will be necessary to have information about the properties of samples of small dimensions. In this paper we make the first report of the fabrication of nanometer bridges of lanthanum–strontium manganite and a study of their magnetoresistance.

The starting components for the synthesis of the $La_{0.8}Sr_{0.2}MnO_3$ targets were La and Mn oxides (La_2O_3 and MnO_2) and strontium carbonate ($SrCO_3$). The mixture of starting components was heat treated at a gradual increase in temperature with a two-hour hold at 300, 400, 650, and 900 °C. Then the powders were reground and pressed into tablets, which were sintered at $T=1385$ °C in air for one hour.

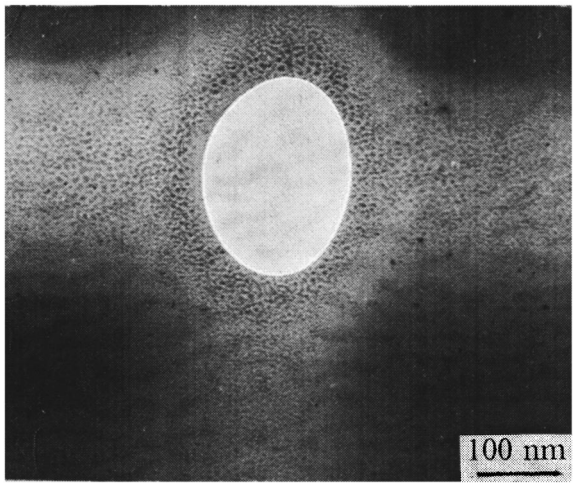

FIG. 1. Hole made by a focused ion beam in a Si_3N_4 membrane.

To form the nanobridges we started from Si_3N_4 membranes[2] about 100 nm thick. A focused ion beam was used to make holes <500 nm in diameter in the membranes (Fig. 1). Then an Al_2O_3 layer of definite thickness was deposited on the membrane from both sides by rf-diode sputtering of a sapphire target; this made it possible to reduce the size of the holes to the required value and prevented the manganite from interacting with the membrane material. In this way channels with a characteristic cross section <100 nm in diameter and up to 200 nm long were formed. The channels were filled with manganite by the laser deposition of a $La_{0.8}Sr_{0.2}MnO_3$ film 250 nm thick on both sides of the membrane. Prior to deposition of the manganite the membranes were vacuum-baked 800 °C directly in the vacuum chamber at a residual gas pressure of 10^{-5} Pa. The deposition was carried out at a sample temperature of 700 °C and an oxygen pressure of 10 Pa.

The deposition was done with the use of a pulsed laser at wavelength 1.06 μm. The beam was focused on the target by a long-focus lens located outside the vacuum chamber. The power density at the rotating target was $\sim 10^9$ W/cm^2 in a pulse 10 ns long. At a pulse repetition rate of 15 Hz and a target-to-sample distance of 60 mm the deposition rate was ≈ 0.4 nm/s. After deposition of the manganite film the samples were annealed in air at 850 °C for one hour and then cooled at a rate of 0.1 deg/s.

The target material was investigated under a JEM-2000FX transmission electron microscope equipped with an

TABLE I.

Sample No.	Dimensions of channel before deposition of manganite	R (300 K), kΩ	R (77 K), kΩ	$\frac{R(0\text{ Oe})-R(6\text{ kOe})}{R(0\text{ Oe})}$ at 77 K
1	50×85 nm	1890	2577	0.085
2	25×75 nm	257.4	465	0.159
3 (control sample)	5×2 mm $h=250$ nm	73.7	50.9	0.189

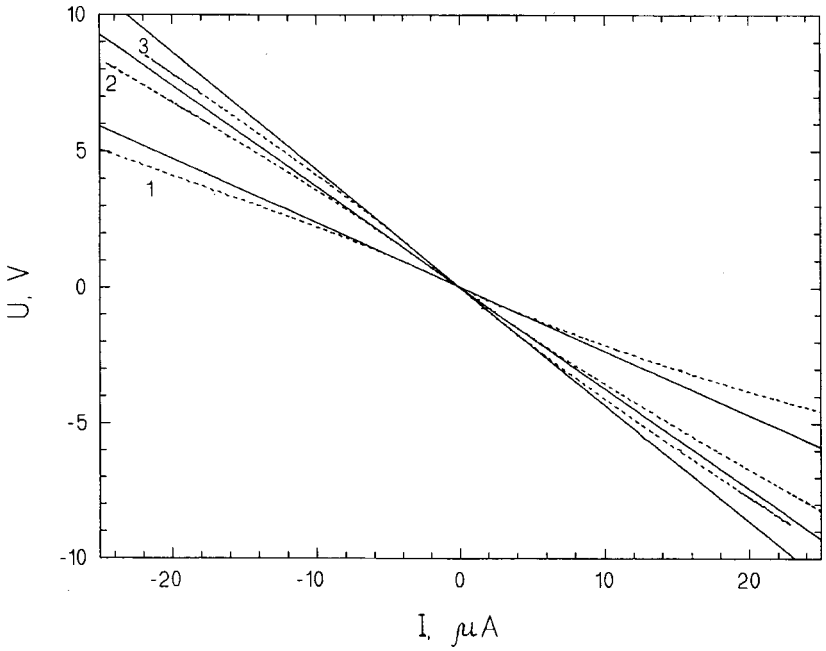

FIG. 2. Current–voltage characteristics of sample No. 2, with a manganite nanobridge. The dotted lines are experimental, the solid lines are approximations of the linear parts of the experimental curves. *1* — $T=300$ K, $H=0$ Oe; *2* — $T=77$ K, $H=6$ Oe; *3* — $T=77$ K, $H=0$ Oe.

AN10/95S elemental analysis system; it was found that the target was single-phase and chemically uniform, with the ratio of metallic elements in correspondence with their proportions in the starting mixture. Observations of the structure of the deposited manganite films revealed that they are polycrystalline, with an average grain size ≈ 50 nm. Also, in contrast to the uniform target material, the structure of the films contained nonuniformities in the form a small number of inclusions (droplets) with an elemental composition different from that of the main body of the grain. The presence of such inclusions is typical for laser-deposited films of other metallic oxide materials as well, including high-temperature superconductors; thus it is necessary to choose the deposition conditions so as to minimize droplet formation.

To study the electrical and magnetic properties of the nanobridges we measured the temperature and field dependences of the resistance. The parameters of samples Nos. 1 and 2, with nanobridges, and of a control sample (a manganite strip 5 mm long and 2 mm wide, deposited and annealed simultaneously with the bridge samples) are given in Table I. The expected values of the resistance for the bridges lay in the range from hundreds of kΩ to several MΩ. With such high resistances there was a significant chance that the samples would be overheated by the measuring current. To avoid this risk, the current–voltage (I–V) characteristic of the sample was measured beforehand. An example of the I–V characteristic for sample No. 2 is shown in Fig. 2 (similar behavior was observed for sample No. 1). It is seen that

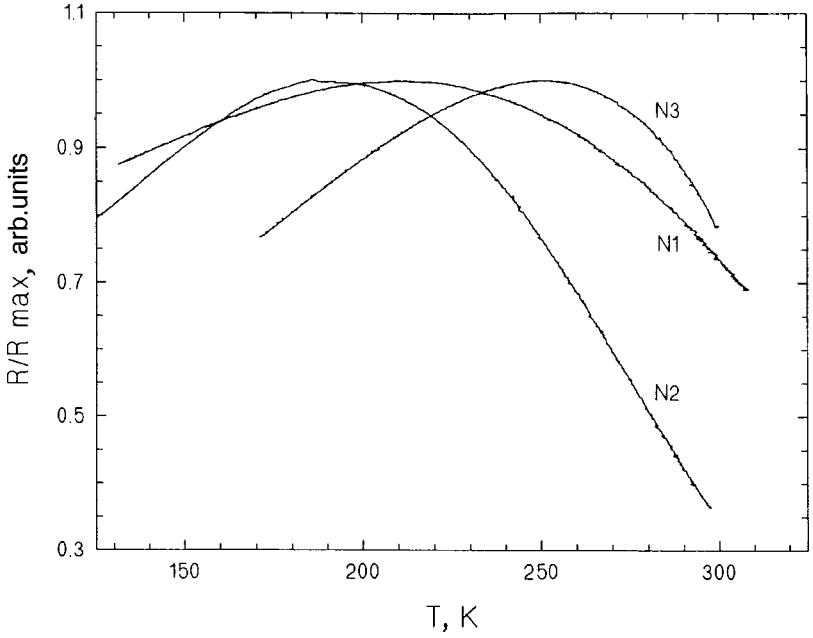

FIG. 3. Temperature dependence of the resistance of nanobridge samples Nos. 1 and 2 and of control sample No. 3; the curves are normalized to the maximum value of the resistance for each.

above a certain value of the current (here around 5 μA) Ohm's law breaks down, and the resistance of the sample with the bridge begins to decrease. The cause of the nonlinearity of the I–V characteristic of the bridge samples is discussed below. The magnetic measurements were done in the linear region of the I–V characteristic.

Figure 3 shows the temperature dependence of the resistance for the bridge samples and the control sample. Since the resistance of the samples was quite different, the curves in Fig. 3 show the values divided by the maximum resistance for each sample. The curves reveal the shift of the position of the resistance maximum to lower temperatures as the transverse size of the bridge decreases. It is known that the maximum of the resistance of manganite conductors of macroscopic size lies near the Curie point, which is determined by the composition of the manganite material, viz., the ratio of the rare-earth and alkaline-earth elements,[3] and the oxygen content.[4]

One notices that the resistance of sample No. 1, in which the channel dimensions prior to deposition of the manganite film were 50×85 nm, is larger than the resistance of sample No. 2, in which the initial channel was smaller (25×75 nm). Moreover, published data[3,4] indicate that a higher value of the temperature of maximum resistance corresponds to a lower resistivity, i.e., sample No. 1 Should have the lower resistivity. The contradiction in these data may be explained by the circumstance that in sample No. 1 the channel contained not only a material of high conductivity, the temperature dependence of which determines the form of the curve in Fig. 3, but also a larger amount of a material of low conductivity. The coexistence of two types of materials can be explained by the presumed cluster structure of the manganite material, which is made up of mixed regions (several nanometers in size) of different materials[6] with high and low conductivity.[5] The conductivity of the bulk manganite material (the control sample) is an averaged quantity determined by the passage of charge carriers through a heterogeneous region. For samples of small dimensions there is a much higher probability that high-resistance or insulating regions will be predominantly present. The latter could fill the channel of sample No. 1 in large numbers.

Figure 4a and b shows the magnetoresistance of the control sample and of bridge sample No. 1 for various orientations of the magnetic field with respect to the sample. It is seen that the control sample has a pronounced anisotropy due to the fact that the sample is in the form of a film. The fact that no such anisotropy is observed for the bridge sample indicates that the bridge is of a more equiaxed form. The two samples have approximately the same values of the coercive force ($\approx$150 Oe) and of the change in resistance in a magnetic field ($>$10% in a field of 6 kOe). An important circumstance which permits their use as magnetic field sensors is that a significant change in resistance ($\approx$9%) occurs in fields as low as $\sim$1 kOe.

The observed nonlinearity of the I–V characteristics of the bridges cannot be explained by a simple thermal overheating of the sample. In this connection let us estimate the possible elevation of the temperature of a bridge when a power between 10 and 200 μW is dissipated in it (for simplicity, we take the dimensions of the bridge to be 100 ×100×100 nm). Assuming that the thermal conductivity of manganite has a typical value for oxide materials,[7] $\lambda \sim 10^{-2}$–10^{-1} W·m^{-1}·K^{-1} at 300 °C, we estimate that the temperature at the center of the nanobridge will be at most 20–40 deg higher than at its edge. Thus the power released

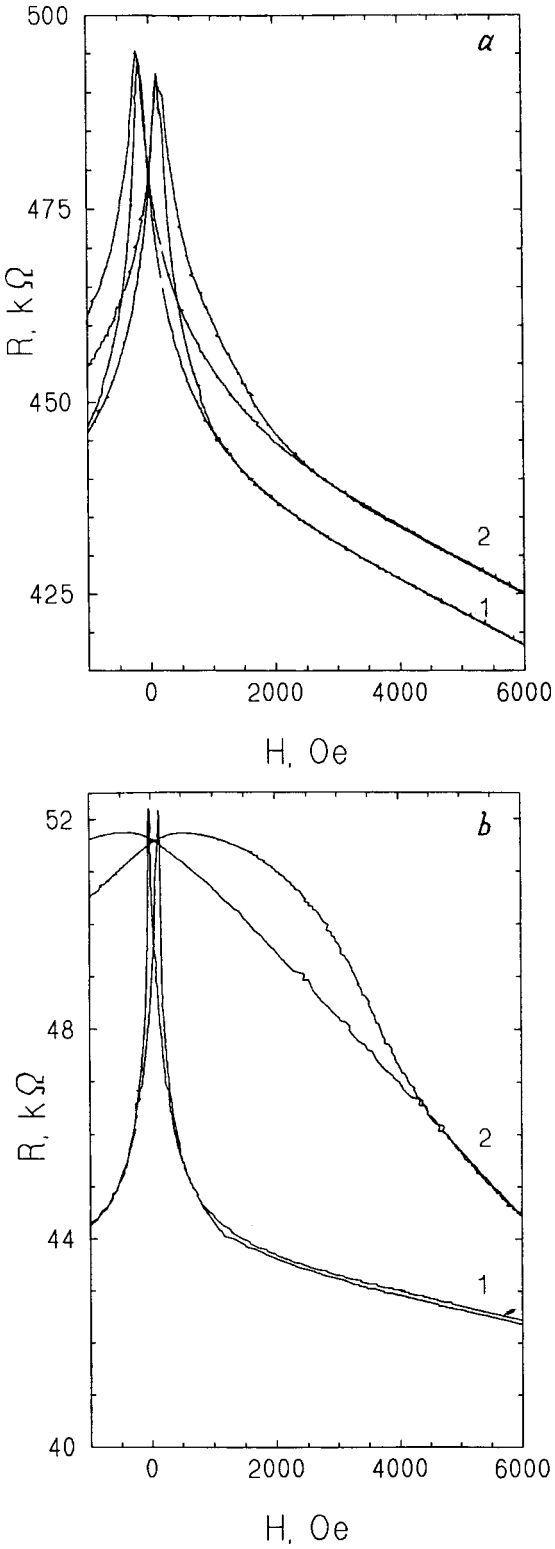

FIG. 4. Field dependence of the resistance at $T=77$ K. a: Control sample; b: nanobridge sample No. 2. The magnetic field was directed parallel (*1*) and perpendicular (*2*) to the plane of the manganite film.

will be effectively removed to the contacts and side walls, and the nanobridge should not overheat. This estimate is supported by the fact that the nonlinear dependence is observed both at temperatures below the resistance maximum (the region of metallic conductivity) and at temperatures above the resistance maximum (the region of semiconductor conductivity). Similarly, the nonlinearity cannot be caused by the magnetic field of the current. Estimates show that the magnetic field of the current is quite small (~ 1 Oe). The nonlinear dependence might be due to the opening up of additional channels of conduction as the electron energy increases.

In closing, let us emphasize the following. We have for the first time fabricated nanometer objects (bridges) of lanthanum–strontium manganite, which exhibits the giant magnetoresistance effect. The size of the effect is comparable to that in manganite films, and an appreciable change in resistance ($\approx 9\%$) occurs in fields of only ~ 1 kOe. We have observed nonlinearity of the I–V characteristic of the nanobridge samples and a shift of their resistance maximum to lower temperatures as compared to a film control sample of composition $La_{0.8}Sr_{0.2}MnO_3$.

This study was supported by the Russian Fund for Fundamental Research (Grant 96-02-17123) and the Government Program ''Physics of Solid-State Nanostructures'' (Grant 97–1063).

[1] S. Jin, T. H. Tiefel, M. McCormack *et al.*, Science **264**, 413 (1994).
[2] A. Yu. Kasumov, V. I. Levashov, V. N. Matveev, V. A. Berezin, and V. A. Tulin, Mikroelektronika **26**, 49 (1997).
[3] A. Urushibara, Y. Morito, T. Akima *et al.*, Phys. Rev. B **51**, 14103 (1995).
[4] H. L. Ju, C. Kwon, Qi Li *et al.*, Appl. Phys. Lett. **65**, 2108 (1994).
[5] É. L. Nagaev, Usp. Fiz. Nauk **166**, 833 (1996).
[6] V. I. Nikolaichik and L. A. Klinkova, *Abstracts of the Fifth International Workshop MSU-HTSC V* (1998), p. F-14.
[7] C. Uher and A. B. Kaiser, Phys. Rev. B **36**, 5680 (1987).

Translated by Steve Torstveit

Hyperboloid mass spectrometer with a truncated trap

E. V. Mamontov and D. A. Ivlev

Ryazan State Radio Engineering Academy
(Submitted December 8, 1997)
Pis'ma Zh. Tekh. Fiz. **25**, 51–56 (May 26, 1999)

A hyperboloid mass spectrometer is proposed in which the analyzer is a three-dimensional ion trap truncated by the plane $z=0$. The mass peaks for different operating regimes of the mass analyzer are constructed from the results of a numerical modeling of the electric field and a simulation of the process of sorting the charged particles. The results serve as a basis for the construction of a hyperboloid mass spectrometer with a simple electrode system and a high resolving power. © *1999 American Institute of Physics.* [S1063-7850(99)02505-7]

Hyperboloid mass spectrometers (HMSs) utilize quadrupole mass filters and ion traps as analyzers of particles according to the specific charge.[1] The electrode systems of these analyzers are complicated to fabricate and assemble. The monopole analyzer has a simplified construction of the electrode system but a limited resolving power. The analyzer proposed here, which utilizes a truncated ion trap, can be used to construct a HMS with a simple construction of the electrode system and good analytical parameters and which also effectively solves the problems of ion injection and extraction.

The electrode system of the analyzer (Fig. 1) consists of half the electrode system of an ion trap, in the hemisphere $z>0$. It consists of two successive hyperboloid electrodes *1* and *2*, with minimum distances of Z_0 and R_0 from the coordinate origin ($Z_0=5R_0$), and a shielding electrode *3*. The ideal potential distribution in the analyzer, which does not take into account the finiteness of the electrode system, is described by the expression

$$\Phi(z,r)=\frac{(\Phi_1-\Phi_2)(z^2-r^2/2)+\Phi_1R_0^2/2+\Phi_2Z_0^2}{Z_0^2+R_0^2}. \quad (1)$$

An opening in the ring electrode *2* permitted injecting the ions into the analyzer prior to the start of the sorting process and to remove the sorted ions for detection after its completion. The sorting space of the truncated trap along to the z coordinate is restricted to positive values, and the charged particles can execute only unipolar oscillations $z(t)\geqslant 0$ in it under the influence of an rf field. In a field with a quadratic potential distribution (1) such oscillations correspond to the boundary $a_0(q)$ of the stability diagram and are described by the relation[2]

$$z(t)=Ace_0(t,q)+Bfe_0(t,q), \quad (2)$$

where $ce_0(t,q)$ and $fe_0(t,q)$ are periodic and aperiodic zeroth-order solutions of the Hill equation, and A and B are parameters which depend on the initial coordinate z_0 and initial velocity ν_0 of the charged particles. In this case the sorting of the particles according to specific charge can be done with respect to a single coordinate.[3] When the volume of the trap is limited, the potential distribution in the region $z<2R_0$ is considerably different from (1), and the character of the trajectories of ions with light masses $m<m_0$ (m_0 is the mass of the ions to be analyzed) is altered in such a way that these ions fall in the region of nonlinear distortions. Since the efficiency of one-dimensional sorting is lowered, it is of interest to create a regime of two-dimensional sorting of ions in a unipolar analyzer.

To estimate the analytical capabilities of such a regime we did a computer simulation of the sorting of charged particles in a truncated trap with the parameters $Z_0=32$ mm, $R_0=6$ mm, and $D=80$ mm. The sorting space of the analyzer (the active zone *4*) is bounded by a cylinder of radius R_0. In the first step the electric field in the analyzer was modeled for fixed potentials Φ_1, Φ_2, and Φ_3 on the end electrode *1*, the ring electrode *2*, and the shielding electrode *3*, and the deviation $\Delta\Phi(z,r)$ of the potential in the active zone from the ideal value was determined. According to the value of $\Delta\Phi(z,r)$ the active zone was divided up into regions with substantial and unimportant distortions of the field. In the region $2R_0\leqslant z\leqslant Z_0$ at the optimum value of the potential $\Phi_3=0.275\Phi_1$ on the shielding electrode the error in the potential distribution does not exceed $0.4\times10^{-4}\Phi_1$ and has practically no influence on the ion trajectories at a

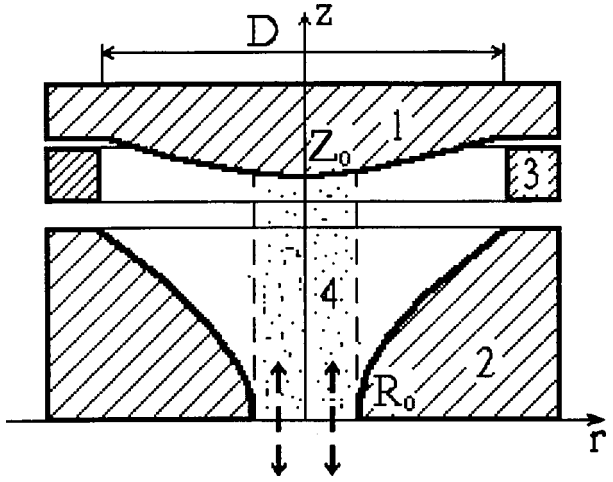

FIG. 1. Electrode system of the analyzer.

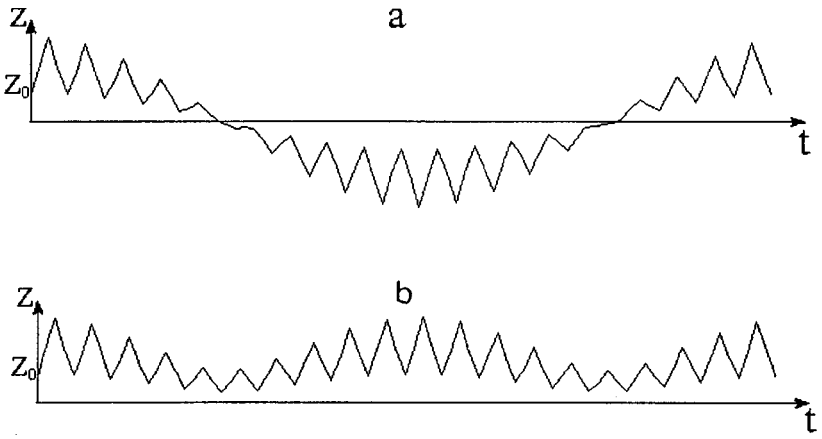

FIG. 2. Trajectories of ions with $m=0.99m_0$ in the ideal field (a) and in a field with nonlinear distortions, with $\lambda=0.33$ (b).

HMS resolving power of several thousand. In the region of substantial distortions $0\leqslant z\leqslant 2R_0$ the deviation of the potential from Eq. (1) for the indicated parameters of the analyzer were approximated by the function

$$\Delta\Phi(z,r)\approx -7.7\cdot 10^{-3}\Phi_1\exp(-14.5z/Z_0)\times\exp(-70r^2/R_0^2). \quad (3)$$

The second step in the simulation was to calculate the ion trajectories and mass peaks of the analyzer with allowance for the error in the potential distribution (3) under the influence of an rf field on the charged particles. The rf field was produced by a potential difference $\Phi_0(t)=\Phi_1-\Phi_2$ between the field-forming electrodes. The pulsed voltage source $\Phi_0(t)=U+V\psi(\omega t)$ with an initial phase $\varphi_{02}=\pi/2$, where U and V are the dc component and the amplitude of the rf voltage, respectively, and $\psi(\omega t)$ is a normalized periodic function. Before the start of the sorting the values $\Phi_1=\Phi_2=\Phi_3=0$ were imposed, and ions were injected in the analyzer at initial coordinates $z_0=2R_0$ and with thermal initial velocities ν_0. Here the parameters z_0 and ν_0 of the ions were matched with the initial phase $\varphi_{02}=\pi/2$ of the rf voltage.[4] The trajectories of the charged particles with respect to the coordinates z and r were calculated by numerical solution of second-order nonlinear equations with periodic coefficients:

$$\frac{d^2z}{dt^2}+[a+2q\phi(\omega t)]\left(z+k\frac{\partial\Delta\Phi}{\partial z}\right)=0,$$

$$\frac{d^2r}{dt^2}-[a/2+q\phi(\omega t)]\left(r+k\frac{\partial\Delta\Phi}{\partial r}\right)=0, \quad (4)$$

where a and q are sorting parameters which depend on the dimension Z_0 of the analyzer and the parameters U, V, ω and the shape of the rf voltage, and $k=(Z_0^2+R_0^2/2)/2(\Phi_1-\Phi_2)$. It was found that the motion of the ions with light masses $m<m_0$ ($m\approx m_0$) along the z coordinate has the peculiar feature that for particles with $m<m_0$ the trajectories, which in the ideal field alternate in sign, become unipolar (Fig. 2) in the presence of potential deviations of the form in Eq. (3). This occurs because the ions with $m<m_0$, which in the initial step of the sorting are found in the ideal-field region, are subsequently displaced along z into the region of nonlinear distortions with a higher field than in the ideal case. As a result, the ions that do not cross the axis $z=0$ return to the initial oscillation region. Here the ion trajectories take on the character of unipolar beats (Fig. 2b), and one-dimensional sorting of the ions becomes inefficient. In that case it is advisable to use sorting with respect to the coordinate r for filtering of the light ions; such a sorting is realized when operating at the vertex of zone I of the stability diagram at $\lambda=U/2V$ close to 0.3455.[1]

The mass peaks were obtained from integral representations of the properties of the mass analyzer with a truncated trap, on the basis of a calculation of a set of trajectories of 5×10^3 ions with various initial coordinates $z_0=(0.2$–$0.35)Z_0$, $r_0=-R_0$ to R_0, and thermal initial velocities, with allowance for the nonlinear distortions of the field. The results of the calculations are presented in Fig. 3. Curve *1* corresponds to the one-dimensional regime of ion sorting, in which, because of the nonlinear distortions of the field the efficiency of the filtering of light ions is low. In this case the mass peak has a gentle declivity on the left-hand side, and

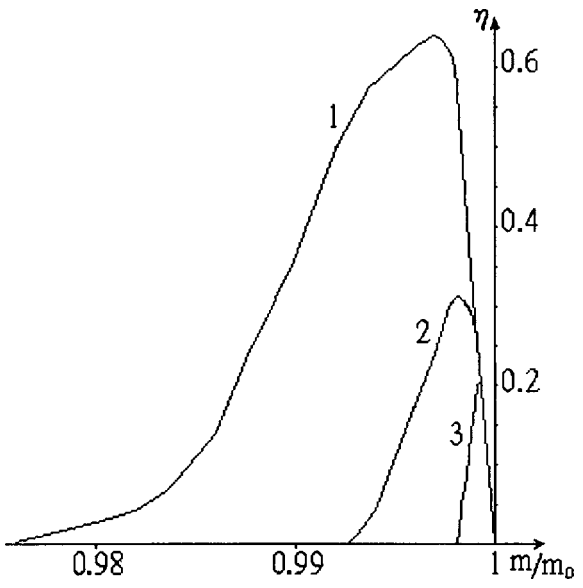

FIG. 3. Mass peaks for a hyperboloid mass spectrometer with a truncated trap. The number of sorting periods $n=20$: *1* — $\lambda=0.33$; *2* — $\lambda=0.34$; *3* — $\lambda=0.344$.

the resolving power does not exceed 50. Curves *2* and *3* were obtained with the analyzer operating in the vicinity of the vertex of zone I of the stability diagram, where the light masses are filtered out with respect to the r coordinate. At $\lambda = 0.344$ the resolving power reaches a value $\rho_{0.5} = 850$. Effective confinement of the particles to be analyzed (the intensity of the peak is 20% of the maximum) is ensured by having the optimum initial phase of the rf voltage, $\varphi_{02} = \pi/2$, at which the initial velocities of the ions have less influence, and the amplitudes of the oscillations with respect to the r coordinate for the stable ions are an order of magnitude smaller than at other injection phases. Optimization of the analyzer parameters and of the ion sorting regime could increase the resolving power of the HMS to several thousand.

In summary, a simulation of the charge-particle sorting processes in a hyperboloid analyzer of the truncated trap type has demonstrated the possibility of building a hyperboloid mass spectrometer with a simple electrode system and with good analytical parameters.

[1] R. E. March and R. J. Hughes, *Quadrupole Storage Mass Spectrometry*, Wiley, New York (1989), 463 pp.
[2] N. W. McLachlan, *Theory and Application of Mathieu Functions*, Clarendon Press, Oxford (1947) [Russ. transl., IL, Moscow (1953), 468 pp.].
[3] E. V. Mamontov, Izv. Akad. Nauk SSSR, Ser. Fiz. **62**, 2039 (1998).
[4] E. V. Mamontov, *Proceedings of the Fourteenth Mass Spectrometry Conference*, Helsinki, Aug. 25–29, 1997, p. 228.

Translated by Steve Torstveit

Faraday compensator of reciprocal optical anisotropy utilizing a polarization ring interferometer

V. M. Gelikonov, G. V. Gelikonov, V. V. Ivanov, and M. A. Novikov

Institute of Applied Physics, Russian Academy of Sciences, Nizhniĭ Novgorod; Institute of the Physics of Microstructures, Russian Academy of Sciences, Nizhniĭ Novgorod

(Submitted November 11, 1998)
Pis'ma Zh. Tekh. Fiz. **25**, 57–63 (May 26, 1999)

It is shown that a polarization ring interferometer containing a Faraday cell can be used to compensate the reciprocal anisotropy in round-trip optical circuits. It is established theoretically and experimentally that, unlike the case of conventional Faraday mirrors, the quality of the restoration of the polarization in a compensator based on a polarization ring interferometer is practically independent of the Faraday rotation angle. A deviation of the Faraday rotation angle from 45° leads only to an additional power loss. The novel compensators can be used in fiber-optic circuits with a wideband light source or with several sources having different wavelengths. © *1999 American Institute of Physics.* [S1063-7850(99)02605-1]

Compensators of reciprocal optical anisotropy which utilize Faraday rotators — so-called Faraday mirrors — are widely used at the present time in round-trip optical circuits,[1–5] in particular, in fiber-optic interferometers[3] and optical amplifiers.[4,5] The simplest Faraday mirror[1,2] is a combination of a 45° Faraday rotator and a rotating mirror. As was shown in Ref. 1, in a round-trip optical circuit consisting of a Faraday mirror and a reciprocal element placed in front of it having arbitrary phase anisotropy (e.g., a length of single-mode optical fiber), the output polarization is always orthogonal to the input polarization, regardless of the anisotropy and input polarization. This allows one to obtain a stable polarization at the output of a round-trip anisotropic optical system with unstable parameters.

However, if the angle of rotation of the Faraday rotator differs from 45°, the Faraday mirror[1] will not provide complete compensation of the parasitic anisotropy. The intensity of the undesirable component of the output polarization is

$$I_{\parallel} \sim \sin^2 2\Delta\theta, \tag{1}$$

where $\Delta\theta$ is the deviation of the angle of rotation of the Faraday rotator from 45°. The compensation error (1) can arise as a result of temperature instability of the Faraday rotation (which is present to some degree in all magnetooptical materials) or on account of degradation of the permanent magnet of the Faraday rotator. In addition, because of the frequency dispersion of the Faraday rotation, the compensation error (1) is always present in circuits with a wideband light source or with several sources having different wavelengths.

In this paper we propose and investigate experimentally a Faraday compensator of reciprocal anisotropy in which the compensation is practically independent of the angle of rotation of the Faraday rotator. A diagram of the compensator is shown in Fig. 1. The compensator is a polarization ring interferometer[6] containing a Faraday rotator F. The polarization ring interferometer (PRI) consists of a polarization beam splitter (PBS) and two mirrors m1 and m2. The Jones matrix of a PRI containing an anisotropy element $\hat{M}$ has the form

$$\hat{R} = \begin{vmatrix} 0 & m_{12}^{+} \\ m_{21}^{-} & 0 \end{vmatrix}, \tag{2}$$

where m_{ij} are elements of the Jones matrix $\hat{M}$, and the superscripts $\pm$ correspond to opposite directions of traversing the contour of the PRI. If the anisotropic element $\hat{M}$ is a Faraday rotator with the Jones matrix

$$\hat{M}_F = \begin{vmatrix} \cos\theta & -\sin\theta \\ \sin\theta & \cos\theta \end{vmatrix}, \tag{3}$$

then the Jones matrix of our compensator takes the form

$$\hat{R} = \sin\theta \begin{vmatrix} 0 & 1 \\ -1 & 0 \end{vmatrix}. \tag{4}$$

As was shown in Ref. 1, in a round-trip optical circuit a reflector with the Jones matrix (4) will compensate any reciprocal phase anisotropy in the elements placed in front of it. Aside from the Faraday rotation angle, a compensator based on a PRI is completely equivalent to an ideal conventional 45° Faraday mirror. A deviation of the angle of Faraday rotation from the optimum (45°) will lead only to a decrease of the power returned by the compensator, this effect being due to a decrease in the polarization component of the counterpropagating waves not redirected by the PBS.

The characteristics of a compensator based on a PRI and a conventional 45° Faraday mirror were compared in an experiment using the arrangement shown in Fig. 2. Light from a helium–neon laser (He–Ne) passed through a polarizer (P), a single-mode axisymmetric optical fiber (SMF), reflected off the compensator under study (C), once again passed through the fiber, and was directed through a 50% beam splitter (BS) onto a polarization photodetector consisting of a Wollaston prism (W) having one of its axes oriented parallel to the polarization at the output of the polarizer *P*, and a pair

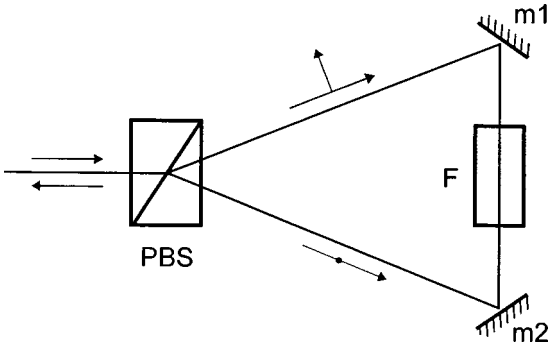

FIG. 1. Diagram of a Faraday compensator based on a polarization ring interferometer. PBS is a polarization beam splitter, m1 and m2 are mirrors, and F is a Faraday rotator.

of photodiodes (PD1, PD2). With a Lefevre polarization controller (PC) we could create any desired phase anisotropy in the fiber. In the case of ideal compensation of the anisotropy in the fiber the polarization at the exit from the fiber (and, accordingly, at the entrance of the photodetector) should be strictly orthogonal to the polarization, produced by polarizer P, at the entrance to the fiber. The fact that a polarization component parallel to the input polarization appears at the entrance of the photodetector is indicative of compensation error. In the experiment we measured the intensity of the orthogonal and parallel components of the polarization after a round-trip passage through the fiber as a function of the angle of Faraday rotation for both types of compensators. At each value of the Faraday rotation angle the Lefevre polarization controller was used to create in the fiber an anisotropy such that the uncompensated component was maximum at each value. It should be noted that, although in our experiment the polarization at the entrance of the round-trip circuit was linear, our data on the quality of the compensation are valid for any input polarization that can be represented as the sum of two linearly polarized components.

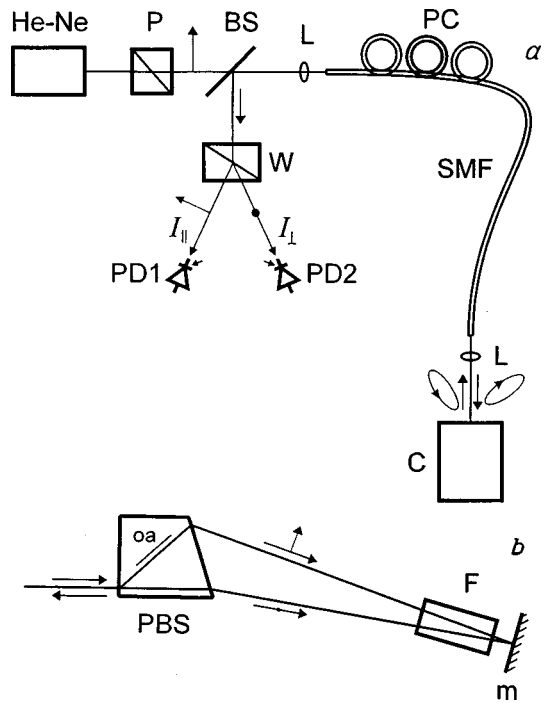

FIG. 2. a: Experimental apparatus for investigating Faraday compensators: He–Ne is a helium–neon laser ($\lambda = 0.63$ μm), P is a polarizer (Glan prism), L is a lens, SMF is a single-mode optical fiber, PC is a Lefevre polarization controller, and C is the compensator under study. b: A compensator based on a polarization ring interferometer: PBS is a polarization beam splitter, m is a plane mirror, and F is a Faraday rotator with an adjustable angle of rotation.

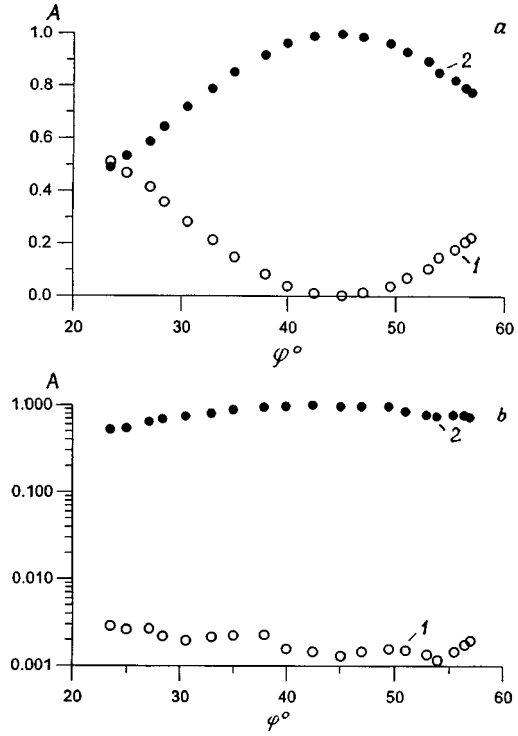

FIG. 3. Quality of compensation versus the Faraday rotation angle φ. *1* — Intensity *A* of the uncompensated (parallel to the initial) component of the output polarization; *2* — intensity of the compensated (orthogonal to the initial) component of the output polarization. a: For a conventional Faraday mirror; b: for a compensator based on a polarization ring interferometer.

A diagram of the compensator used in the experiment is shown in Fig. 2b. The compensator included a polarization beam splitter (PBS), a mirror (M) closing the contour of the PRI, and a Faraday cell (F) having an adjustable angle of rotation of the plane of polarization and mounted directly in front of the mirror. The PBS used was a cleaved Savart plate — a calcite prism cut at an angle to the optic axis. The mirror was mounted at the crossing point of the rays separated by the Savart plate. The Faraday rotator was made in the form of a rod of the magnetooptical glass MOS-31 which could be moved around inside a cylindrical samarium–cobalt permanent magnet. By moving the magnetooptical rod around inside the permanent magnet we could vary the Faraday rotation angle at the working wavelength 0.63 μm from 0 to 60°. The same cell was used in a 45° Faraday mirror.

The results of the measurements are shown in Fig. 3. It is seen that when a PRI-based compensator is used, the quality of the compensation, defined as the ratio of the parallel and orthogonal components of the input polarization, remain high at all Faraday rotation angles, whereas in the case of a conventional 45° Faraday mirror the ratio of the intensities

of the uncompensated and compensated components rises rapidly as one moves away from 45°. It is important to note that even at Faraday rotation angles close to 45° the PRI compensator provides a higher-quality restoration of the polarization than does a 45° Faraday mirror. The residual compensation error is apparently due to imperfection of the Faraday cell and nonideality of the adjustment of the PRI and the photodetector.

The results presented above suggest that compensators of parasitic anisotropy which utilize polarization ring interferometers may find application in various optical circuits, primarily fiber-optic ones, where wideband light or light of several wavelengths is used and where high-quality compensation at all wavelengths is required. It should be noted that this new compensator is amenable to all-fiber implementation with the use of polarization-dependent fiber couplers.

The author thanks E. A. Khazanov for useful comments.

[1] V. M. Gelikonov, D. D. Gusovskiĭ, V. I. Leonov, and M. A. Novikov, Pis'ma Zh. Tekh. Fiz. **13**, 775 (1987) [Sov. Tech. Phys. Lett. **13**, 322 (1987)].
[2] M. Martinelli, Opt. Commun. **72**, 341 (1989).
[3] A. D. Kersey, M. J. Marrone, and M. A. Davis, Electron. Lett. **27**, 518 (1991).
[4] N. Duling and R. D. Esman, Electron. Lett. **28**, 1126 (1992).
[5] C. R. Giles, Electron. Lett. **30**, 976 (1994).
[6] M. A. Novikov, Radiotekh. Elektron. **21**, 904 (1976).

Translated by Steve Torstveit

New type of oscillations in bistable resonant tunneling diodes

B. A. Glavin, V. A. Kochelap, and V. V. Mitin

Institute of Semiconductor Physics, National Academy of Sciences of Ukraine, Kiev;
Wayne State University, Detroit, MI 48202, USA
(Submitted October 9, 1998)
Pis'ma Zh. Tekh. Fiz. **25**, 64–68 (May 26, 1999)

It is shown that that the coupling of resonant tunneling diodes with an external electrical circuit containing an oscillatory loop can lead to the excitation of spatiotemporal oscillations.
 [S1063-7850(99)02705-6]

Resonant tunneling diodes (RTDs) have been the subject of intensive investigations in recent years (see, e.g., Ref. 1). One of the effects commonly observed in RTDs is Z-shaped internal bistability of the current–voltage (I–V) characteristic, arising as a result of the accumulation of the electric charge of the resonant electrons in the quantum well of the RTD.

Recently a new type of transient process in bistable RTDs, due to transverse switching waves, was examined theoretically in Refs. 2 and 3. A switching wave is a nonuniform (in the direction transverse to the current) structure of the resonant tunneling current density. Part of the cross section of the RTD is in a high-current state, and part is in a low-current state (Fig. 1a), and the boundary between these two regions moves along the quantum well with a certain velocity v which depends on the voltage V across the RTD. As we see, the switching wave brings about the switching of the RTD from one uniform state to the other. The type of switching that is possible is also determined by V. Inside the bistable region of voltages $V_l<V<V_h$ there is a certain voltage value V_c for which $v=0$ and the switching wave is a stationary transverse structure. For $V_l<V<V_c$, switching can occur from the low-current to the high-current state, and for $V_c<V<V_h$, from the high-current to the low-current state. Importantly, the switching wave can be excited by excess injection or extraction of resonant electrons near the transverse boundaries of the RTD, which can occur on account of technological nonuniformities (variations of the layer thicknesses in the quantum well and barriers) and also on account of the presence of additional contacts. Thus the low-current branch of the I–V characteristic for $V_l<V<V_c$ and the high-current branch for $V_c<V<V_h$ may become unstable as a result of excitation of a switching wave.

The main result of this study is the finding that when an RTD whose I–V characteristic has a region of instability against the excitation of a switching wave is connected into an external electrical circuit containing an oscillatory loop, a new type of spatiotemporal oscillations can be excited. These oscillations are caused by the fact that the change in the RTD current during the propagation of a switching wave will lead to a change in the voltage across the RTD and in the velocity of the switching wave on account of the reaction of the electrical circuit. The subject of our analysis is the simple electrical circuit illustrated in Fig. 1b. For specificity we assume that the high-current branch of the I–V characteristic for $V_c<V<V_h$ is unstable as a result of the excitation of a switching wave. The stationary states of the system are determined by the intersection of the I–V characteristic of the system and the load line (Fig. 1c). We are interested in the case in which two of these stationary states ($S1$ and $S3$) are homogeneous high- and low-current states, while the third, $S2$, is a stationary structure of the type $V=V_c$. It is easy to see that $S1$ and $S3$ are stable against small perturbations, while $S2$ is unstable. If the system is initially found in state $S1$, then a disturbance that is strong enough for V to become greater than V_c will lead to the excitation of a switching wave. Then there are three possible scenarios for the subsequent evolution of the system: 1) the RTD is completely switched to the state $S3$; 2) the influence of the circuit causes V at some time to become smaller than V_c, so that the switching wave changes its direction of propagation and the RTD reverts to the homogeneous high-current state; 3) after the reversion described in scenario 2 the evolution of the circuit restores the condition $V>V_c$, and the switching wave is excited anew.

As we see, each cycle of oscillations consists of two stages. During the first stage a switching wave propagates in the RTD. In this stage the system is described by the equations

$$\frac{dl}{dt}=-v(V), \quad \frac{d^2U}{dt^2}+\omega_0^2U=\frac{1}{C}\frac{dI}{dt}. \tag{1}$$

Here l is the length of the RTD region found in the high-current state, a positive velocity v corresponds to switching from the high- to the low-current state, U is the voltage across the oscillatory loop, $\omega_0=(L^*C)^{-1/2}$, L^* and C are the natural frequency, inductance, and capacitance of the oscillatory loop, I is the RTD current, which is given by the relation

$$I=(l/L)I^{(h)}(V)+(1-l/L)I^{(l)}(V), \tag{2}$$

where L is the length of the RTD in the direction of propagation of the switching wave, and $I^{(h,l)}$ are the equations of the high- and low-current branches of the I–V characteristic of the RTD. This system of equations must be supplemented with Kirchhoff's law: $IR+U+V=E$, where E is the source voltage. During the second stage the RTD is found in a ho-

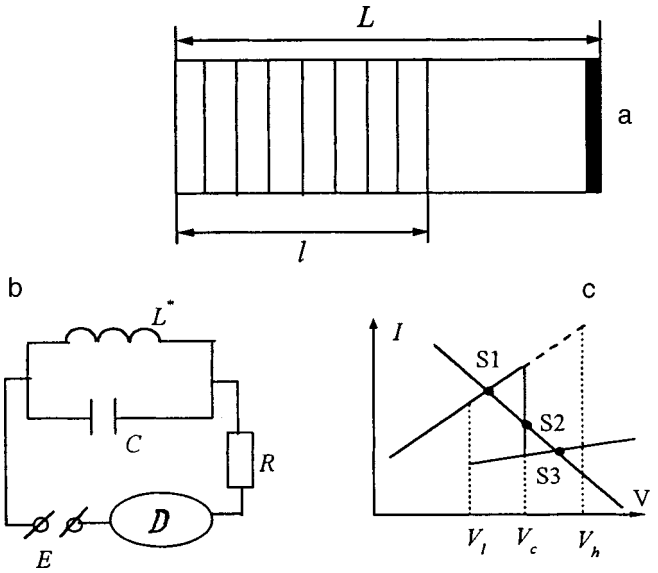

FIG. 1. a: Schematic illustration of the transverse cross section of a resonant tunneling diode (RTD) during the propagation of a switching wave. The shaded part, of length l, is found in the high-current state, while the remainder $L-l$ is in the low-current state. b: The electrical circuit used in the analysis; D is the RTD. c: Stationary states of the system; the Z-shaped I–V characteristic of the RTD and the load line are shown.

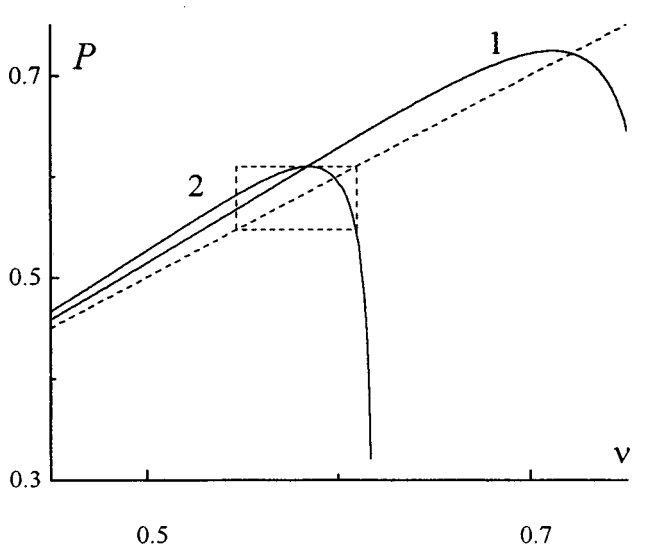

FIG. 2. One-dimensional maps $P(\nu)$ leading to the onset of oscillations. The single straight line $P=\nu$ and the basin of attraction of map *2* are shown by dashed lines.

mogeneous high-current state $l=L$, and the system is described by the second of Eqs. (1). In accordance with what we have said above, each cycle is determined by three initial conditions. Two of them, however, are always the same: at the beginning of the cycle, $l=L$ and $U\equiv U_0=E-V_c-I^{(h)}(V_c)R$. Thus there is actually only one initial parameter, which we define as $\nu=-(\omega_0 U_0)^{-1/2}(dU/dt)(t=0)$. Then the evolution of the whole system is described by a one-dimensional map P which determines the value of ν in the $(n+1)$th cycle according to its value in the nth cycle: $\nu_{n+1}=P(\nu_n)$.

Figure 2 shows two types of maps P that lead to oscillations. Regular oscillations correspond to the fixed points of P, which are defined by the condition $P(\nu)=\nu$. If at a fixed point $|dP/d\nu|<1$, then the fixed point and the oscillations are stable, and the situation corresponds to curve *1* in Fig. 2. Oscillations can also exist when the fixed point is unstable, but the map will have a basin of attraction within which the parameter ν is trapped. This case corresponds to curve *2* in Fig. 2 (the basin of attraction is shown by the dashed rectangle). In the calculations we used linear approximations for v and for the I–V characteristic of the RTD: $v=\beta(V-V_c)$, $I^{(h,l)}=I_0^{(h,l)}+(V-V_c)/R_{h,l}$. Curves *1* and *2* correspond to the following parameters of the RTD and circuit: $\beta(I_0^{(h)}-I_0^{(l)})R/(L\omega_0)=1.3$ and 1.6, respectively, $R_h/R=100$, $R_l/R=1000$, $\omega_0 RC=20$, $l_c/L=0.9$, where l_c is the value of l corresponding to the stationary state $S2$.

Thus we have shown that excitation of a switching wave in bistable resonant tunneling diodes connected to an oscillatory loop can give rise to a new type of spatiotemporal auto-oscillations that do not derive from the presence of negative differential resistance. This effect is largely due to the stability properties of transverse structures in systems with Z-type bistability.[4]

[1] *Proceedings of a NATO Advanced Research Workshop on Resonant Tunneling in Semiconductors: Physics and Applications*, El Escorial, May 14–18, 1990, Plenum Press, New York (1991), 537 pp.
[2] B. A. Glavin, V. A. Kochelap, and V. V. Mitin, Phys. Rev. B **56**, 13346 (1997); Lith. Phys. J. **35**, No. 5–6, pp. 549–551 (1995).
[3] D. V. Mel'nikov and A. I. Podlivaev, Fiz. Tekh. Poluprovodn. **32**, 227 (1998) [Semiconductors **32**, 206 (1998)].
[4] M. Meixner, P. Rodin, and E. Schöll, Phys. Status Solidi B **204**, 493 (1997).

Translated by Steve Torstveit

Temperature effect on the field emission from zirconium islands on tungsten

E. L. Kontorovich, T. I. Sudakova, and V. N. Shrednik

A. F. Ioffe Physicotechnical Institute, Russian Academy of Sciences, St. Petersburg
(Submitted January 14, 1999)
Pis'ma Zh. Tekh. Fiz. **25**, 69–73 (May 26, 1999)

The coefficients α_T of the change in the work function with temperature are determined experimentally for two-dimensional islands of zirconium on and in the vicinity of the {001} face of tungsten. The values of α_T are an order of magnitude higher than those typical for clean metals. The reason is a change in the adatom–adatom binding energy with increasing temperature.
 [S1063-7850(99)02805-0]

Two-dimensional islands of zirconium form in the vicinity of the {001} cube faces of the tungsten crystal and on these faces themselves. These islands appear as bright spots in a field electron microscope.[1,2] Zirconium is ordinarily deposited on cold tungsten in high vacuum. At a temperature $T=1000-1400$ K the zirconium is redistributed over the surface (while not yet diffusing into the interior or evaporating) and accumulates around the faces of the cube. The islands have the greatest contrast if the coverage is low: 0.05–0.1 monolayer. Special experiments[1,3] have demonstrated that these islands are actually flat (a monolayer thick) and not three-dimensional micropyramids, and that their strong field emission is due to a lowering of the work function φ of the surface from 4.4–4.5 eV for the initial clean tungsten to 2.5–3 eV (Ref. 1) for the islands. The islands are small, ordinarily 30–100 Å in size, which is comparable to the resolution of the field electron microscope. An example of these islands is shown in Fig. 1. By varying the temperature one can cause the islands to ''dissolve'' (i.e., evaporate within the confines of the adsorbed layer) and regrow. From the rates of these processes investigators have determined the energies of the interatomic bond in the two-dimensional crystal and the activation energies for the growth and dissolution of the islands.[2,4,5]

A detailed analysis of two-dimensional phase transitions in adsorption systems of this kind, in particular, of the values of the pre-exponential coefficients in the Arrhenius equations governing the kinetics of the transitions, has raised the issue of searching for anomalies in the temperature coefficients of the work function of two-dimensional adsorbed phases.[6] Carrying out such a search in the case of Zr islands on W is the main purpose of the present study. For this we determined experimentally the temperature effect on the field emission from the islands, which was then compared with the known theory of this effect.[7]

Repeated measurements of the emission current from the islands at room temperature and at an elevated temperature lying below the temperature of their formation were carried out in three sealed-off glass devices on three tungsten tips. The vacuum in the devices was at the $10^{-9}-10^{-11}$ torr level, which eliminated the influence of adsorption of residual gases on the measured currents. The amount of Zr initially deposited was varied from 0.05 to 0.5 monolayer. Islands around the {100}W faces were formed at $T\sim 1400$ K. Measurements of the emission currents (within the interval from 1 to 500 nA) were carried out in the temperature interval from room temperature (293 K) to 1330 K. The growth of the emission current with temperature T was significant and measurable starting at 500 K. However, our task was to elucidate the conditions under which and the degree to which this growth exceeded the growth expected according to the Murphy–Good theory.[7]

According to that theory[7] the ratio of the field electron current $I(T)$ at temperature T to its value $I(0)$ at 0 K obeys the following formula in cases when $I(T)/I(0)<10$:

$$I(T)/I(0)=\pi\omega/\sin\pi\omega, \tag{1}$$

where

$$\omega=4\pi\sqrt{2m}\cdot k\sqrt{\varphi}\cdot t(y)\cdot T/he\cdot E, \tag{2}$$

m is the electron mass, k is Boltzmann's constant, φ is the work function, h is Planck's constant, T is the absolute temperature, E is the electric field, and $t(y)$ is a tabulated function which is of the nature of a correction with values close to 1 (see, e.g., Ref. 8).

For φ measured in eV and E in V/cm, if we substitute the value $t(y)\approx t(0.5)=1.044$ from Ref. 8 and the values of all the constants into the above equation, we get

$$\omega\approx 9.22\times 10^3\sqrt{\varphi}\cdot T/E. \tag{3}$$

In practice the minimum current is measured not at 0 K but at room temperature ($T_{\text{room}}=293$ K), and the current $I(T)$ measured at high T is taken in ratio to it. The experiments are carried out at the same value of E, and to a first approximation it is assumed that φ does not change as T is increased.[1)] Then

$$I(T)/I(T_{\text{room}})=T\cdot\sin\pi\omega_{\text{room}}/T_{\text{room}}\cdot\sin\pi\omega_T, \tag{4}$$

where ω_{room} and ω_T are the values of ω at T_{room} and T, respectively. For convenience in comparing the measured and calculated ratios $I(T)/I(T_{\text{room}})\equiv D(T)$ we have calculated detailed tables of D as a function of T and of the parameter $P=(\sqrt{\varphi}/E)\times 10^7$ (with φ in eV and E in V/cm).

Measurements of D for strongly emitting spots on and around {001}W revealed that for none of these Zr formations does the temperature effect on emission fall outside the the-

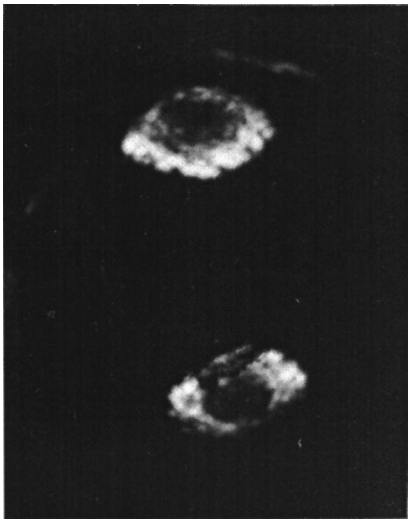

FIG. 1. Field electron image of Zr islands in the vicinity of a {001} cube face of a W single crystal. The Zr, in an amount of about 0.1 monolayer, was deposited on the W at room temperature and then redistributed by heating to 1300–1400 K. The picture was taken at a temperature of the W tip of $T=1000$ K, at a voltage $V=3790$ kV and an emission current of 40 nA. The scale is specified by the distance between centers of the {001} faces, which was around 5000 Å.

oretical range. An effect slightly in excess of (4) was observed both for the low-contrast islands ($\varphi \approx 4.2$ eV) formed at low coverages in the initial stages of island formation and also for the overdense, continuous-looking formations around the {001} poles at relatively high coverages (0.3 monolayer and higher). A strong temperature effect was observed for the islands with high contrast in φ (with φ from 2.5 to 3 eV), formed in the heating of the deposit from an initial concentration of 0.05–0.15 monolayer (this is the type shown in Fig. 1). For such islands D exceeded the calculated value, depending on the parameters φ, E, and T, by a factor of N, where N varied from 1.2 to 4.9 in the cases recorded here.

The excess growth of D was related to the lowering of φ with increasing temperature, and for the known value of E the Fowler–Nordheim theory[8] was used to find the depression of the work function φ_T, and then by dividing the change in φ ($\Delta\varphi$) by the temperature interval $\Delta T = T - T_{\text{room}}$ we obtain the temperature coefficient α_T of the work function:

$$\alpha_T = (\varphi_T - \varphi_{\text{room}})/\Delta T, \tag{5}$$

where φ_T and φ_{room} are the work functions at T and T_{room}, respectively.

A similar calculation was done for new measurements of D in ΔT intervals from 500 to 1000 deg and also for the measurements of D made in Ref. 3, over intervals of 200–400 deg. All of these calculations gave coefficients α_T an order of magnitude greater than the typical values of α_T for metals, which lie around 10^{-5} eV/deg.[9] For islands with work functions φ from 2.5 to 3 eV, for ΔT from 500 to 1000 deg the coefficient α_T was $-(1.6\text{–}2.2)\times 10^{-4}$ eV/deg. For islands with φ from 2.5 to 4 eV, for ΔT of 300–400 deg we obtained $\alpha_T = -(3\text{–}7.5)\times 10^{-4}$ eV/deg.

In summary, it is those two-dimensional crystals of Zr on W which undergo reversible two-dimensional phase transitions, exhibiting ''nontheoretical'' pre-exponential factors in the Arrhenius equations, that have anomalously high negative coefficients α_T. This confirms the idea that an important role is played by the redistribution of bonds in the adatom–adatom adatom–substrate system as the crystal undergoes thermal expansion.[6] This redistribution gives an appreciable contribution to the lowering of the energy of the Zr–Zr interatomic bonds in the two-dimensional islands as the temperature is raised.

This study was supported by the Russian Fund for Fundamental Research, Project No. 97-02-18066.

[1)] If the change of φ with T is then taken into account, this will give only a small correction to the values of α_T presented at the end of this paper.

[1] V. N. Shrednik, Fiz. Tverd. Tela (Leningrad) **3**, 1750 (1961) [Sov. Phys. Solid State **3**, 1286 (1961)].
[2] V. N. Shrednik and G. A. Odishariya, Izv. Akad. Nauk SSSR, Ser. Fiz. **33**, 536 (1969).
[3] V. N. Shrednik, Fiz. Tverd. Tela (Leningrad) **1**, 1134 (1959) [Sov. Phys. Solid State **1**, 1037 (1959)].
[4] G. A. Odishariya and V. N. Shrednik, Dokl. Akad. Nauk SSSR **182**, 542 (1968).
[5] B. K. Vaĭnshteĭn and A. A. Chernov (eds.), *Problems of Modern Crystallography* [in Russian], Nauka, Moscow (1975), pp. 150–171.
[6] V. N. Shrednik, Pis'ma Zh. Tekh. Fiz. **24**(11), 34 (1998) [Tech. Phys. Lett. **24**(6), 427 (1998)].
[7] E. L. Murphy and R. H. Good, Phys. Rev. **102**, 1464 (1956).
[8] M. I. Elison (ed.), *Cold Cathodes* [in Russian], Sov. Radio, Moscow (1974), pp. 166–173.
[9] L. N. Dobretsov and M. V. Gomoyunova, *Emission Electronics* [in Russian], Nauka, Moscow (1966).

Translated by Steve Torstveit

Global reconstruction from nonstationary data

N. B. Yanson, A. N. Pavlov, T. Kapitaniak, and V. S. Anishchenko

Saratov State University;
Technical University, Lodz, Poland
(Submitted January 20, 1999)
Pis'ma Zh. Tekh. Fiz. **25**, 74–81 (May 26, 1999)

One-dimensional time series of a dynamical system with slowly varying parameters are investigated. For estimation of the characteristics of the attractors of such a system which exist for fixed values of the parameters, it is proposed to ''cut out'' from the time series short segments that belong to the individual attractors and to use them to reconstruct a model dynamical system. © *1999 American Institute of Physics.* [S1063-7850(99)02905-5]

Papers in which dynamical systems are analyzed from one-dimensional time series as a rule have the goal of estimating the characteristics of the operating regimes of the systems, specifically, to calculate the power spectra and moment functions and to determine the geometric and dynamic characteristics of the attractors, etc. One of the most complicated problems is to predict the future behavior of the system and to construct a mathematical model describing the evolution of its state (the problem of global reconstruction).

An algorithm for global reconstruction of a dynamical system from one-dimensional times series was first proposed in 1987.[1,2] In recent years the technique of modeling from experimental data has been discussed in a number of papers: various modifications of the global reconstruction method have been developed,[3–5] and several original approaches to the problem have been implemented.[6,7]

Since most of the algorithms hitherto developed for solving the aforementioned problems are applicable to stationary signals, it is ordinarily assumed that the time series is generated by a finite-dimensional dynamical system with constant parameters,

$$d\mathbf{x}/dt=\mathbf{F}(\mathbf{x},\boldsymbol{\mu}),\quad \mathbf{x}\in R^n,\quad \boldsymbol{\mu}\in R^m, \tag{1}$$

in which the investigated processes are assumed stationary.

However, if real experimental signals are being analyzed, especially signals of biological origin, such an assumption is not always justified, since the initial objects are open systems, subject to the influence of the surrounding medium. Such systems, on account of the presence of feedback, generally function in a regime of adaptation to changes in the external conditions. The signals generated by them are nonstationary, and the adaptation process can often be interpreted as a variation of the parameters of the system in time.

In this paper we consider the possibility of applying the technique of reconstruction to a one-dimensional time series of a dynamical system with slowly varying parameters for the purpose of determining the dependence of the characteristics of the attractors of the systems on the values of the control parameters.

Suppose that $\boldsymbol{\mu}=\boldsymbol{\mu}(t)$ in the dynamical system (1). Let us make several assumptions under which we will solve the stated problem:

1) the function $\boldsymbol{\mu}(t)$ is oscillatory;

2) for simplicity we restrict consideration to the case of one-parameter modulation, i.e., $\mu_j=\mu_j(t)$, $\mu_k(t)=\text{const}$, $k=1,\ldots,m, k\neq j$;

3) the parameters vary slowly not only in comparison

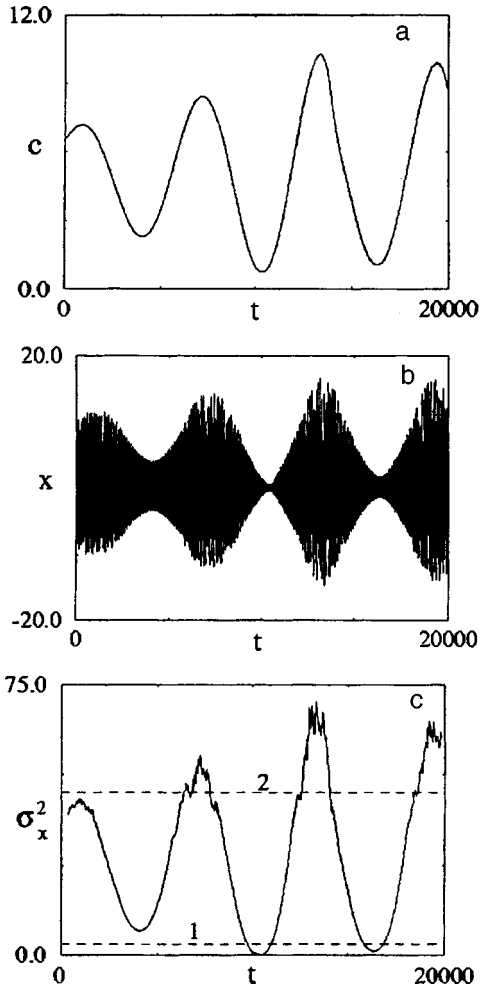

FIG. 1. a: Modulation of the parameter c of the Rössler system; b: corresponding time dependence $x(t)$; c: time dependence of the variance calculated from the signal (b) within a time window that is shifted along the time series.

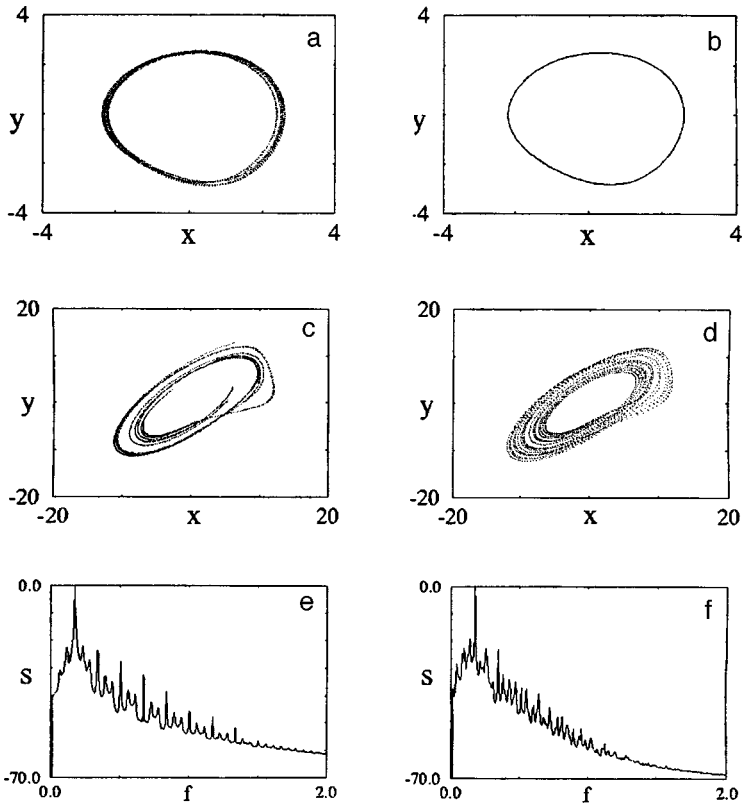

FIG. 2. a,c: Phase trajectories reconstructed from short segments of the time series in Fig. 1b and corresponding to levels *1* and *2* in Fig. 1c; b,d: attractors of the dynamical systems reconstructed from the given phase portrait. The parameters of the reconstruction for Fig. 2 are as follows: a,b — dimension of the embedding space $n=3$, the right-hand sides were approximated by third-degree polynomials, and the coordinates were reconstructed by the method of successive differentiation;[11] c,d — dimension of the embedding space $n=4$, the right-hand sides were approximated by third-degree polynomials here also, but the coordinates were reconstructed by the delay method; e — the power spectrum calculated from the x coordinate of the Rössler system at the value of the parameter corresponding to level *2* in Fig. 1c; f — power spectrum calculated from the solution of the reconstructed model system.

with the period of the base frequency of the oscillations of the system under study but also in comparison with the duration of the transient processes, so that one can neglect the inertial properties of the system;

4) the system does not exhibit multistability phenomena, i.e., for identical values of μ it functions in the same dynamical regime.

These assumptions allow us to assume that at times when the parameters of the system take on the same values, the phase transitions belong to the same attractor. We will discuss the meaning of the fourth assumption, which may not be necessary, below.

We note that we are analyzing only a time series generated by a system with varying parameters and do not have information about the concrete form of the evolution equations of the system or about the character of the time dependence of $\mu(t)$.

As an example, let us model the given situation with the well-known Rössler model:[8]

$$\frac{dx}{dt}=-(y+z), \quad \frac{dy}{dt}=x+ay, \quad \frac{dz}{dt}=b+z(x-c),$$

$$a=0.15, \quad b=0.2, \tag{2}$$

where the parameter c varies in an irregular way (Fig. 1a) on the interval.[1–12] On this interval a transition occurs from a one-cycle to a regime of chaotic oscillations through a cascade of period-doubling bifurcations. The relation between the mean modulation period of the parameter and the base period of the auto-oscillations $x(t)$ was chosen to be of the order of 1000:1. The observed time series (Fig. 1b) is nonstationary.

We choose the time window for the signal $x(t)$ so as to be long enough to encompass several periods of the observed time series but short enough that the parameters of the system can be considered approximately constant during this time interval. We will determine the character of the parametric modulation. For this we will calculate the moments for segments of the time series inside a time window 50 dimensionless time units long (encompassing approximately 8 periods of the oscillations).[1)] By shifting the window along the signal, we construct the time dependence of these moments. Obviously a changeover of the regime of functioning of the system will not lead to a change of all the moments simultaneously. For example, for the time series in Fig. 1b the mean value does not change as the control parameter is varied. However, one can always find moments which will react to a changeover of regime, and for the time series under study the variance is one of those (Fig. 1c). The behavior of this graph qualitatively reproduces the function $c(t)$ (Fig. 1a).

Let us now consider two levels corresponding to two different values of the variance (Fig. 1c), which, as we assume, correspond to two fixed values of the parameter c. In an actual calculation with real signals we will not know the values of the control parameters of the system and will only assume that each set of them corresponds to some value of the moment. However, for the modeled situation we know that the lower level (line *1*) corresponds to a one-cycle limit cycle, while the upper level (line *2*) corresponds to a chaotic regime.

We choose small neighborhoods of the points (the size of the neighborhood is about one period of the oscillations)

in which each chosen level crosses the time dependence of the variance. We ''cut out'' the corresponding segments of the time series for these neighborhoods and apply to them the standard embedding technique, e.g., the delay method or the method of successive differentiation.[9–11] The results of the reconstruction of the phase portrait for such segments for the two different levels are shown in Figs. 2a and 2c, respectively. The segments of the phase trajectories do not ''meet up'' with one another and are rather short, but we assume that they belong to the same attractor (the regular and the chaotic, respectively).

Since the number of state vectors reconstructed by this method may be quite small and, moreover, the reconstructed segments of the phase trajectories do not ''meet up,'' the application of the standard method of signal processing, such as calculation of the autocorrelation function, power spectrum, Lyapunov exponents, etc., to these data is problematical. At the same time, employing the technique of global reconstruction presupposes only knowledge of a set of state vectors at discrete times and their time derivatives (here the length of the signal may be relatively short)[12,13] and does not impose any requirements on the continuity of the phase trajectory. Let us illustrate the application of the given algorithm to the phase portraits shown in Figs. 2a and 2c (the parameters of the algorithm are given in the captions).

Figures 2b and 2d show the attractors corresponding to the reconstructed models. Then, having obtained a dynamical description of the necessary regime, one can by numerical integration generate a phase trajectory of arbitrary duration and calculate from it the characteristics of the attractors by standard algorithms. In particular, the maximum Lyapunov exponent λ_1 calculated for the chaotic attractor of the Rössler system by the method of Ref. 14 for $c \approx 8.0$ and corresponding to level *2* in Fig. 1d, has a value ≈ 0.065. The Lyapunov exponent calculated by the same method from the equations of the model system obtained for level *2* is ≈ 0.052, somewhat less than its ''true'' value. For comparison, in Figs. 2e and 2f we show the power spectra of the initial chaotic attractor of system (2) and of the chaotic attractor of the corresponding reconstructed system.

In summary, with the multiwindow reconstruction procedure discussed in this paper, by shifting the straight lines *1* and *2* in Fig. 1c one can track the evolution of the characteristics of the regimes of functioning of a dynamical system with slowly varying parameters from a one-dimensional time series.

We note in closing that the technique described above is applicable under conditions where the system under study does not exhibit multistability and the related hysteresis. If this is not the case, then the time dependences of the moment functions will not reproduce the law of modulation of the parameters. However, since the moments characterize the regime of oscillations and not the values of the parameters, we assume that this technique will permit reconstruction of the necessary attractors even in that case, but this question will require a separate detailed investigation.

The research reported was supported in part by INTAS Grant 96-0305 and by the Korolev Society of London.

[1)] To calculate the moment functions of the random process one needs to know its distribution densities. However, by making the assumption that the process under study is stationary over the chosen time segment (we assume that the oscillations occur at an attractor) and ergodic, one can replace the averaging over an ensemble of time series by a time average. For calculations to high accuracy in averaging over time it is necessary that the time series be long. Here, with short time series, we can evaluate the moments only approximately, and that will lead to choppiness of the graphs of their ''time'' dependence (Fig. 1c).

[1] J. Cremers and A. Hübler, Z. Naturforsch., A: Phys. Sci. **42**, 797 (1987).
[2] J. P. Crutchfield and B. S. McNamara, Complex Syst. **1**, 417 (1987).
[3] J. L. Breeden and A. Hübler, Phys. Rev. A **42**, 5817 (1990).
[4] G. Gouesbet and J. Maquet, Physica D **58**, 202 (1992).
[5] G. Gouesbet and C. Letellier, Phys. Rev. E **49**, 4955 (1994).
[6] R. Hegger, M. J. Bünner, H. Kantz, and A. Giaquinta, Phys. Rev. Lett. **81**, 558 (1998).
[7] H. Voss and J. Kurths, Phys. Lett. A **234**, 336 (1997).
[8] O. E. Rössler, Phys. Lett. A **57**, 397 (1976).
[9] N. H. Packard, J. P. Crutchfield, J. D. Farmer, and R. S. Shaw, Phys. Rev. Lett. **45**, 712 (1980).
[10] F. Takens, in *Dynamical Systems and Turbulence, Warwick 1980*, edited by D. Rang and L. S. Young (Vol. 898 of Lecture Notes in Mathematics), Springer-Verlag, Berlin, pp. 366–381.
[11] J. L. Breeden and N. H. Packard, Int. J. Bifurcation Chaos Appl. Sci. Eng. **4**, 311 (1994).
[12] A. N. Pavlov, N. B. Yanson, and V. S. Anishchenko, Pis'ma Zh. Tekh. Fiz. **23**(8), 7 (1997) [Tech. Phys. Lett. **23**(4), 297 (1997)].
[13] A. N. Pavlov, N. B. Yanson, T. Kapitaniak, and V. S. Anishchenko, Pis'ma Zh. Tekh. Fiz. **25**, No. 10 (1999) [*sic*].
[14] A. Wolf, J. B. Swift, H. L. Swinney, and J. A. Vastano, Physica D **16**, 285 (1985).

Translated by Steve Torstveit

On the magnetization of solar convective zones

Yu. V. Vandakurov

A. F. Ioffe Physicotechnical Institute, Russian Academy of Sciences, St. Petersburg
(Submitted January 28, 1999)
Pis'ma Zh. Tekh. Fiz. **25**, 82–88 (May 26, 1999)

The condition of minimum entropy production has been used previously by the author [see Yu. V. Vandakurov, *Proceedings of the SOHO 6/GONG 98 Workshop*, Boston (1998), Vol. 1, pp. 567–571; *Conference on the New Activity Cycle of the Sun* [in Russian], St. Petersburg, Pulkovo (1998); Zh. Tekh. Fiz. (1999) [in press]] to find the rotation of stellar convective zones and, in particular, to find the latitude distribution of the rotation near the Sun. It turns out, however, that the self-excitation of even very slow meridional flows of the medium leads to ''smearing'' of the entropy-production minima that were considered in the papers cited. In the presence of a toroidal magnetic field the ''smearing'' effect is eliminated. In the case of rotation of the solar type the necessary field is of the order of 10 kG, which can apparently be reconciled with the magnetic fields in bursts on the Sun. © *1999 American Institute of Physics.* [S1063-7850(99)03005-0]

It is known that many of the phenomena observed on the Sun are magnetic-field related. It is generally believed that the magnetic fields are generated in the interaction with a differentially rotating plasma, although the mechanism of generation still remains unknown. In this regard it is of interest to take a new approach to the problem of studying any directed motions of the medium in the stellar convective zones, an approach based on the use of the minimum property of the entropy production.[1–3] Essentially, in the case of an adiabatic convective zone the main forces (per unit mass) are potential forces, and therefore the solenoidal components of such forces as the Coriolis or magnetic force must be counterbalanced by the corresponding component of the viscous force. In particular, an order-of-magnitude estimate shows that in order to maintain the observed solar rotation it is necessary to generate a very strong turbulent viscosity, exceeding the molecular viscosity by 14 orders of magnitude. Since viscosity is a source of entropy production, the latter is markedly increased.

The hypothesis that the interaction with the convective motions causes the distribution of the rotation in the convective zone to be established in accordance with the condition of minimum entropy production, i.e., the condition of smallest $\overline{\epsilon}$ (where $\overline{\epsilon}$ is a dimensionless quantity characterizing the average turbulent viscosity of the medium over the convective zone), can be used to find, among the many possible solutions, a solution which satisfactorily describes the observed latitude distribution of the solar rotation.[1–3] The characteristic radial gradient of the rotational modes, which is proportional to a certain quantity α, is also determined. Here and below we assume that the dependence on the radius r for all the modes with dimensions of velocity is given by a factor r^{α}, where $\alpha = \text{const}$. For the investigated rotation of the medium the parameter α is close to unity, i.e., the rotation is close to rigid-body. It is convenient to study the various equilibrium configurations for different values of this parameter.

However, when the other modes responsible for excitation of slow meridional flows of the medium are included among the variables to be varied, an unexpected result emerges: Despite the small value of the meridional velocities (in the case of minimum $\overline{\epsilon}$ investigated here they were less than 10 cm/s, which is 4 orders of magnitude less than the equatorial velocity of the solar rotation), their influence on the distribution of the minima of $\overline{\epsilon}$ turned out to be extremely substantial. While rough calculations attest to the existence of many such intervals of α within which $\overline{\epsilon}$ decreases quite strongly, when the boundaries of these intervals are refined they ''smear out'' and vanish altogether, except for a single solution with the minimum $\alpha = 1$, corresponding to rigid-body rotation of the medium. This ''smearing out'' of the minima can also occur in the absence of meridional flows if the number N of effectively interacting rotational modes is sufficiently small. In that case, however, instead of the expected minimum we usually obtain an extremely close to neutral state with a small value $\overline{\epsilon}(\alpha) \approx \text{const}$.

Since rigid-body rotation of the convective zone does not agree with the data of solar observations, in finding states with minimum values of $\overline{\epsilon}$ we are forced to take into account the current motions leading to generate of the magnetic field. We restrict consideration to a steady-state equilibrium model with a toroidal magnetic field that is antisymmetric about the equatorial plane. Such a symmetry of the field follows from the aforementioned observational data. Our problem is to find the values of the coefficients of an expansion of the field **B** and velocity **v** in a series in vector spherical harmonics, by minimization of $\overline{\epsilon}$. As in Ref. 3, we consider the problem in the approximation of a thin convective zone, where the radial dependence of the hydrodynamic and Alfvén velocities are assumed to be proportional to $\text{const} \cdot r^{\alpha}$, and the equilibrium density ρ is written approximately as $\text{const} \cdot r^{-\beta}$, where α

and β are constants. In this case the toroidal coefficient of the field $B_{J0}^{(0)}$ is equal to $\text{const}\cdot r^{(\alpha-\beta/2)}$.

It is not hard to show that when the toroidal magnetic field is taken into account in the basic equations (9) and (10) of Ref. 3, only the term $A^J_{J_1J_2}$ in Eq. (10) of that paper will change, and it will be replaced by $A^J_{J_1J_2}-H^J_{J_1J_2}$. Here

$$A^J_{J_1J_2}=[(\alpha+1)I^2Z^J_{J_1J_2}+2\alpha I_1^2Z^{J_1}_{JJ_2}]v^{(0)}_{J_10}v^{(0)}_{J_20} \tag{1}$$

and

$$H^J_{J_1J_2}=[(\alpha+1-\beta/2)I^2Z^J_{J_1J_2}+2\alpha I_1^2Z^{J_1}_{JJ_2}]B^{(0)}_{J_10}B^{(0)}_{J_20}/(4\pi\rho), \tag{2}$$

and the rest of the notation is the same as in Ref. 3. In the case of a rotation of the medium which is symmetric about the equatorial plane and an antisymmetric field distribution, the coefficients J_1 and J_2 in Eq. (1) are odd, while in Eq. (2) they are even. Then the number J is even. For the discussion that follows we introduce the notation

$$u_J=u_{2k-1}=v^{(0)}_{J0}/v^{(0)}_{10}, \quad f_J=f_{2k}=v^{(-1)}_{J0}/[iv^{(0)}_{10}],$$
$$b_J=b_{2k}=B^{(0)}_{J0}/[v^{(0)}_{10}(4\pi\rho)^{1/2}], \tag{3}$$

where $v^{(0)}_{10}=-ir\Omega(8\pi/3)^{1/2}$, k is equal to 1,2, . . . ,N, with N the number of modes (the same for all variables); Ω is a real quantity which would be equal to the angular velocity of rotation if only the first rotation mode were nonzero; the number J is expressed in terms of k in accordance with the parity that follows from Eq. (3).

We assume that N and β are known quantities, and we set out to find those values of the coefficients u_J, f_J, b_J, and α for which $\bar{\epsilon}$ reaches a minimum. The actual procedure of finding the solution is similar to that described in Ref. 3, only a larger number of coefficients are varied. Among the possible configurations we pay particular attention to those which characterize rotation similar to that observed on the Sun. In other words, only models that are rather close to rigid-body rotation are considered.

It turns out that in the presence of a magnetic field the aforementioned ''smearing out'' of the minima vanishes, and a transition to a neighboring solution will occur if α changes by approximately 2%. Two computational models with $N=4$ and $\beta=10$ and 50 are given in Table I. For the solar model of Guenther *et al.*,[4] at these values of β the relative radius (in units of the solar radius) and the density of the layer under consideration are equal to 0.85, 0.04 g/cm^3 and 0.96, 0.004 g/cm^3, respectively. The coefficients of the radial velocity f_J are not given in Table I, since they turned out to be zero. In contradistinction to this, the field contribution almost completely counterbalances the contribution due to the rotation of the medium (replacing the field by zero would increase $\bar{\epsilon}$ to a quantity of the order of 10^{-2}). We also note that the sign of the field is arbitrary, i.e., the sign in front of all the coefficients b_J can be changed to the opposite.

The latitude dependence of the angular velocity of rotation, expressed as a ratio to the equatorial angular velocity, is shown in Fig. 1 by the solid curve and the dashed curve, respectively, for models 1 and 2 of Table I. The crosses in Fig. 1 represent experimental data obtained by Doppler measurements.[5] The helioseismological results of Birch and Kosovichev,[6,7] which pertain to depths with relative radius greater than 0.96, are shown by the vertical bars, the lengths of which characterize the scatter in the data. It is seen that the theoretical curves satisfactorily describe the observational data, and they may also explain the recently observed strong decrease of the angular velocity of rotation at high latitudes. We note, by the way, that the curves shown in Fig. 1 are rather close to the curve corresponding to the nonmagnetic case for $N=5$ and $\alpha=1.27914$.

TABLE I. Model parameters

Model No.	1	2
Number of modes	4	4
β	10	50
α	1.295910	1.291355
u_1	1	1
u_3	−0.0535370	−0.0534743
u_5	−0.0119636	−0.0115274
u_7	−0.0033672	−0.0026194
b_2	0.0295428	0.0150941
b_4	0.0151412	0.0052541
b_6	0.0084693	0.0023948
b_8	0.0046572	0.0010049
$\bar{\epsilon}$	6×10^{-9}	9×10^{-9}

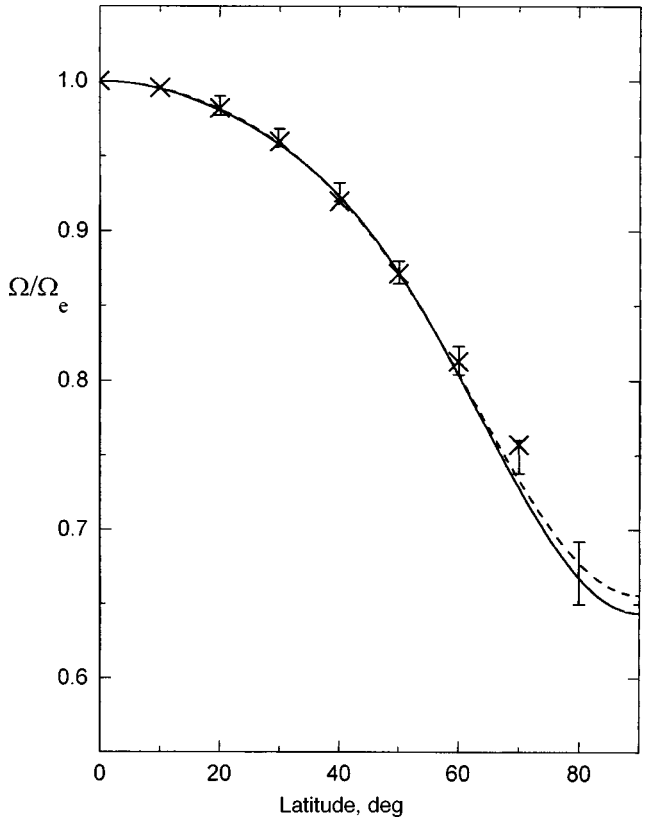

FIG. 1. Dependence on latitude (in degrees) of the angular velocity of rotation Ω, normalized by the angular velocity Ω_e at the equator, for models 1 and 2 of Table I (the solid and dashed curves, respectively). The crosses and vertical bars represent the experimental results of Ref. 5 and Refs. 6 and 7, respectively.

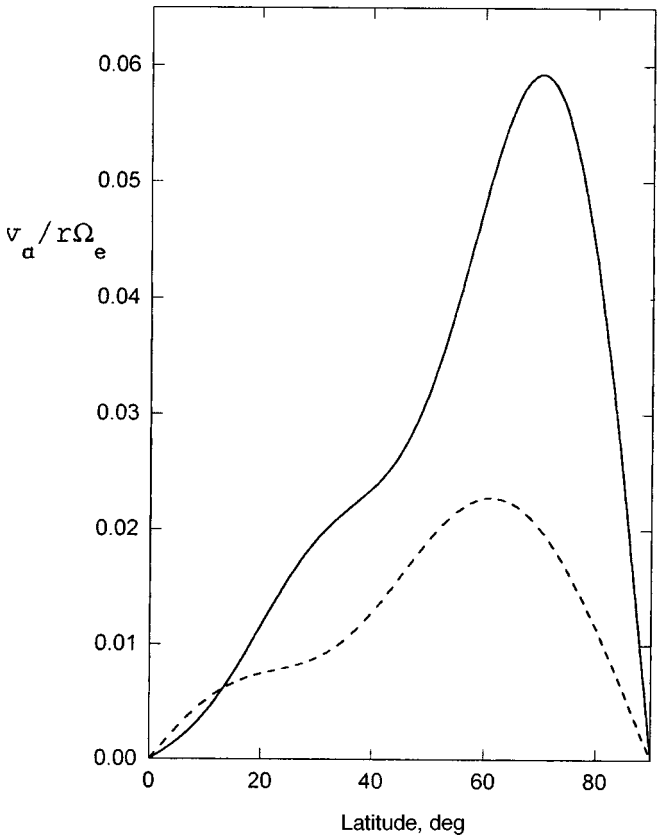

FIG. 2. Latitude distribution of the Alfvén velocity v_a, renormalized by the equatorial velocity $r\Omega_e$, for the same models as in Fig. 1.

The distribution for a magnetic field that is antisymmetric about the equatorial plane is shown in Fig. 2 by the solid and dashed curves, respectively, for models 1 and 2 of Table I. Here $v_a = B_\varphi / [4\pi\rho]^{1/2}$ is the Alfvén velocity, which we have normalized by the equatorial velocity $\tau\Omega_e$. The maximum values of the field for the same models 1 and 2 are approximately 8 and 1 kG. It is seen that the equilibrium magnetic field increases with depth and can reach values of 15 kG in the deepest layers of the solar convection zone. These field values are not inconsistent with the fact that the induction in bursts of the solar field is considerably less than 10 kG.

Thus our calculations definitely argue in favor of the view that the state with the lowest entropy production in the solar convective zone can be reached only in the presence of a magnetic field of around 10 kG. In the approximation of a thin convective zone and a toroidal field a steady-state equilibrium configuration of the field and rotation is possible. However, in the case of the Sun this approximation is extremely crude, so that unsteady processes will also be excited. In order to study the latter it will be necessary to consider more-exact equations.

This study was done with the financial support of the Fund of the St. Petersburg Education and Science Center of the Ministry of Education of the Russian Federation and the Russian Academy of Sciences for ''Electrophysics of High-Density Currents and High Magnetic Fields.''

[1] Yu. V. Vandakurov, *Proceedings of the SOHO 6/GONG 98 Workshop*, Boston (1998), Vol. 1, pp. 567–571.
[2] Yu. V. Vandakurov, *Conference on the New Activity Cycle of the Sun* [in Russian], St. Petersburg, Pulkovo (1998).
[3] Yu. V. Vandakurov, Zh. Tekh. Fiz. (1999) [in press].
[4] D. B. Guenther, P. Demarque, Y.-C. Kim, and M. H. Pinsonneault, Astrophys. J. **387**, 372 (1992).
[5] R. Howard, Annu. Rev. Astron. Astrophys. **22**, 131 (1984).
[6] A. C. Birch and A. G. Kosovichev, Astrophys. J. Lett. **503**, L187 (1998).
[7] A. C. Birch and A. G. Kosovichev, *Proceedings of the SOHO 6/GONG 98 Workshop*, Boston (1998), Vol. 2, pp. 679–684.

Translated by Steve Torstveit

Salient features of using a free-electron laser with a crossed fluted cavity for generating coherent tunable gamma radiation

F. F. Baryshnikov, V. V. Perebeĭnos, and N. V. Cheburkin

GP OKB ''Granat,'' Moscow
(Submitted November 27, 1998)
Pis'ma Zh. Tekh. Fiz. **25**, 89–94 (May 26, 1999)

A new way of generating high-power tunable coherent gamma radiation in a free electron laser with a crossed fluted cavity is proposed. The gamma rays are generated in the inverse Compton scattering of intracavity radiation on the electron beam of the free-electron laser. The use of a crossed fluted cavity makes it possible to raise substantially the intracavity power and thereby the power of the gamma radiation and also to solve the problem of extraction of the hard radiation while eliminating the hitherto unavoidable losses in passage through the material of the cavity mirror. © *1999 American Institute of Physics.* [S1063-7850(99)03105-5]

INTRODUCTION

Coherent, frequency-tunable sources of gamma and x rays are needed for various applications. Such sources may find use for research in solid-state and nuclear physics and in medicine, both for diagnostic purposes (tomography) and for precision irradiation of tumors, since coherent radiation is more easily focused and better absorbed in the place where it is needed.

The possibility of generating coherent gamma and x radiation in the inverse Compton scattering of laser photons on a relativistic electron beam was first analyzed in Refs. 1 and 2. The wavelength λ_X of the hard radiation for $\gamma \gg 1$ is given by the expression[3]

$$\lambda_X \approx \frac{\lambda_L}{4\gamma^2}(1+\gamma^2\theta^2), \tag{1}$$

where λ_L is the wavelength of the laser radiation, γ is the electron energy in units of mc^2, m and c are the electron mass and the speed of light, respectively, and θ is the observation angle measured from the direction of motion of the electron beam.

In Ref. 4 it was proposed for the first time to use intracavity inverse Compton scattering of free-electron laser (FEL) radiation on the beam electrons of the laser itself for generating frequency-tunable gamma rays. Not only could the hard radiation be tuned in frequency over a wide range but would also be polarized. The frequency of the gamma radiation is given by the following relation, which is a generalization of Eq. (1):

$$\lambda_X \approx \frac{L}{8\gamma^4}\left(1+\frac{K^2}{2}\right)(1+\gamma^2\theta^2), \tag{2}$$

where L is the period of the undulator and K is the undulator parameter.

Since that time there have been several demonstration experiments which have confirmed the main theoretical estimates. Let us discuss in greater detail one of the more recent such experiments,[5] which used an infrared FEL with wavelength tunable over the interval 3.5–7.0 μm. The peak current of the linear rf accelerator was equal to 100 A in an electron micropulse 8 ps long. A macropulse 11 μs long was filled with micropulses separated by 16 ns, so that the optical cavity, 4.8 m long, contained 2 micropulses of the electron and (accordingly) light beams. The collision of the electron micropulse ($\gamma \approx 100$) and backward-propagating light micropulse at the center of the cavity led to the generation of x rays with energy in the range 7–14 keV.

To decrease the absorption of the hard radiation, one of the mirrors of the cavity was made of beryllium, and the central part of the mirror, a region 12 mm in diameter, was thinned down to 1.7 mm. To decrease the loss of infrared radiation the surface of the beryllium mirror was additionally coated by a layer of gold 100 μm thick.

In Ref. 5 the number of gamma rays N_X was estimated from the approximate formula

$$N_X \approx 22.7 N K^2 \gamma^2 \theta^2 q, \tag{3}$$

where $K = 0.934 B_0[T]\lambda_{\mathrm{FEL}}(\mathrm{cm})$, B_0 is the peak field of the electromagnetic wave, λ_{FEL} is the wavelength of the free-electron laser, N is the number of periods of the electromagnetic wave, θ is the observation angle in mrad, and q is the charge of the electrons in nC. Since $K^2 \propto J_{\mathrm{FEL}}(\mathrm{W/cm^2})$ and N is proportional to the length of the wave, it follows that N_X is proportional to the laser energy and not to the peak power.

For the given parameters a calculation according to Eq. (3) gives the following values for the number of photons of the hard radiation:[5] 4×10^2 for a micropulse, 2×10^5 for a macropulse, and $5\times10^6\ \mathrm{s}^{-1}$ for a macropulse repetition rate of 25 Hz.

The experimental results obtained in Ref. 5 turned out to be around an order of magnitude lower than the quoted numbers, and the shortfall was attributed by the authors mainly to a decrease in the intracavity intensity on account of degradation of the gold coating by the high-power infrared radiation (the loss per pass reached 6%) and also to the partial absorp-

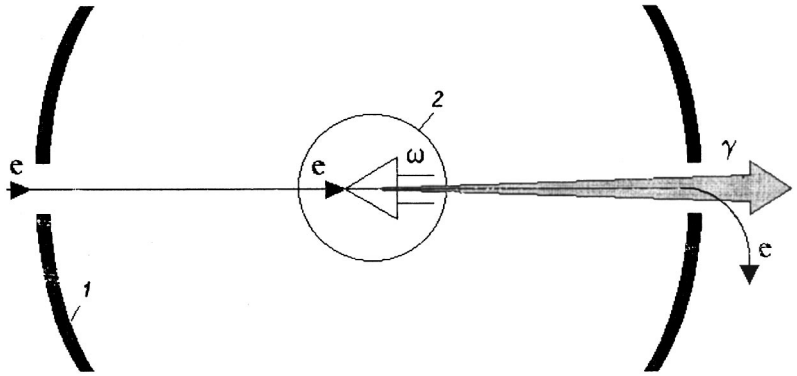

FIG. 1. Schematic illustration of the generation of gamma rays in inverse Compton scattering in a crossed fluted cavity of a free-electron laser: *1* — mirror, *2* — interaction region.

tion of the hard photons in the cavity mirror. We note also that for prolonged operation there is inevitably additional degradation of the mirror surface by the hard radiation in the region of the maximum laser field, which would obviously increase the intracavity losses still further.

MAIN IDEAS

In this paper we propose to use a crossed fluted cavity[6,7] as the optical cavity of the laser for the generation of gamma rays in intracavity inverse Compton scattering in a FEL. This eliminates the difficulties mentioned in Ref. 5, making it possible to increase the intracavity power and the intensity of the hard radiation substantially while avoiding the loss of gamma rays in passage through the cavity mirror (see Fig. 1).

Let us briefly recall the features of the crossed fluted cavity (CFC) device.[7] Unlike ordinary fluted cavities, the geometric generator of the concave mirror in revolution around the symmetry axis of the CFC is inclined at a small angle to this axis. As a result, the intersection zone of the rays propagating between the mirrors of the CFC occupies a central region of significant length, which is bounded by the outer caustic surface. At the mirrors these rays uniformly fill an annular region. For such a structure of the field the presence of a central hole in the mirror does not materially affect the parameters of the oscillation. In addition, this geometry of the field makes the CFC especially attractive for application to high-power FELs.[8]

It was shown in Refs. 9 and 10 (and also in 11–13) that stable oscillations can exist in the geometric structures just described, and the fundamental mode of the cavity indeed has an annular field distribution at the mirrors and a focused field distribution at the center of the cavity, at the proposed location of the undulator of the FEL. An experimental modeling[14] of the operation of the CFC in the millimeter wavelength range has confirmed the basic theoretical and computational results.

Thus, as follows from the above-described properties of the CFC and the sketch in Fig. 1, the use of a FEL with a CFC for generating coherent tunable radiation will make it possible to implement the following measures:

— to introduce a central hole in the cavity mirror (on the symmetry axis) for extracting the hard photons without loss in passage through the mirror. The introduction of the central hole will not affect the intensity of the intracavity radiation, since it does not increase the loss of the fundamental mode, on account of its annular distribution at the surface of the mirror;

— to increase sharply the intracavity radiation intensity and, hence, the intensity of the hard radiation through the use of cooled optics, for example, since the thickness and construction of the mirror do not affect the intensity of the hard radiation emerging from the cavity, as it does for conventional cavities;

— to eliminate the degradation of the mirror surface by the hard radiation, since the hard photons do not touch the surface of the mirror, so that the service life of the device is practically unlimited.

CONCLUSION

Let us emphasize that the advantages of using a crossed fluted cavity in a high-power FEL (the relatively high intensity of the hard radiation and the long service life) make it likely that a source of coherent tunable hard radiation can be built for solving specific problems in both fundamental and applied physics and for novel medical applications.

The authors thank J. M. J. Madey and E. Szarmes, University of Hawaii at Manoa, for interest in this study and for a stimulating discussion.

[1] F. R. Arutyunian and V. A. Tumanian, Phys. Lett. **4**, 176 (1963).
[2] R. H. Milburn, Phys. Rev. Lett. **10**, 75 (1963).
[3] V. B. Berestetskiĭ, E. M. Lifshitz, and L. P. Pitaevskiĭ, *Quantum Electrodynamics*, 2nd ed., Pergamon Press, Oxford (1982) [Russ. original, Nauka, Moscow (1980)].
[4] V. N. Litvinenko, Y. Wu, B. Burnham, G. Barnett, and J. M. J. Madey, Nucl. Instrum. Methods Phys. Res. **358**, 345 (1995).
[5] F. Glotin, J.-M. Ortega, R. Prazeres, G. Devanz, and O. Marcouille, Nucl. Instrum. Methods Phys. Res. **393**, 519 (1997).
[6] G. A. Bogatova, V. V. Perebejnos, and N. V. Cheburkin, Nucl. Instrum. Methods Phys. Res. **359**, 61 (1995).
[7] F. F. Baryshnikov, G. A. Bogatova, and V. V. Perebeĭnos, Pis'ma Zh. Tekh. Fiz. **21**(16), 67 (1995) [Tech. Phys. Lett. **21**(8), 663 (1995)].
[8] G. N. Kulipanov, A. S. Sokolov, and N. A. Vinokurov, Nucl. Instrum. Methods Phys. Res. **375**, 576 (1996).
[9] F. F. Baryshnikov, G. A. Bogatova, and V. V. Perebeĭnos, Kvantovaya Élektron. (Moscow) **23**, 349 (1996).
[10] N. V. Vinokurov and S. S. Serednyakov, *Proceedings of the Second Asian Symposium on Free Electron Lasers*, Novosibirsk, June 13–16, 1995; publ. (1996), pp. 141–149.
[11] F. F. Baryshnikov, G. A. Bogatova, V. V. Perebeĭnos, and N. V. Cheburkin, Opt. Spektrosk. **81**, 156 (1996).

[12] F. F. Baryshnikov, G. A. Bogatova, N. V. Cheburkin, and V. V. Perebejnos, Nucl. Instrum. Methods Phys. Res. **405**, 242 (1998).

[13] F. F. Baryshnikov, G. A. Bogatova, G. D. Bogomolov, A. I. Kleev, V. V. Perebeĭnos, and N. V. Cheburkin, Kvantovaya Élektron **24**, 230 (1997) [Quantum Electron. **27**, 224 (1997)].

[14] F. F. Baryshnikov, G. A. Bogatova, G. D. Bogomolov, V. V. Zavyalov, V. A. Ipatov, A. I. Kleev, V. V. Perebeĭnos, N. V. Cheburkin, E. Yu. Shamparov, Pis'ma Zh. Tekh. Fiz. **24**(19), 69 (1998) [Tech. Phys. Lett. **24**(10), 777 (1998)].

Translated by Steve Torstveit